THESIS FOR THE DEGREE OF DOCTOR OF PHILOSOPHY

Fabrication and noise properties of high-T_c SQUIDs with multilayer superconducting flux transformers

MAXIM L. CHUKHARKIN

CHALMERS

Department of Microtechnology and Nanoscience - MC2
CHALMERS UNIVERSITY OF TECHNOLOGY
Göteborg, Sweden 2013

Fabrication and noise properties of high-T_c SQUIDs with multilayer superconducting flux transformers
MAXIM L. CHUKHARKIN
ISBN 978-91-7385-877-9

Doktorsavhandlingar vid Chalmers tekniska högskola
Ny serie nr 3558
ISSN 0346-718X

Quantum Device Physics Laboratory
Department of Microtechnology and Nanoscience - MC2
Chalmers University of Technology
SE–412 96 Göteborg
Sweden
Telephone +46 (0)31-772-1000

ISSN 1652-0769
Technical report MC2-257

Chalmers Reproservice
Göteborg, Sweden 2013

Fabrication and noise properties of high-T_c SQUIDs with multilayer superconducting flux transformers
MAXIM L. CHUKHARKIN
Department of Microtechnology and Nanoscience - MC2
Chalmers University of Technology
Göteborg, Sweden 2013

Abstract

The thesis describes the development of high-T_c superconducting quantum interference devices (SQUIDs) with multilayer thin film flux transformers. High-T_c SQUID magnetometers are promising in various biomedical applications, including magnetoencephalography (MEG) and ultra-low field magnetic resonance imaging (ulf-MRI). Both MEG and ulf-MRI demand magnetic field sensitivity of less than 10 fT/Hz$^{1/2}$ at frequencies as low as 10 Hz. The magnetic field sensitivity of single-layer high-T_c SQUID magnetometers is typically about 50 fT/Hz$^{1/2}$. To improve the magnetic field sensitivity, superconducting flux transformer with a multiturn input coil should be used. The flux transformer requires multilayer superconducting structures, which is a significant challenge for high-T_c superconducting materials due to the anisotropy of the material and high temperatures required for a deposition of thin films.

Chemical-mechanical polishing (CMP) of high-T_c superconducting films has been developed in this work to fabricate multilayer structures. CMP improves surface smoothness of films, thereby reducing galvanic shorts between top and bottom superconducting electrodes. It has been shown that edge slope angles of about 2° can be fabricated using CMP, meaning that crossovers with very high critical current densities 2×10^6 A/cm^2 can be obtained. These results were important for successful fabrication of high-quality multilayer structures with high yield.

The CMP technique was used to fabricate multiturn magnetic flux transformers on 10×10 mm^2 STO substrates. A flip-chip magnetometer based on the developed multilayer flux transformer and a bicrystal SQUID was designed, fabricated and characterized. Magnetic field sensitivity of 8 fT/Hz$^{1/2}$ at 2 kHz and 80 fT/Hz$^{1/2}$ at 10 Hz has been demonstrated. Low-frequency magnetic flux noise was investigated and related with the microstructure of the flux transformer.

The developed multilayer flip-chip flux transformer was used in ulf-NMR experiments and demonstrated the improvement in the signal-to-noise ratio (SNR) when compared to a planar SQUID magnetometer. The demonstrated gain in SNR indicates the new multilayer structures are a promising technology for high-T_c SQUID-based ulf-MRI systems.

Lastly, high-T_c superconducting quantum interference filters (SQIFs) were designed and fabricated. The SQIF consisted of array of 50 SQUID loops connected in series along the bicrystal grain boundary. Electrical characterizations revealed a large spread of individual SQUID parameters that lead to the situation when only few SQUIDs from the whole array are operational at a certain bias current and voltage-to-field response demonstrates an absence of voltage dip at the zero external field. At the same time, it has been demonstrated that an array of identical SQUIDs benefit from higher voltage-to-flux transfer function as compared with a single SQUID.

Keywords: High-T_c SQUIDs, YBCO, SQUID magnetometers, ulf-NMR, SQIFs.

List of appended papers

This thesis is based on the work contained in the following papers:

I O.V. Snigirev, M.L. Chukharkin, A. Kalabukhov, M.A. Tarasov, A.A. Deleniv, O.A. Mukhanov, D. Winkler, "Superconducting quantum interference filters as RF amplifiers" *IEEE Trans. Appl. Supercond.* **17**. 2.718-721, 2007.

II A. Kalabukhov, M.L. Chukharkin, A.A. Deleniv, D. Winkler, I.A. Volkov, O.V. Snigirev, "Analysis of the possibility to amplify an RF signal with a superconducting quantum interference filter" *Journal of Communications Technology and Electronics.* **53**. 8. 934-40, 2008.

III M. Chukharkin, A. Kalabukhov, J.F. Schneiderman, F. Öisjöen, O.V. Snigirev, Z. Lai, D. Winkler, "Noise properties of high-T_c superconducting flux transformers fabricated using chemical-mechanical polishing." *Appl. Phys. Lett.* **101**. 4. 042602-042607, 2012.

IV F. Öisjöen, J.F. Schneiderman, G.A. Figueras, M.L. Chukharkin, A. Kalabukhov, A. Hedström, M. Elam, and D. Winkler, "High-T_c superconducting quantum interference device recordings of spontaneous brain activity: Towards high-Tc magnetoencephalography." *Appl. Phys. Lett.* **100**. 13. 132601, 2012.

V M. Chukharkin, A. Kalabukhov, J.F. Schneiderman, F. Öisjöen, O. Snigirev, M. Xie, M. Jönsson,D. Winkler, "Improvement of Ultra-Low Field Magnetic Resonance Recordings with a Multilayer Flux-Transformer-Based High-T_c SQUID Magnetometer." *IEEE Trans. Appl. Supercond.* **23**. 3. 1602404, 2013.

VI M. Chukharkin, A. Kalabukhov, N. Crovato, J.F. Schneiderman, M. Xie, O.V. Snigirev, D. Winkler, "Flip-chip multilayer high-T_c SQUID magnetometers with improved sensitivity." Manuscript, to be submitted for Superconductor Science and Technology.

Contents

1 Introduction

1.1 Superconductivity

In 1911 Kammerlingh-Onnes discovered sharp drop of the resistance in mercury when it was cooled down to 4 K. The residual resistance was immeasurable within the limit of the setup. This lead him to the conclusion that this may indicate a new state of matter – called superconductivity. Later it was confirmed by many experiments that several metals show similar transition to the state with zero resistance at a certain critical temperature T_c. The critical temperatures however were limited to very low values typically below 10 K. Therefore the potential applications of superconductivity were hampered by the need to use expensive cryogenic equipment.

The microscopic mechanism of superconductivity was explained in 1957 by Bardin, Cooper and Schrieffer who described superconducting transition in terms of weak attractive coupling of electrons through lattice vibrations (phonons). Below the critical temperature electrons form pairs (called Cooper pairs) in a Bose condensate described by a single wave function Ψ (order parameter). The microscopic theory described the properties of all known superconductors at that time and predicted their critical temperatures in excellent agreement with experiment. According to this theory the maximum critical temperature cannot exceed 30 K in elementary metals and binary compounds (low-T_c superconductors).

In 1987, Bednorz and Muller discovered superconductivity in the ceramic compound La_{2-x} $(Ba,Sr)_xCuO_4$ with a critical temperature around 35 K [1]. A few years later superconductivity was confirmed in many different compounds (called high-T_c superconductors) with a similar composition based on the copper oxide ceramic. Maximum critical temperature of some compounds exceeds 130 K. This high critical temperature cannot be explained by the microscopic theory based on weak electron-phonon interactions. Several models have been suggested to explain the mechanism of high-T_c superconductivity but so far there is no complete physical description of it.

Many high-T_c superconductors have critical temperature above the boiling point of liquid nitrogen (77 K). This opens more opportunities for practical applications of superconductivity as liquid nitrogen is cheap and easier to handle as compared with liquid helium required for operation of low-T_c superconductors. One of the most important high-T_c materials is $YBa_2Cu_3O_{7-x}$ with the critical temperature of 92 K.

High-T_c superconductors have complex chemical compositions and crystal structures. They are brittle ceramic materials. Their electronic and superconducting properties are anisotropic (i.e. depend on the direction of the crystal lattice). Fabrication of devices from these materials is much more complicated as compared with simple metallic low-T_c superconductors.

Applications of superconductivity range from high power electrical distribution lines and magnets to ultra low current devices with sensitivity close to quantum limit. This theses deals with development of magnetic field sensor based on high-T_c superconducting quantum interference device that can be used for the readout of magnetic signals from, e.g., human brain. Using high-T_c superconductors allows minimizing the distance from the sensor to the source of the magnetic field at room temperature. This can be advantageous as compared with low-T_c sensors as it helps to obtain new information from the human brain. The most important part of this work is the improvement of the sensitivity of high-T_c magnetometers that had to take into consideration complicated properties of high-T_c materials.

1.2 The Josephson effects

In 1962, Brian Josephson theoretically predicted that a supercurrent can flow between two superconductors separated by an insulating barrier [2]. He also predicted that if finite dc voltage is applied, there is an ac current that oscillates between two superconductors. These effects were experimentally confirmed in 1963 by Anderson and Rowell [3].

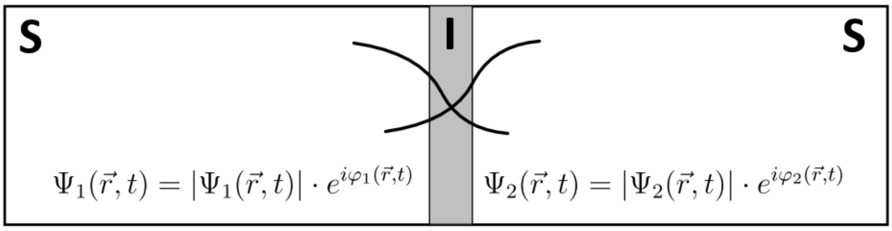

Figure 1: Superconductor-insulator-superconductor tunnel junction.

The supercurrent, I_S, through a Josephson junction is a periodic function of the phase difference ϕ between the two wave functions of the superconducting electrodes (see Fig. 1):

$$I_S = I_c sin\phi \tag{1}$$

where I_c is the maximum critical current of the Josephson junction. This is the dc Josephson effect.

When the supercurrent exceeds a critical value, there is a dc voltage across the junction that depends on the time derivative of the phase difference:

$$\frac{\partial \phi}{\partial t} = \frac{2e}{\hbar}V = \frac{2\pi}{\Phi_0}V \tag{2}$$

where $e = 1.6 \times 10^{-19}$ C is the electric charge, $h = 6.62 \times 10^{-34}$ J·s is Planck constant and $\Phi_0 = 2e/h = 2.068 \times 10^{-15}$ Wb is magnetic flux quantum. By integrating this equation one can see that phase difference linearly depends on time. Substituting this phase time dependence into Eq. 1, one can see that the supercurrent oscillates with the frequency $\frac{2e}{\hbar}V$. This is the ac Josephson effect.

The maximum critical current of the Josephson junction is defined by properties of superconducting electrodes, junction geometry and barrier properties. For an superconductor-insulator-superconductor (SIS) tunnel junctions the critical current can be estimated as [4]:

$$I_c = G_n \left(\frac{\pi \Delta(T)}{2e} \right) tanh \left(\frac{\Delta(T)}{2k_B T} \right) \tag{3}$$

where G_n is the tunneling conductance, $\Delta(T)$ is the temperature-dependent gap parameter, and $k_B = 1.38 \times 10^{-23}$ J·K^{-1} is the Boltzman constant.

In the presence of an external magnetic field H_0 parallel to the plane of the junction the phase difference of the Josephson junction (with length L) can be defined as:

$$\phi(x) = \frac{2\pi d}{\Phi_0} H_0 x + C \tag{4}$$

where $d = 2\lambda_L + t$ is the length of the of the region penetrated by the current and magnetic field (λ_L is the London penetration depth, t is the thickness of the insulator), and C is a constant. By substituting Eq. 4 into 1 and integrating over entire length L of the junction one can obtain the dependence of the maximum supercurrent I_0 that can pass through the junction without dissipation as a function of the total magnetic flux $\Phi = H_0 L d$:

$$I_0 = I_c \left| \frac{sin(\Phi/\Phi_0)}{\Phi/\Phi_0} \right| \tag{5}$$

The behavior of Josephson junction can be described in most cases by the resistively and capacitively shunted junction (RCSJ) model (see Fig. 2 (a)) [5, 6]. In this model, the total junction current is represented by a sum of the supercurrent I_S, a normal current $I_n = V/R_n$ (where R_n is the normal resistance), a displacement current in the shunting capacitance $I_D = C\frac{dV}{dt}$ and a fluctuation current I_f:

$$I = C\frac{\Phi_0}{2\pi}\ddot{\phi} + \frac{1}{R_n}\frac{\Phi_0}{2\pi}\dot{\phi} + I_c \sin\phi + I_f \tag{6}$$

The equivalent circuit diagram of the RCSJ model is shown in the Fig. 2.

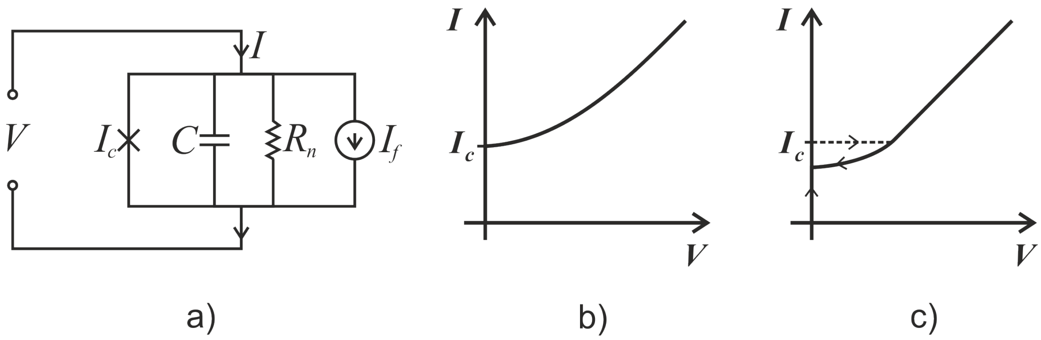

Figure 2: Equivalent circuit of the Josephson junction in the framework of the RCSJ model (a). I–V characteristics of the resistively shunted Josephson junction in cases $\beta_c \leqslant 1$ (b) and $\beta_c > 1$ (c).

Equation 6 describes dynamic electrical properties of the Josephson junction for both superconducting and resistive states. The mechanical analogue of a Josephson junction is a pendulum with the moment of inertia $C\frac{\Phi_0}{2\pi}$, coefficient of viscosity $\frac{1}{R_n}\frac{\Phi_0}{2\pi}$, maximum gravitational torque I_c and external torque I [7].

Eq. 6 can be rewritten in terms of $\beta_c = \frac{2\pi I_c C R_n^2}{\Phi_0}$ and $\omega_c = \frac{2\pi I_c R_n}{\Phi_0}$ [5]:

$$I/I_c = \beta_c \omega_c^{-2}\ddot{\phi} + \omega_c^{-1}\dot{\phi} + I_c \sin\phi + I_f \tag{7}$$

where β_c is the Stewart-McCumber parameter and ω_c is a characteristic Josephson frequency. In case of very small $\beta_c \leqslant 1$ one can neglect the capacitance term in Eq. 6 and 7. Current-voltage characteristic of such Josephson junction is described by the relations:

$$\begin{aligned} \overline{V} &= 0 && for \quad I \leq I_c \\ \overline{V} &= R_n\sqrt{I^2 - I_c^2} && for \quad I > I_c \end{aligned} \tag{8}$$

where $\overline{V}$ is the average voltage across the junction (see Fig. 2 (b)). When $\beta_c > 1$, the $I - V$ characteristic of Josephson junction becomes hysteretic as shown in Fig. 2 (c).

Josephson junctions can be used in a variety of applications such as a microwave generators or detectors for terahertz radiation, or mixers and amplifiers using the ac Josephson effect [8]. The dependence of the critical current on magnetic field can in principle be used for detection of magnetic field. But since the junction cross-sectional area is usually very small, the magnetic field sensitivity is also very low. Also, the dependence is not periodic and nonlinear. More practical ways to make a sensitive detectors for magnetic flux is to include one or two Josephson junctions in a superconducting loop, forming rf or dc SQUID.

1.3 Principles of dc SQUIDs

One or two Josephson junctions connected by a superconducting loop form a radio frequency (rf) or a direct current (dc) superconducting quantum interference device (SQUID), respectively. The principles of operation of both rf and dc SQUIDs are similar. We describe here only dc SQUIDs as they are the most commonly used devices.

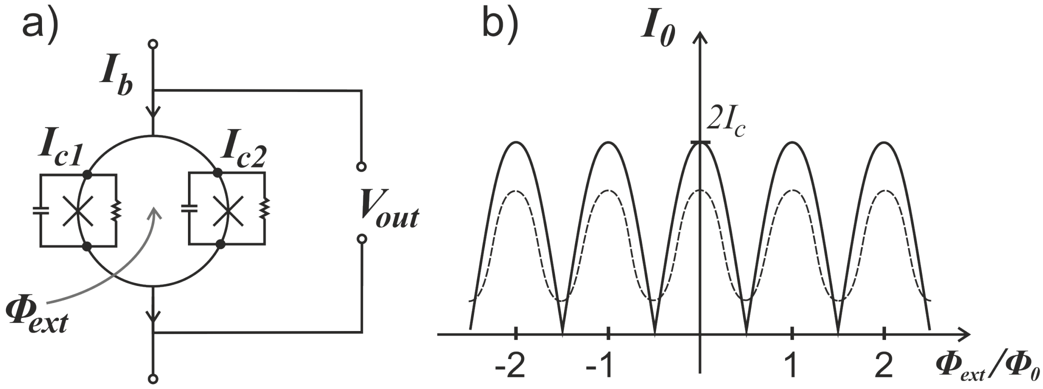

Figure 3: a)-equivalent circuit of the SQUID. b)- dependence of the total critical current I_0 of the SQUID on the applied flux. Solid line for the symmetrical SQUID, dashed line for asymmetrical SQUID with $I_{c1} = 2I_{c2}$.

The equivalent circuit of the dc SQUID is shown in the Fig. 3. The SQUID operation is based on two principles: the dc Josephson effect described above and the flux quantization effect. When the current in the SQUID loop is below critical currents of both junctions the magnetic flux in the loop is an integer number of single flux quanta $\Phi = n\Phi_0$. The maximum supercurrent I_0 of the SQUID is the result of interference of two junctions. The total critical current of the SQUID is a periodic function of the applied external magnetic flux, Φ_{ext}. In case of a SQUID with nonhysteretic ($\beta_c \leqslant 1$)

junctions and with negligible inductance L_S this dependence can be written as [9]:

$$I_0(\Phi_{ext}) = [(I_{c1} - I_{c2})^2 + 4I_{c1}I_{c2}cos^2(\pi\Phi_{ext}/\Phi_0)]^{1/2} \tag{9}$$

In an important case of a symmetric dc SQUID ($I_{c1} = I_{c2} = I_c$), this equation can be written as:

$$I_0(\Phi_{ext}) = 2I_c \cos\left|\frac{\pi\Phi_{ext}}{\Phi_0}\right| \tag{10}$$

This dependence of the total critical current (both symmetric and asymmetric) on the applied flux is shown in Fig. 3 (b) [9].

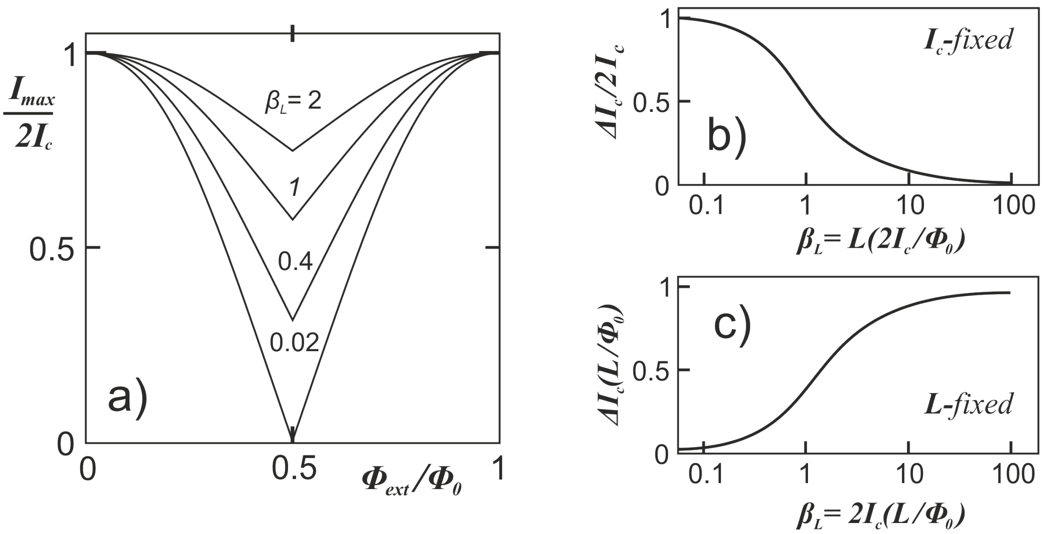

Figure 4: a)–critical current of dc SQUID vs. applied flux for different β_L. Critical current modulation vs. β_L as a function of L (b) and I_c (c) [10].

From Eq. 10 one can see that for $I_{c1} = I_{c2} = I_c$ the total critical current of the dc SQUID can modulate between $2I_c$ and 0. Equation 10 is valid only for very low inductance when the screening parameter of the SQUID $\beta_L = \dfrac{2I_cL_S}{\Phi_0}$ is close to zero. For a nonzero β_L, the total flux through the SQUID loop is $\Phi_T = \Phi_{ext} - L_SI_{sc}$, where I_{sc} is the screening current. The dependences of the critical current modulation of the SQUID on the β_L obtained by numerical simulations are presented in the Fig. 4 [10]. As L_S is reduced below a value corresponding to $\beta_L \approx 0.1$, ΔI_c approaches the limit $2I_c$ independent of L_S (see Fig. 4 (b)). Fig. 4 (c) demonstrates the plot of the $\Delta I_c/(\Phi_0/L)$ as a function of $\beta_L = I_c(2L_S/\Phi_0)$ (fixed L) where the modulation depth approaches a limit independent of I_c for sufficiently large values of I_c [10].

Let's consider a symmetric dc SQUID. When the SQUID is biased with $I_{bias} \approx 1.1 I_c$ the modulation of the critical current produces a corresponding voltage modulation (see Fig. 5). Therefore, the SQUID works as flux-to-voltage converter. The SQUID sensitivity is defined by the maximum slope of the voltage-to-flux transfer function, $V_\phi = \partial V/\partial \Phi$ at the bias point W where $\Phi_{ext} = (n \pm 1/4)\Phi_0$.

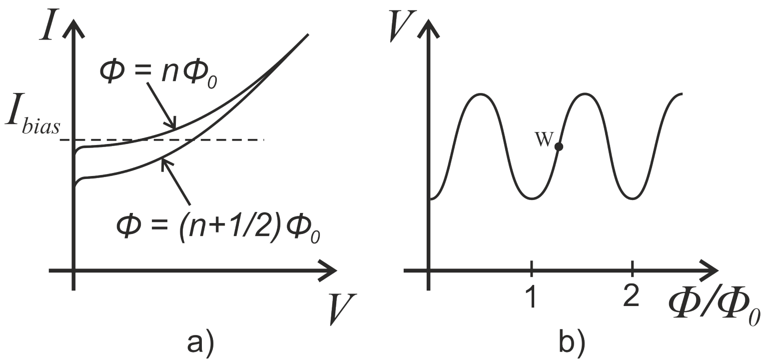

Figure 5: a)–I-V characteristics of the SQUID. b)– dc SQUID voltage V as a function of external applied magnetic flux Φ/Φ_0 at constant bias current I_{bias}.

1.4 Noise of the dc SQUID

The magnetic flux sensitivity of the dc SQUID is defined by the noise sources from several different contributions. There are thermal Johnson-Nyquist noise of the Josephson junctions in normal state, thermal fluctuations of the critical currents, and external fluctuations. In case of high-T_c SQUIDs, another contribution from thermally activated motion of flux vortices that produce $1/f$ magnetic flux noise is also significant. For simplicity we disregard the contribution of external fluctuations.

Thermal fluctuations produce voltage noise in the Josephson junctions in the resistive state with a frequency independent spectral density ("white noise"). When estimating this noise one should consider two important factors. First, the dynamic resistance at the bias point can be different from the normal resistance of the junction $R_d \approx 1.3 - 1.7 R_n$ for low-T_c SQUIDs at for 4 K [11]. Second, thermal fluctuations induce noise current in the SQUID loop that in turns generates the flux noise. This contribution is less important for SQUIDs working at 4 K but has to be taken into account for SQUIDs operated at higher temperatures.

It has been shown that optimal noise properties of the dc SQUID can be achieved with the β_L close to 1 [10]. In this case, for low-T_c SQUIDs the spectral density of voltage noise at the SQUID output can be estimated as $S_V = 16k_BTR_n$ [11]. An equivalent magnetic flux noise can be estimated from the spectral density of voltage noise as $S_\Phi = S_V/V_\Phi^2$. For a typical value of normal resistance 5 Ω and voltage modulation of 50 μV at 4 K, corresponding voltage noise and equivalent flux noise are $S_V = 4.4 \times 10^{-21}$ V and $S_\Phi = 2.8 \times 10^{-11}$ Wb, respectively. This shows that SQUID is an extremely sensitive detector of magnetic flux. It can be also be used for very sensitive measurements of different physical signals that can be converted in to magnetic flux: magnetic field, current, voltage etc.

The analysis of the noise in high-T_c SQUIDs is more complicated as it has to take into account the effect of SQUID inductance on the white noise. This can be considered as an effective reduction of the voltage transfer function. One can show that in this case spectral density of the voltage noise can be written as $S_V = 2k_BTR_n[R_d^2/R_n^2 + L_S^2V_\Phi^2/k_BTR_n]$ [12]. The estimation of the flux noise of the high-T_c SQUID shows a value about 10 $\mu\Phi_0/\mathrm{Hz}^{1/2}$.

At low frequencies (below 10 kHz) the spectral density of the flux noise depends on the frequency as $1/f$ (so called "flicker noise"). There are two main sources of low frequency noise in dc SQUIDs. One is due to thermal fluctuations of the critical currents of Josephson junctions. The fluctuations of the critical currents can produce the voltage across the SQUID ("in-phase" mode). For low-T_c SQUIDs these fluctuations are negligible. For high-T_c SQUIDs critical current fluctuations are the one of the main sources of the low frequency noise.

The second major source of the *1/f* noise is thermally activated motion of flux vortices in the superconducting electrodes. The movement of the vortex produces change in magnetic flux coupled to the SQUID ("direct noise"). This process induces a random telegraph signal (RTS) in the SQUID output when a single vortex is hopping between two pinning sites. A superposition of the RTS in the SQUID loop produces the spectra scaling as *1/f.* Such *1/f* noise is much bigger issue in high-T_c SQUIDs compared with low-T_c ones because of the larger thermal activation at the operational temperature 77 K.

1.5 Operation of the dc SQUID in flux-locked loop

As it was shown, the SQUID is a very sensitive magnetic flux sensor. But the sensitivity of the SQUID depends on the flux bias. It has maximum sensitivity at $\Phi_0(n \pm 1/4)$ and zero sensitivity at $n\Phi_0$ and $\Phi_0(n + 1/2)$. This limits dynamic range and makes SQUID inconvenient for practical use. To circumvent this problem, a so called flux-locked loop (FLL) electronics has been developed [13]. An equivalent circuit diagram of the FLL is shown in Fig. 6. The basic idea of the FLL is a negative feedback to compensate minute changes in external flux in the SQUID loop. To do this the signal from preamplifier is integrated and sent through the feedback resistor to the SQIUD loop using feedback coil. The voltage that has to be applied to the feedback coil to keep the working point constant is therefore proportional to the external magnetic flux variation. This scheme allows linearization of the SQUID output increasing its dynamic range to about 150 dB [11].

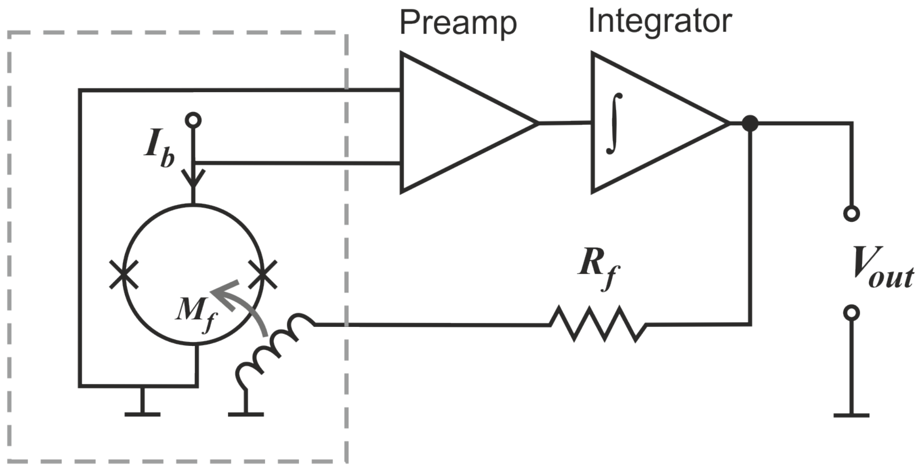

Figure 6: Basic FLL circuit diagram. Components inside the dashed box are at cryogenic temperature.

1.6 Practical aspects of SQUID fabrication

First practical SQUIDs were made from point contacts. They were bulky and a reproducibility of the fabrication process was low [14]. Real advances in low-T_c SQUIDs fabrication were made using Nb thin film technology and tunneling trilayer Nb/Al-AlO$_x$/Nb Josephson junctions [15]. These low-T_c niobium SQUIDs have shown very high reproducibility, good control of parameters and commercially available.

The fabrication of the high-T_c SQUIDs is a more complicate task because of the peculiar properties of these materials. In this work we used $YBa_2Cu_3O_{7-x}$ (YBCO) which is the most extensively researched and easy-to-use material. Crystal structure of the YBCO is presented in Fig. 7. The structure of YBCO is related to that of perovskite with apical oxygen atoms removed from the structure. YBCO has a layered structure with the stacking sequence of the a-b planes: Y–CuO–BaO–CuO$_2$–BaO–CuO$_2$–Y [16, 17].

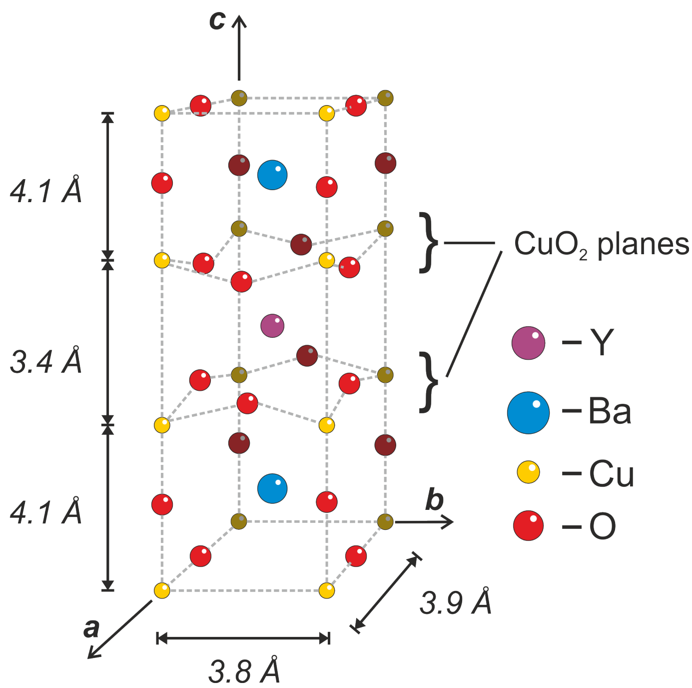

Figure 7: Crystal structure of YBCO.

Physical parameters of the YBCO are listed in the Table 1 [16]. YBCO belongs to Type II class of superconductors which are characterized by their ability to retain their superconducting properties in very high magnetic fields [16, 18]. Superconducting properties of the $YBa_2Cu_3O_{7-x}$ depend on the oxygen content (x-value, $0 \leq x \leq 1$). The material becomes non-superconducting at $x \geqslant 0.6$. The transition temperature remains around 90 K from x=0 to x≈0.2 and then shows a plateau at 60 K when x=0.3–0.4 [17].

One of the peculiarities of copper-oxide superconductors is the anisotropy of their normal and superconducting properties due to the layered crystal structure. As it can be seen from the Table 1, the penetration depth and coherence length of the YBCO are different in the a-b plane, parallel to the layers, compared to the c-direction, which is perpendicular to the layers. The strong uniaxial anisotropy was observed in the normal state resistivity, magnetic susceptibility, critical current density and in the superconducting upper and lower critical fields [16].

Anisotropy and very short coherent length prohibit fabrication of SIS tunneling junctions in high-T_c superconductors. One possible way to make high-T_c Josephson junctions is to use grain boundaries that are known to act as weak links limiting the transport critical current density of these materials [19, 20]. Critical current density depends strongly on the misorientation

Table 1: Physical parameters of $YBa_2Cu_3O_{7-x}$.

Parameter	Values
Transition temperature	T_c=92 K
Penetration depth	$\lambda_L(ab)$=1400 Å, $\lambda_L(c)\sim 5\times1400$ Å
Coherence length	$\xi(ab)$=15 Å, $\xi(c)$=3–5 Å
Crystal lattice parameters	a=3.82 Å, b= 3.89 Å, $c/3$=3.89 Å
Thermal conductivity	3.2×10^{-2} W/cm·K(at 300 K)
Specific heat capacity	0.39 J/g·K

angle between grains. The Josephson junctions can be formed by patterning narrow bridges across grain boundaries. Individual grain boundary Josephson junctions (GBJ) with controllable and reproducible characteristics were fabricated by growing the YBCO thin films on bicrystal substrates [19]. Further studies [20, 21] demonstrate that GBJs behave similarly as resistively shunted Josephson junctions with the Stewart-McCumber parameter $\beta_c < 1$. To make GBJs, special substrates consisting of two crystals bonded together with the misorientation angles 18°–36° are used. Typical critical current densities of GBJs fabricated on the 24° bicrystal substrates are $10^4 - 10^5$ A/cm^2 [22]. The bicrystal technique is widely used for the high-T_c Josephson junctions fabrication due to its reproducibility and relative simplicity [23, 24].

1.7 Magnetic field sensors based on dc SQUIDs

Dc SQUID can be naturally used as a detector of magnetic field. The magnetic field sensitivity is defined as $S_B = S_\Phi/A_{eff}^2$, where A_{eff} is the effective area of the SQUID. The effective area is defined as $A_{eff} = B_0/\Phi_0$ where the B_0 is external magnetic field that produces one flux quantum in the SQUID loop. The effective area is proportional to the geometric area of the SQUID loop but not necessarily equal to it. In any case the geometric area of the SQUID loop should be increased in order to increase its effective area. The upper limit on the SQUID loop size is set by the need to satisfy the condition $\beta_L \approx 1$. Since SQUID inductance also increases proportionally to the loop size, the area of the SQUID cannot be increased infinitely. The effective area of the sensor can be increased by using flux focusing effect [25, 26, 27]. The SQUID loop is made with a wide washer that due to the Meissner effect repels the magnetic field by shielding currents and concentrates it in the central hole (see Fig. 8(a)). At the same time the inductance of the SQUID loop depends mainly on d_S. The effective area of the SQUID with such flux focuser can be estimated as $A_{eff} = D_S \times d_S$

[25]. For a dc SQUID with 1×1 mm^2 washer and $d_S = 60$ μm the effective area is around 0.06 mm^2 that corresponds to the transformation coefficient $1/A_{eff} = 33$ nT/Φ_0. For a typical flux noise of 10 $\mu\Phi$ (for a high-T_c SQUIDs) this corresponds to equivalent magnetic field noise of $S_B^{1/2}$= 330 fT/Hz$^{1/2}$. Layouts of the high-T_c SQUIDs with wide washer are presented in the Fig. 8.

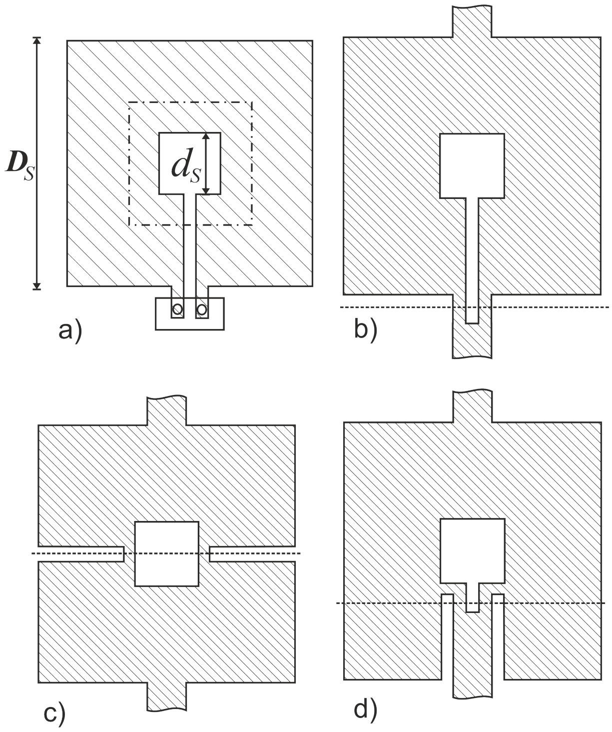

Figure 8: a)–Design of SQUID magnetometer with flux-focusing washer. Circles indicate Josephson junctions for a typical low-T_c layout. Dash dotted line indicates the dimensions of the effective area of the sensor. b), c), d)–layouts of high-T_c SQUIDs with washer. Dashed lines indicate the position of grain boundaries. The figures are adapted from [25] and [28].

To further increase the magnetic field sensitivity, a superconducting flux transformer is used [25, 24, 29]. The idea of the flux transformer is to couple a large area pickup loop to the small SQUID inductance. Schematic diagram of the superconducting flux transformer is shown in the Fig. 9. A large pickup loop is connected to a multiturn input coil forming a closed superconducting circuit. The input coil is inductively coupled to the SQUID loop with mutual inductance $M_i = \alpha\sqrt{L_S L_I}$, where L_I and L_S are the inductances of the input coil and the SQUID correspondingly; $0 < \alpha < 1$ is the coupling coefficient. In

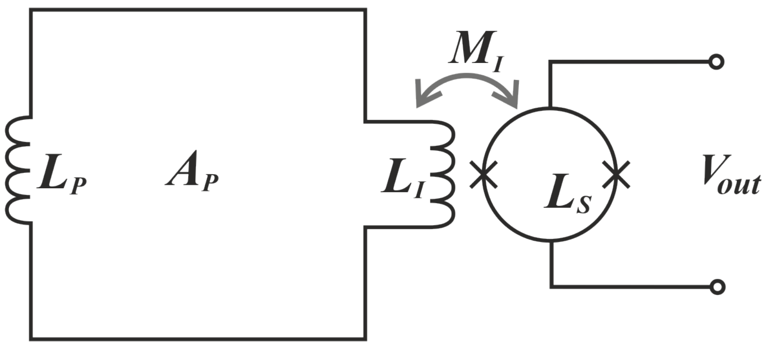

Figure 9: Schematic circuit of an inductively coupled SQUID magnetometer.

the absence of resistive losses circulating dc screening current in the pickup loop generated by an external magnetic field creates magnetic flux in the SQUID loop. A detailed analyzes of this circuit gives following result for the effective area of such SQUID magnetometer with the superconducting flux transformer [30]:

$$A_{eff} = A_S + A_P \cdot \frac{M_i}{L_I + L_P} \tag{11}$$

where A_S is the effective area of the SQUID, and L_P is the pickup loop inductance. The effective area reaches maximum when $L_I \approx L_P$ [28]. A_S is typically much smaller than A_P, so the Eq. 11 can be reduced to:

$$A_{eff} = \frac{\alpha}{2} \cdot A_P \cdot \frac{\sqrt{L_S}}{\sqrt{L_P}} \tag{12}$$

This design allows increasing the effective area without the cost of the SQUID performance. There should be tight coupling between input coil and the SQUID loop. This can be achieved by using a planar thin-film superconducting flux transformer integrated on the same chip with the SQUID. High coupling coefficients of 0.75–0.8 can be realized in this case. Fig. 10 shows calculated magnetic field noise of the SQUID magnetometer with flux transformer according to Eq. 12 as a function of pickup loop size D (calculated for $\alpha = 0.75$, width of the pickup loop w_P=0.5 mm, $L_S = 100$ pH).

Practically magnetic field sensitivity of low-T_c SQUID magnetometers with the size 30×30 mm^2 below 1 fT/Hz$^{1/2}$ was achieved [8]. For a long time it was the best magnetic field sensitivity among all magnetometers. SQUID sensors were successfully used in commercial applications such as multichannel systems for magnetoencephalography (MEG) [31]. Recently similar or even better sensitivity was achieved using spin-exchange relaxation-free atomic magnetometers, but they are orders of magnitude larger in size,

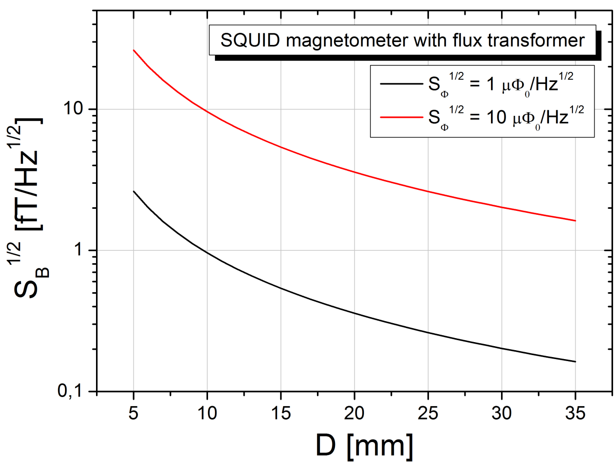

Figure 10: Calculated dependence of the equivalent magnetic field noise of a dc SQUID with superconducting flux transformer as a function of the pickup loop size calculated for two different values of equivalent flux noise 1 and 10 $\mu\Phi_0\mathrm{Hz}^{1/2}$ (α=0.75, w_P=0.5 mm, L_S = 100 pH).

can only operate near zero magnetic field and still far from mass production [32]. Mixed sensors that consists of a giant magnetoresistive sensor and superconducting loop is another possible candidate for biomagnetic applications, with the magnetic field sensitivity approaching that of SQUIDs. However a common issue all compared competing technologies have is the inferior sensitivity below 20 Hz comparing to the SQUIDs [33].

1.8 Magnetometers based on high-T_c dc SQUIDs

All considerations of the previous paragraph are valid for both low-T_c and high-T_c SQUIDs. However, realization of the multilayer superconducting flux transformer in high-T_c materials is a very challenging task due to high temperatures during the deposition of high-T_c thin films and anisotropy their of physical properties. In the beginning of the development of high-T_c SQUIDs, galvanically coupled pickup loop was introduced [34, 35]. Screening current generated in a pickup loop is injected directly in to the SQUID loop producing magnetic flux that is detected. This design allows fabrication of the SQUID and flux transformer in a single layer of superconducting film. Fig. 11 shows schematic diagram of a single layer dc coupled SQUID magnetometer and the layout of the SQUID loop.

Effective area of such galvanically coupled SQUID magnetometer can be

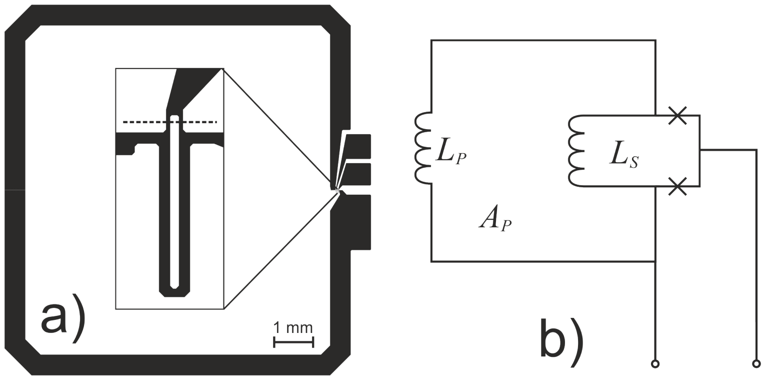

Figure 11: a)– layout of a dc coupled SQUID magnetometer. Dashed line indicates a position of a grain boundary. b)– schematic circuit of a dc coupled single layer SQUID magnetometer.

estimated using equation:

$$A_{eff} = k \cdot A_P \cdot \frac{L_S}{L_P} \tag{13}$$

where A_P is the area of the pickup loop; L_S and L_P are the SQUID and pickup loop inductances, correspondingly; k is the coupling coefficient typically equal to 0.9. This equation shows that this design suffers from the large mismatch between pickup loop and SQUID inductances as compared with Eq. 12. Fig. 12 shows calculated magnetic field sensitivities of the directly coupled and inductively coupled SQUID magnetometers as a function of the pickup loop size. It can be seen that for a pickup loop size $D = 9$ mm the magnetic field sensitivity of the single layer sensor is 6 times lower compared with a SQUID sensor with inductively coupled flux transformer.

Nevertheless, dc-coupled scheme was successfully implemented in practical high-T_c SQUID magnetometers with the best achieved magnetic fields sensitivity of 25 fT/Hz$^{1/2}$ [36]. More advanced planar first order gradiometers with a field gradient noise of 72 fT/Hz$^{1/2}$ (at high frequencies) were demonstrated by Seidel *et. al.* [37].

Several attempts were made to fabricate high-T_c superconducting multilayer flux transformer. Ludwig *et.al.* demonstrated a high-T_c SQUID magnetometer with integrated 8×8 mm^2 pickup loop that shows the magnetic field sensitivity below 10 fT/Hz$^{1/2}$ at 1 kHz (53 fT/Hz$^{1/2}$ at 10 Hz) [38]. High-T_c SQUID magnetometers with 16×16 mm^2 multilayer flux transformers fabricated by Faley *et.al.* demonstrate even better sensitivity of 3.5 fT/Hz$^{1/2}$ at 1 kHz (7 fT/Hz$^{1/2}$ at 1 Hz) [39].

Despite that high-T_c SQUIDs have higher noise and lower magnetic field

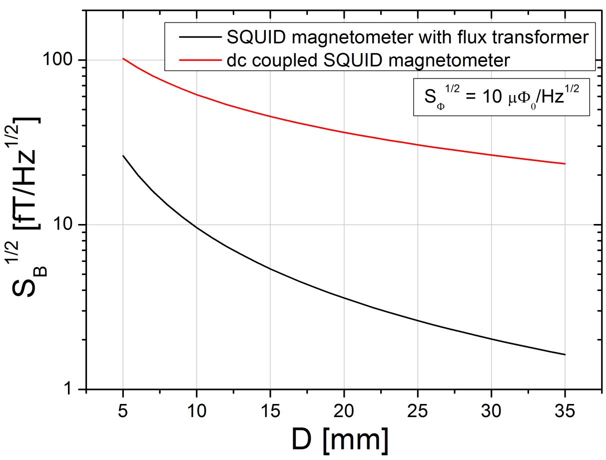

Figure 12: Dependence of the equivalent magnetic field noise as a function of the pickup loop size calculated for two SQUID sensor with flux transformer (black) and dc coupled SQUID magnetometer (red).

sensitivity compared with low-T_c SQUIDs, they can benefit for practical applications. First, using liquid nitrogen significantly simplifies cryogenic system design and decreases operational costs. Secondly, higher operation temperature allows minimizing the distance between sensor and object at room temperature. The latter is very important for MEG.

1.9 SQUID applications in biomagnetism

Magnetometers based on SQUIDs are widely used in various biomedical applications, including magnetocardiography (MCG), magnetoencephalography (MEG) and ultra-low field magnetic resonance imaging (ulf-MRI) [8]. These applications require very high magnetic field sensitivity. For the MEG it should be less than 10 fT/Hz$^{1/2}$ at 10 Hz [40, 41, 42, 43].

MCG is a technique to measure the magnetic fields produced by electrical activity in the heart. MCG experiments using SQUID magnetometers were first performed in 1969 by Cohen *et al.* [44] in magnetically shielded room (MSR). Since then, SQUID based MCG systems were improved from an one channel prototype to the multichannel systems, which can operate in an unshielded environment [8]. Modern MCG systems contain up to 77 channels and are using SQUIDs (typically low-T_c) with a sensitivity around 5 fT/Hz$^{1/2}$ [45, 42]. Usage of gradiometric configurations allows MCG systems to operate in unshielded environment that can significantly reduce the costs.

Ultra-low-field (ulf) NMR/MRI is a new spectroscopic/imaging modality that can potentially lead to cheaper, simpler, and, for some applications better magnetic resonance capabilities. Because the measurement field is of the same order of magnitude as that of the earth's magnetic field ($\sim 50\ \mu$T), ulf-MR systems do not require bulky and expensive superconducting coils, thereby reducing up-front and running costs. Perhaps most importantly, T_1 contrast at ultra-low fields is significantly enhanced and allows, for example, contrast-free imaging of prostate cancer [46].

However, recording at ultra-low fields imposes several challenges, the most significant of which is a low signal-to-noise ratio (SNR). Standard MR systems tend to employ high magnitude measurement fields (several Tesla) and coil-based RF antennas as the sensing element because the signal from such a coil is proportional to the measurement field squared. As that field is reduced below the mT range, SQUIDs become advantageous because the signal from a SQUID is directly proportional to the measurement field [43].

Recently, Busch *et al.* demonstrated ulf-MRI system equipped with low-T_c SQUIDs [43, 46]. The magnetic field noise of the SQUID detectors was typically 0.5–1 fT/Hz$^{1/2}$. This system was used to measure the proton longitudinal relaxation time T_1 in *ex vivo* prostate tissue specimens from radical prostatectomies of 35 patients with prostate cancer at 132 μT. The NMR and MRI measurements suggest that MR images with T_1 contrast established at ultra-low fields may discriminate prostate cancer from normal prostate tissue *in vivo* without a contrast agent [46].

Magnetoencephalography (MEG) is a technique for mapping brain activity by recording magnetic fields produced by electrical currents occurring in the brain, using very sensitive magnetometers [47].The first successful attempts to reveal magnetic signals generated by neural activity in the human brain were performed in the mid 1960s [8]. They were carried out using non-superconducting detector and the quality of those signals was very poor. Only using recently invented SQUIDs in the MSR allowed to improve the sensitivity of the MEG system and record the first good quality magnetoencephalograms [8, 48]. A review of the MEG theory and instrumentation can be found in [47].

MEG now is one of the most important neuroimaging technologies [8]. A modern SQUID-based MEG system consists of hundreds of channels and is commercially available [31]. The low-T_c SQUIDs used in such systems can have a magnetic field sensitivity around 3 fT/Hz$^{1/2}$.

Over the past decade, many biomagnetic SQUID systems have evolved from prototypes to full-featured clinical devices [8, 31]. Nevertheless, most of these systems use low-T_c SQUIDs sensors. These magnetometers may yield magnetic field sensitivity below 1 fT/Hz$^{1/2}$, but they require liquid helium temperatures (4.2 K) for operation. To simplify cooling requirements, high critical-temperature (high-T_c) SQUIDs can be utilized that operate at the boiling point of liquid nitrogen (77 K). Another advantage of using high-T_c SQUID sensors is minimizing of the separation between sensor and tested object, which is very important for example for MEG.

A single- and two-channel high-T_c SQUID MEG recordings of spontaneous brain activity in two healthy human subjects were performed at Chalmers University of Technology in 2011. The modulation of the occipital alpha rhythm and the mu rhythm were demonstrated using dc coupled single-layer SQUID magnetometers with magnetic field sensitivities of 50 fT/Hz$^{1/2}$ [36]. It was shown that despite higher noise-levels compared to their low-T_c counterparts, high-T_c SQUIDs can be used to detect and record physiologically relevant brain rhythms with comparable signal-to-noise-ratios.

Ulf-NMR/MRI system was also developed in Chalmers University. NMR signals were obtained from water in a measurement field of 80 μT and two NMR peaks were successfully resolved from two spatially separated water samples in a gradient field. Being combined with MEG, ulf-MRI system could be a powerful tool for investigation of the human brain. However, the magnetic field sensitivity of present single-layer SQUID sensors was not sufficient to obtain high signal-to-noise ratios required for imaging.

Both MEG and ulf-MRI systems will benefit from using high-T_c SQUID sensors with magnetic field sensitivity below 10 fT/Hz$^{1/2}$. This level of sensitivity can be achieved only using SQUIDs inductively coupled with superconducting flux transformer. There have been several attempts to realize superconducting flux transformers made from high-T_c materials and the magnetic field sensitivity of magnetometers combined with such flux transformers below 10 fT/Hz$^{1/2}$ has been demonstrated [39]. While such demonstrations of highly-sensitive high-T_c SQUID magnetometers serve well as proofs-of-principle, such fabrication techniques suffer from low fabrication yield and/or require materials that are potentially hazardous. Main goal of this work was to develop a safe and reproducible process for fabrication of high-T_c superconducting multilayer flux transformers and use them in combination with bicrystal dc SQUIDs to achieve magnetic field sensitivity below 10 fT/Hz$^{1/2}$.

2 Fabrication of thin film multilayer high-T_c superconducting structures

2.1 Specific requirements for fabrication of high-T_c multilayer structures

As it was discussed in the introduction, high-T_c superconducting materials have complicated chemical and physical properties that prohibit standard fabrication methods developed for thin film metallic superconductors. There are few problems: a high fabrication temperature that provides conditions for diffusion species across boundaries, another problem is the anisotropy of physical and electrical properties. Critical current density in a direction parallel to the a-b planes is 10–1000 times higher as along the c-axis direction. For this reason thin films of high-T_c superconductors should be grown in a way that the c-axis is perpendicular to the plane of the substrate and most of the supercurrent flows along the a-b planes. Moreover, presence of unwanted grain boundaries may result in formation of weak links with reduced critical current density and this should be avoided.

In a multilayer structure there are at least two superconducting layers separated by an insulator. For a superconducting flux transformer there should also be a connection between two layers (often called via). Since both films are expected to grow in the c-axis direction, the via is the most difficult part to fabricate in high-T_c multilayer structure. It would require that part of the current should flow along the the c-axis direction that decreases the critical current density substantially. Since the bottom electrode should also be patterned, the top superconducting layer will be grown not on a flat surface but also on step edges of the bottom structure. The step edges may also lead to a formation of non c-axis oriented films that reduce the critical current density.

A common solution for both problems is to fabricate edges of the bottom electrode structures with very low angles. High quality c-axis oriented high-T_c film can be grown with angles below 10° [49]. This helps to avoid formation of a-axis oriented grains in the top superconducting layer thereby keeping high critical current density. In the via, this also helps to increase the overlap between the top and bottom electrode where current flows along the a-b planes (see Fig. 13 (b)) (in this case one should take into account that critical current will be defined not by area but the perimeter of the via). There are two approaches how one can obtain shallow edges: chemical mechanical polishing and anisotropic wet etching. These methods will be described in following two sections.

Beside this, there are more complications in the fabrication of high-T_c multilayer structures. One is that usually the surface of the high-T_c films is very rough due to the presence of outgrowths and droplets. This leads to the formation of shorts between superconducting layers. It is rather difficult to grow very smooth high-T_c films. It would be desirable to improve the surface of the bottom electrode during the fabrication process. It will be shown later that chemical mechanical polishing can solve this problem and it was one of the reasons why it was chosen in this work.

To obtain high quality epitaxial single crystal high-T_c superconducting films, high deposition temperature (about 800°C) and high oxygen pressure are typically used. In terms of microfabrication, this restricts using polymer resist layers for lift-off and shadow mask evaporation. Finally, superconducting properties of high-T_c materials are very sensitive to oxygen stoichiometry that may easily be affected during the fabrication process, i.e. during heating or ion beam milling used for film etching.

2.2 Deposition and patterning of epitaxial superconducting $YBa_2Cu_3O_{7-x}$ films

For practical devices high quality thin $YBa_2Cu_3O_{7-x}$ films are needed. There are several methods of the YBCO films deposition [16]:

- magnetron dc sputtering;
- thermal or e-beam evaporation;
- metalorganic chemical vapor deposition (MOCVD);
- pulsed laser deposition (PLD).

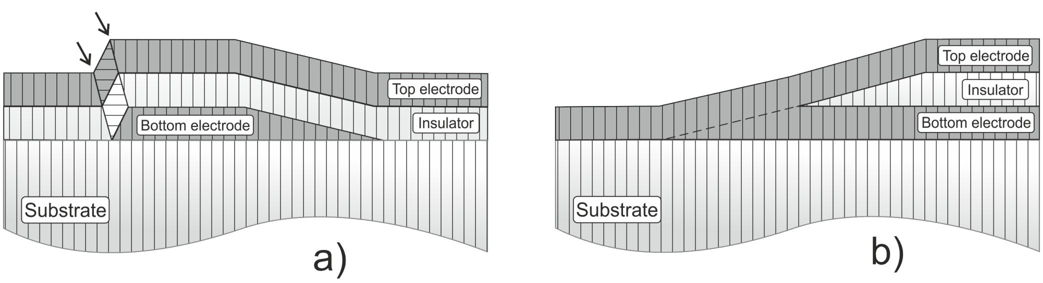

Figure 13: An illustration of the high-T_c superconducting crossover (a) and via (b). The arrows indicate unwanted grain boundaries formed in top film on slope with large angle.

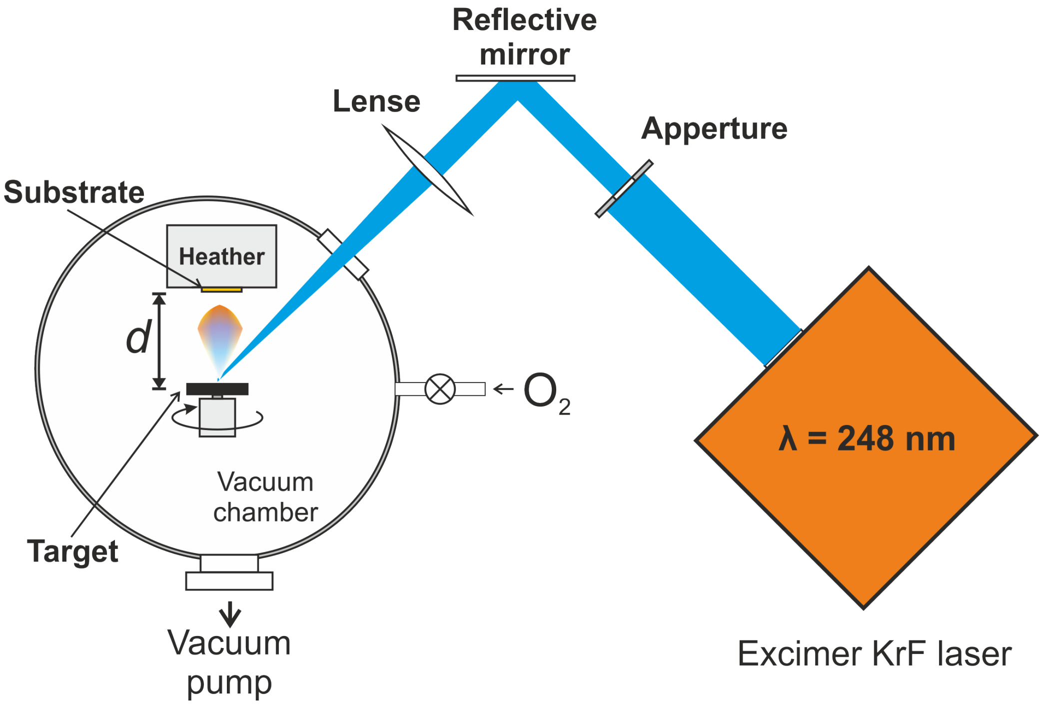

Figure 14: Schematic diagram of the pulsed laser deposition system.

Pulsed laser deposition (PLD) was used as a method of YBCO thin film preparation in this work. Main advantage of the PLD is preservation of the target composition (stoichiometry) [16]. Fig. 14 shows a schematic diagram of a typical PLD system. A laser pulse strikes a stoichiometric $YBa_2Cu_3O_{7-x}$ target. When laser energy density is high enough (typically about 1–1.5 J/Cm^2), the target material is ablated and produces a plasma plume near the surface of the target. Part of the ablated material is absorbed on a substrate that is heated to high temperature and placed in the vicinity to the target(typically 4–5 cm). The result is the deposition of thin film of YBCO materials with the same composition as the target [16]. High temperature is required for both formation of right chemical phase and epitaxial growth of the film.

In order to obtain high-quality YBCO thin films the following parameters should be accurately controlled: substrate temperature T_S; energy density of the laser beam at the target J; oxygen pressure in the chamber during the deposition process, P_{O2}. Another important parameter is the target-to-substrate distance d_{TS} (typically in the range 4–6 cm), providing proper position of the substrate in the plume to maintain stoichiometry. The deposition rate depends on the energy density at the target, d_{TS}, and oxygen pressure and typically is 5–10 nm/min.

In most PLD systems excimer lasers are employed for target ablation. It is a gas filled laser typically with the gas mixture KrF and wavelength of 248 nm. An aperture is placed across the beam so that the non-uniform edge effects can be minimized [16].

In order to obtain high quality high-T_c films for SQUID-based devices, one should choose suitable substrates. To provide conditions of the epitaxial growth the mismatch between lattice parameters of the YBCO and substrate should be minimized. The best candidate for low frequency applications is the strontium titanate $SrTiO_3$ (STO). STO has a cubic perovskite structure with the crystal lattice parameters $a = b = c = 3.905$ Å. Other possible substrate materials candidates for deposition of thin YBCO films are Al_2O_3, YSZ (yttria-stabilized zirconia) and MgO, but in this case deposition of the buffer layer between the substrate and YBCO is needed to prevent chemical interaction. YSZ and CeO_2 are examples of suitable buffer layers for YBCO.

In this work, an ultra-high vacuum pulsed laser deposition system (DCA Instruments) was used to grow thin YBCO films. The system consists of an excimer KrF laser with a wavelength of 248 nm and pulse duration 16 ns. An aperture and long focus lens are used to form 1×4.2 mm^2 size laser beam spot on the target. The vacuum chamber is equipped with a turbomolecular pump with the pressure of 8×10^{-9} Torr. A mass flow controller is used to provide a regulated oxygen pressure during the deposition. The heather using a SiC element can provide uniform radiation heating of the substrates (with sizes up to 2″) up to 900 °C with the accuracy of 0.5 °C. The substrate during the deposition is placed in a sapphire receptacle in the holder with its surface down. Because of the radiation heating, there is no need to use any thermo-conducting paste, so the backside of the sample remains clean after the process. The substrate holder can perform rotation and scan movement above the plume to obtain a uniform distribution of the film thickness. The PLD chamber is one of the parts of the cluster deposition system (DCA Instruments) which contains also loading and transportation part and magnetron sputtering systems for *in-situ* deposition of oxides and metals.

A short description of the deposition process is presented below. Preparation procedure for substrates consists of ultrasonic cleaning in acetone and isopropanol together with mechanical cleaning. After this substrates were washed with deionized water and dried in the nitrogen flow. After the loading, substrates were slowly heated up to the deposition temperature (see Table 2) at 0.6 mbar oxygen pressure. The depositions were done at 10 Hz pulse frequency with the number of pulses needed to obtain desired thickness (4000 pulses correspond to 250 nm of the YBCO film thickness). An annealing procedure followed after the deposition at the 960 mbar of oxygen and substrate temperature 550 °C. After this, obtained samples were slowly cooled down to room temperature. Thin 20 nm protective layers of Au were *in-situ* deposited on top of YBCO if it was needed.

Table 2: YBCO layers deposition parameters

Substrate temperature T_S	780 °C
Energy density on the target J	1.38 J/cm^2
Oxygen pressure P_{O2}	0.6 mbar
Target-to-substrate distance d_{TS}	52 mm
Pulse frequency f	10 Hz
Number of pulses N	4000
Deposition rate, Å/pulse	0.6
Annealing T_S	780 °C
Annealing P_{O2}	960 Torr
Annealing time	60 min

Insulating and buffer oxide layers were deposited in the same cluster system using RF sputtering. Buffer layers were deposited *in-situ* with the YBCO layer in the same vacuum cycle. The deposition parameters are listed in the Table 3. After the deposition, the samples were slowly cooled down (10 °C/min) at an oxygen pressure 660 mbar.

In order to pattern the YBCO film, UV photolithography and dry Ar^+ ion beam etching (IBE) were used. The patterning process is schematically presented in the Fig. 15. Positive Shipley 1813 photoresist was spun on the substrate at 6000 rpm and baked at 95 °C for 3 min. Thick photoresist layer on the edges of the samples was removed using special frame mask. An MJB3 Carl Suss mask aligner with a wavelength 400 nm was used to perform photolithography. Exposure times were 30 s for the frame mask and 11 s for the actual device (20 s and 6 s in case of using Au layer). Exposed photoresist was removed using MF-319 developer (50 s for thick layers on the substrate edges and 35 s for small $\leqslant$2 μm structures).

Samples with the photoresist masks were mounted on the IBE stage using S1813 as a glue. Before etching the milling systems was pumped down to base pressure of 2×10^{-7} Torr. The beam and accelerating voltages were 250 and 300 V, correspondingly. The beam current was 13 mA and the measured current density was 0.17 mA/cm^2. The incident beam angle during etching was 30°. The cooling stage rotated during the etching with the rotation speed of 3 rpm. The calibrated etching rate for YBCO under these parameters was

Table 3: Buffer and insulating layers deposition parameters

	CeO_2	STO	PBCO
Substrate temperature T_S, °C	750	750	750
Gas pressure P, mbar	0.1	0.1	0.1
% Ar	100	40	80
% O_2	–	60	20
Power of RF source, W	50	100	50
Target-to-substrate distance, mm	30	35	35
Deposition rate, nm/min	1.5	3	4.5

4 nm/min.

2.3 Post exposure baking

The first attempts to fabricate multilayer high-T_c superconducting structures were performed using ion beam etching (IBE) combined with post exposure baking (PEB) of the photoresist mask. PEB is an additional baking of the photoresist mask at temperatures 120–150° C after the exposure that makes the edges of the mask more round. IBE with large incident angle (45°–60° to the surface normal) performed through such mask allows to form shallow slopes of the superconducting electrodes. The minimum slope angles of the bottom high-T_c superconducting electrode obtained using this method were close to 20° [50, 30, 51]. PEB was used by several groups to fabricate high-T_c superconducting multilayer flux transformers [50, 30, 52, 38].

We use PEB as a preliminary step for fabrication of low-angle steps. A test layout consisting of four pairs of intersecting bridges (with 5, 20, 100 , and 200 μm line width) separated by an insulator was developed. Fabrication details and electrical characterization of fabricated crossovers are presented below.

First, we investigated how the slope angle of the edge of the photoresist mask depends on baking temperature. Photoresist test structures of the bottom electrodes were baked at different temperatures after development. The obtained edges of the photoresist masks were investigated using atomic force microscopy (AFM). Fig. 16 shows typical AFM micrograph and a cross-section of the edge of photoresist mask after baking at 140° C for a 5 min. The red markers on the cross-section indicate positions where the angle (25° for this sample) was measured. Obtained dependence of the slope angle of the edge of the phoresist mask as a function of PEB temperature is shown

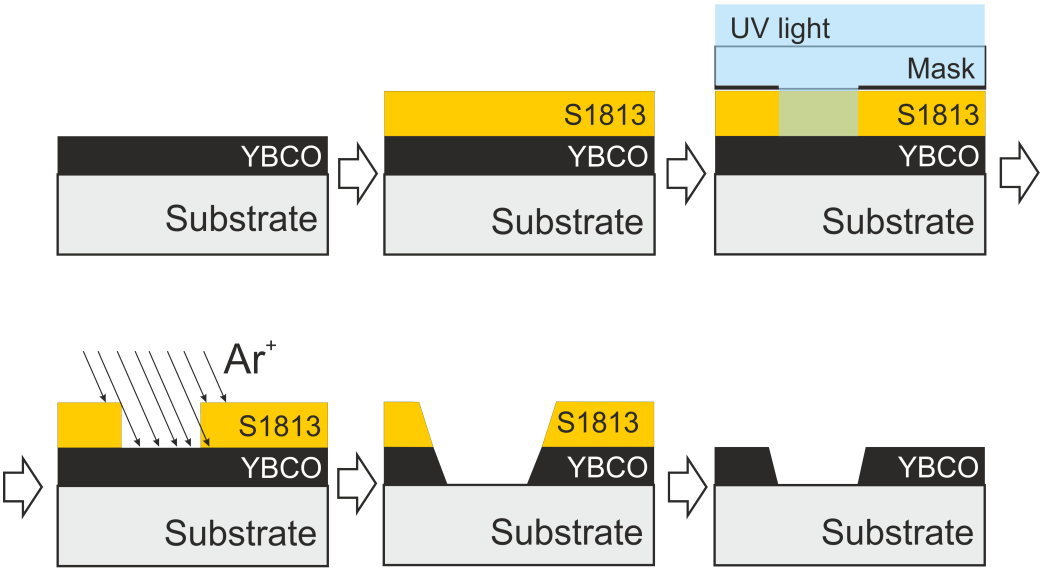

Figure 15: Schematic of the patterning process (the figure is not to scale).

in the Fig. 17. We found that the slope angle decreases with the increasing of the temperature up to 140° C where it reaches its minimum value. We did not find a strong dependence of the slope angle on the baking time and typically baked samples for 5 min.

Fig. 18 shows the AFM micrograph and a crossection of the edge in the bottom YBCO electrode fabricated using PEB and IBE. 300 nm thick YBCO films were deposited on 5×5 mm^2 STO substrates. After the photolithography and PEB (140° C, 5 min), samples were etched using IBE (angle of beam incidence was 45° to the surface normal). The obtained slope angle of the YBCO electrodes was 24°. As can be seen in Fig. 18, there is a redeposited material on the edges of the etched electrode. After dissolving the photoresist in acetone, it can form sharp ”fence” along the edge of the electrode. It is very hard to remove it and it can form a shorts between layers.

After the fabrication of the bottom electrode, $SrTiO_3/PrBa_2Cu_3O_7/SrTiO_3$ (SPS) insulating trilayers were deposited using RF sputtering with deposition parameters listed in Table 3. The thicknesses of the layers were 30 nm for both $SrTiO_3$ (STO) sublayers and 270 nm for the $PrBa_2Cu_3O_7$ (PBCO). After the deposition of the insulator, a 300 nm thick top YBCO layer was deposited *in-situ* by PLD. Top YBCO film was patterned to form bridges crossing the bottom YBCO lines. The insulating layer was etched in order to open corresponding contact pads in the bottom YBCO electrode. Finally, Au contact pads were fabricated on both top and bottom superconducting electrodes using dc sputtering, and lift-off.

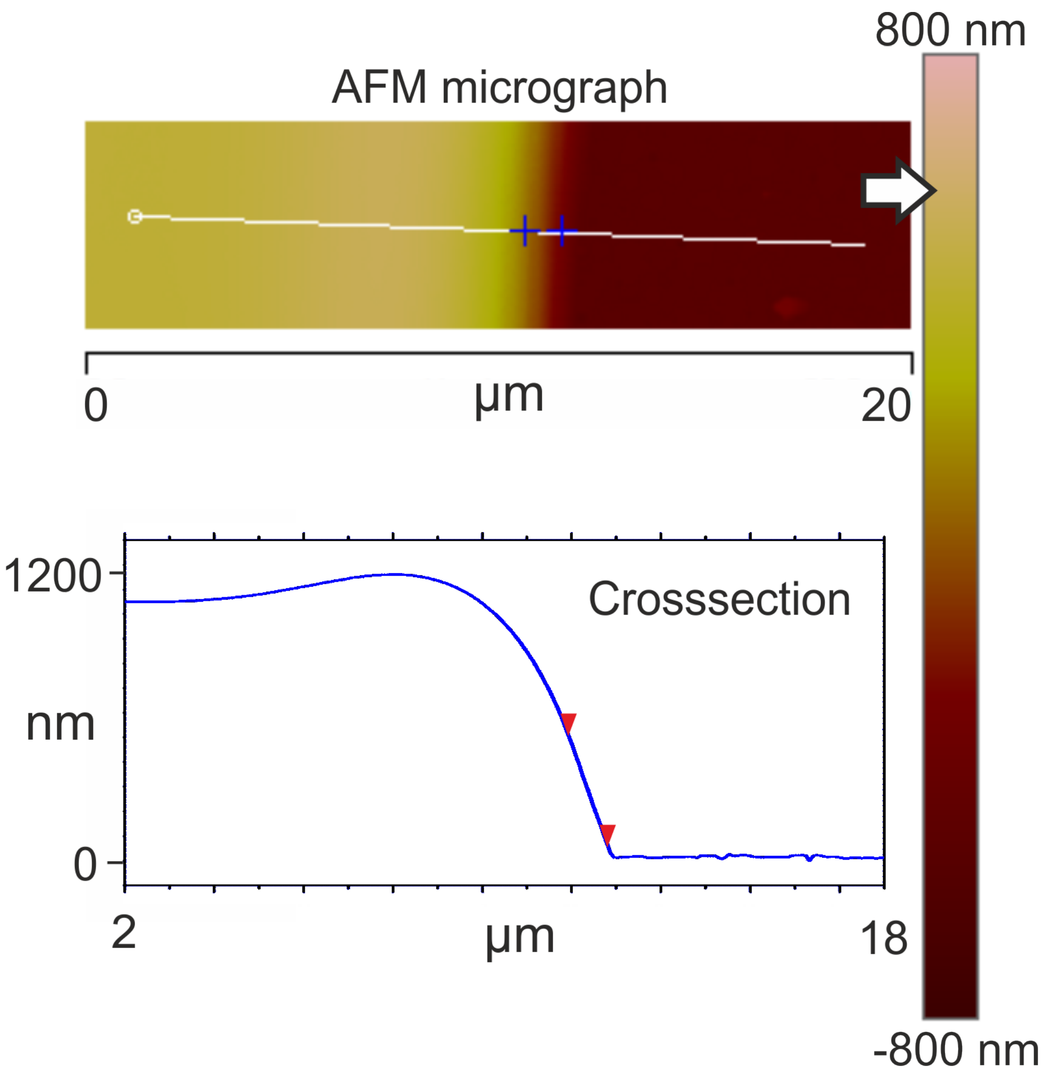

Figure 16: AFM micrograph and a crossection of the edge of photoresist mask after baking at 140 °C. Red markers in the cross-section indicate the positions where the angle was measured.

Electrical properties of fabricated YBCO/SPS/YBCO crossovers were investigated at 77 K. Critical temperatures, T_c, of the both bottom and top electrodes were measured. Critical currents of crossovers were also measured and critical current densities J_c were calculated. Table 4 presents the room temperature resistance R^{300}, T_c, and J_c of the 5 μm crossover. Low J_c values of the top electrode can be explained by the presence of grain boundaries with large misorientation angles between the YBCO film on the slope and the film on the flat parts of the crossovers [49]. Presence of defects in the

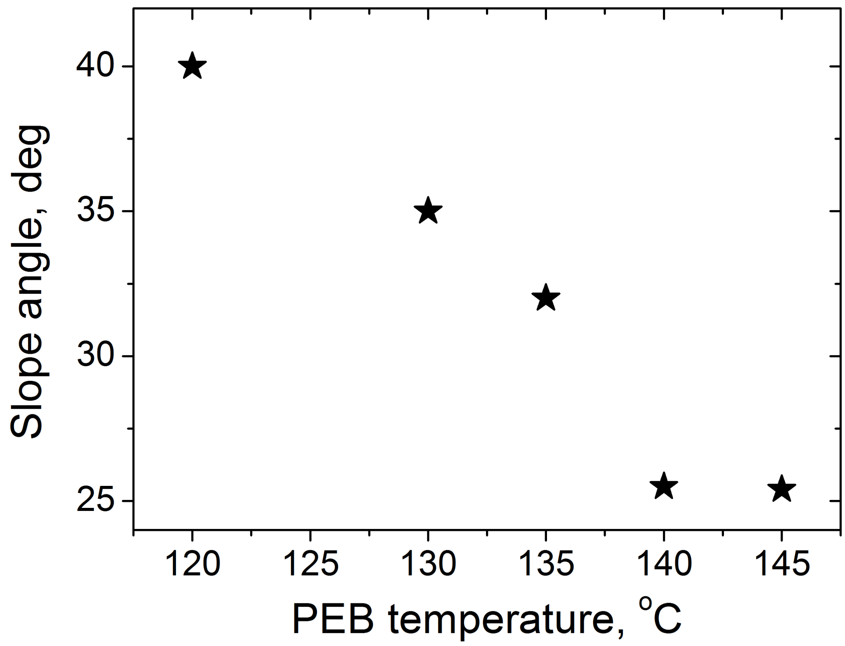

Figure 17: Dependence of the slope angle of the photoresist mask as a function of the PEB temperature.

YBCO film on the slopes can also decrease the critical current density.

The resistance between bottom and top YBCO electrodes at 77 K was measured to 15×10^3 Ω (for the 5 μm crossover). For crossovers with larger overlap area (20×20, 100×100, and 200×200 μm^2) the resistances between superconducting layers were much lower (typically 15–20 Ω) because of presence of shorts between layers through droplets on the surface of the bottom electrode.

Table 4: Electrical and superconducting properties of the YBCO electrodes of the 5 μm crossover fabricated using PEB

	bottom YBCO	top YBCO
R(300 K), Ω	544	123
T_c, K	89	84
J_c, A/cm^2	2×10^6	10^4

In conclusion, we found that minimal slope angle of the bottom super-

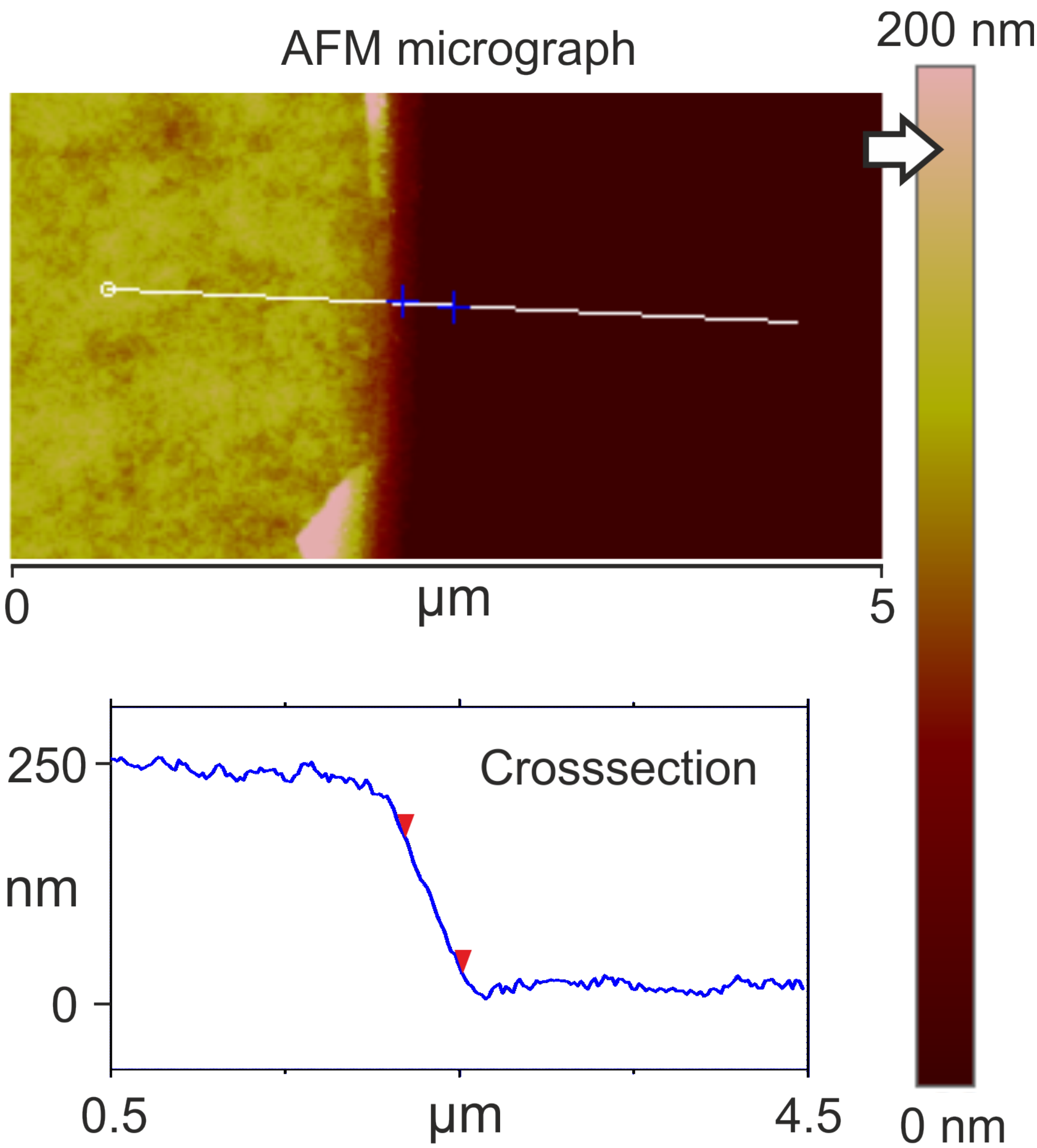

Figure 18: AFM image and a crossection of the edge of the YBCO fabricated using PEB and IBE. The red markers on the cross-section indicate positions where the angle was measured.

conducting electrode that can be obtained using PEB combined with IBE is 24°. For this angle, grain boundaries may be formed in the crossover and result in two orders of magnitude lower critical current densities compared with the bulk YBCO film [49]. Therefore, we conclude that this method is not suitable for flux transformer fabrication, but it can be used to obtain the initial low slope angles before using other methods of the treatment of the bottom electrode.

2.4 Anisotropic wet etching

Anisotropic wet etching was proposed as an alternative to the ion beam milling processes [53, 54]. This technique was used to fabricate ramp edge Josephson junctions [55, 56, 57, 58] and later was successfully implemented for other high-T_c superconducting multilayer structures [51, 28, 29].

A fabrication method consisting of a deep UV photolithography of $YBa_2Cu_3O_{7-x}$ and $PrBa_2Cu_3O_7$ films, combined with nonaqueous Br-ethanol chemical etching, was developed and successfully used for the fabrication of Josephson junctions, interconnects, and crossovers [54]. The slope angle of the resulting edges was about 3°. For crossovers the critical current density quantitatively corresponded to that of high quality YBCO epitaxial films.

This technique was used to fabricate multilayer high-T_c superconducting flux transformers with a transformation coefficient of 1 nT/Φ_0 on 10×10 mm^2 chips. The magnetic field sensitivity of magnetometers combined with such flux transformers was 15 fT/Hz$^{1/2}$ at 1 kHz and 35 fT/Hz$^{1/2}$ at 1 Hz for an 8×8 mm^2 pickup loop and 3.5 fT/Hz$^{1/2}$ at 1 kHz and 7 fT/Hz$^{1/2}$ at 1 Hz for a 16×16 mm^2 pickup loop [39].

Despite the significant improvement in the magnetic field sensitivities of the sensors, this technique has some disadvantages. First, Br-containing solvents are hazardous. Bromine is highly toxic, irritating, reactive, corrosive and oxidizing and Br-methanol solution requires extreme care when it is handled. It is also often forbidden to use in a university environment. Br-methanol solution is an anisotropic etchant of the YBCO and the etching rate in *a*-*b* plane is much higher than in the *c*-direction. This means that the presence of *a*-outgrowths will lead to the appearance of holes in the etched structure. Also if one uses the STO as an insulator the etching of the windows in the insulating layer should be done using IBE [28], thus increasing the slope angle and which may contaminate the edges by redeposited material.

Because of the safety regulations we were not able to use this technique for fabrications of multilayer high-T_c flux transformers.

2.5 Chemical-mechanical polishing

Both PEB and wet etching methods described above have many advantages and SQUID magnetometers with multilayer flux transformers, fabricated using these methods, demonstrated very high magnetic field sensitivity. On the other hand, both techniques demand very smooth surfaces of the thin films and generally do not provide any surface treatment of the electrodes during fabrication process. The presence of precipitates, droplets and redeposited material on the edges of the electrodes (in case of using IBE) can lead to the formation of galvanic shorts between the superconducting layers. The roughness of $YBa_2Cu_3O_{7-x}$ films obtained using pulsed laser deposition (PLD) is a well-known problem [59, 60, 61]. It is very difficult to tune the deposition parameters to avoid formation of the droplets on the surface of the film. This imposes strict requirements on every deposition step of the fabrication process and reduces the reproducibility of the methods.

The chemical-mechanical polishing (CMP) was suggested for fabrication of high-T_c multilayer structures as an alternative approach [62, 63, 64, 65, 66]. First attempts to use polishing in process of fabrication of high-T_c multilayer structures were performed in Chalmers University of Technology [62, 67]. It was shown that it is possible to create planarized YBCO/PBCO/YBCO structures by depositing YBCO in ion-milled trenches in substrates and polish mechanically with 0.25 μm diamond spray. The planarized layers served well as templates for epitaxial growth of an insulator layer and a top superconducting layer. Crossovers, free of high-angle grain boundaries, were demonstrated and showed critical current densities, J_c, of $\leq 2.5\times10^6$ A/cm^2. However, this method is not suitable for fabrication of vias because it cannot create shallow slope angles of the edges of the bottom electrode which are needed to obtain contacts between superconducting layers with high J_c.

Takashima *et al.* used CMP on the insulator to fabricate multilayer YBCO/STO/YBCO structures [63, 68]. Two-stage polishing of the STO surface was carried out; first, rough polishing with slurry of 0.5 μm diameter and then the fine polishing with slurry of 0.1 μm diameter [69]. The slope angle of the STO deposited on the lower YBCO stripline after CMP was less than 1°. The electrical characterizations of the fabricated crossovers demonstrated that the critical temperature, T_c, of the top YBCO layer was 88.5 K, and that of the bottom YBCO layer was 88 K. The critical current density, J_c, of all YBCO layers was 2×10^6 A/cm^2 at 77 K, which is the same as that for a single layer YBCO films. Finally, Takashima *et al.* demonstrated a multilayer YBCO/STO/YBCO SQUID magnetometer fabricated using CMP, but their device has only a single-turn input coil without a via [70]. The noise level was 200 $\mu\Phi_0/\mathrm{Hz}^{1/2}$ at 100 Hz and 20 $\mu\Phi_0/\mathrm{Hz}^{1/2}$ at 1 kHz.

Wada *et al.* used the CMP technique for YBCO/PBCO/YBCO trilayer junctions fabrication [65, 71, 72]. They used 0.03 μm alumina abrasive to polish YBCO and insulating PBCO layers. The slope angles of 3° were demonstrated after 5 min of polishing. The developed process had four polishing steps for both improving film smoothness and obtaining shallow slopes of the

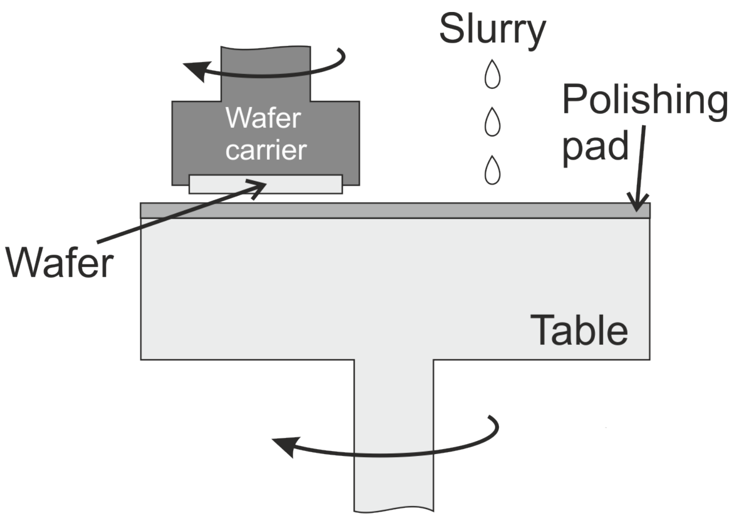

Figure 19: Chemical mechanical polishing of the surface of a wafer.

edges of the bottom YBCO and PBCO. In summary, full high-T_c superconducting YBCO/PBCO/YBCO trilayer Josephson junctions were fabricated using a polishing technique and demonstrated typical J_c at 4.2 K of 110 A/cm^2 [72].

Recently, Michalowsky *et al.* used CMP to improve the surface of YBCO films and showed that polishing does not lead to deterioration of the properties of the grain boundary junctions [73]. Shapoval *et al.* used CMP as an alternative approach for a sample preparation to investigate the internal structure of thin films [74].

Despite of the fact that CMP was demonstrated to be promising for high-T_c superconducting multilayer structures, it has never been used for a flux transformer fabrication. CMP has several benefits when compared to other techniques. CMP does not require hazardous chemicals like Br-ethanol and also improves surface smoothness of the bottom electrode, thereby reducing galvanic shorts. Therefore CMP was selected as a method of high-T_c superconducting and insulator layer treatment for multilayer flux transformer fabrication in this work.

CMP is widely used in semiconductor fabrication processes. It is a key enabling technology to generate extremely flat and smooth surfaces at several critical steps in this manufacturing process flow [75].

A schematic of a CMP machine is shown in Fig.19 [76]. It uses orbital, circular and lapping motions. The wafer is held on a rotating wafer carrier while the face being polished is pressed against a resilient polishing pad attached to a rotating table. For oxide or silicon polishing, an alkaline slurry of colloidal silica (a suspension of SiO_2 particles) is used as a chemical abrasive. The size of SiO_2 particles varies between 100 Å and 3 μm. The slurry is carried to the wafer by the porosity of the polishing pad. It chemically attacks the wafer surface, converting the silicon top layer to a hydroxilated form (with the OH^- radical) which is more easily removed by the mechanical abrasive [77]. Gross mechanical damage of the surface is prevented by the fact that the colloidal silica particles in the slurry are not harder than the oxide being removed. CMP uses nontoxic substances, has a good removal selectivity, and a good rate control [77].

CMP is applied for several types of structures in semiconductor fabrication processes: bare silicon before any processing starts, metallization, the intermetal layer dielectric, and process silicon with dielectrics and metals [77, 78].

Main characteristic of the CMP process is the removal rate which can be described by Preston's equation [76, 77]:

$$\frac{dT}{dt} = K \cdot \frac{N}{A} \cdot \frac{ds}{dt} \tag{14}$$

where T is the thickness of the wafer, N/A is the pressure produced by the normal force on the area A, s is the total distance traveled by the wafer, and t is the elapsed time. This equation means that the removal of the wafer material is proportional to the pressure and the velocity of the rotation. Any physical considerations are put into Preston's constant K, which is often considered a proportionality constant (independent of pressure and velocity), but may also include the effects caused by the chemical reactions [77].

In this work a Logitech PM5 polishing machine [79] was used to fabricate test multilayer structure. The machine allows a variation of the rotating

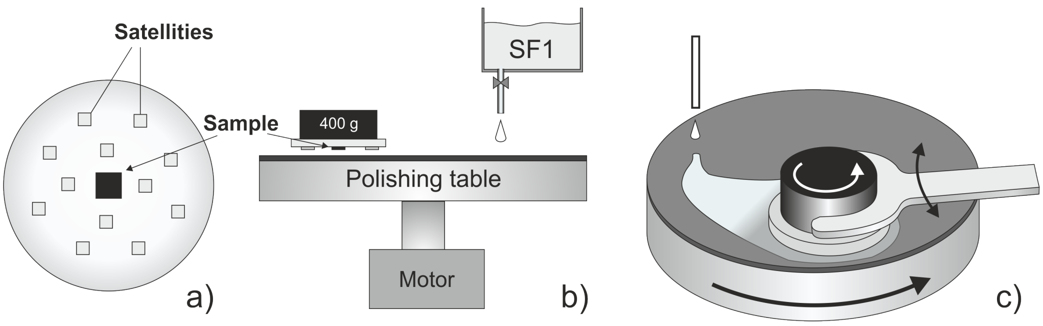

Figure 20: Scheme of the chemical mechanical polishing. a) - Position of the sample and satellites on the glass holder, b) - polishing scheme, c) - movement of the polishing plate and sample.

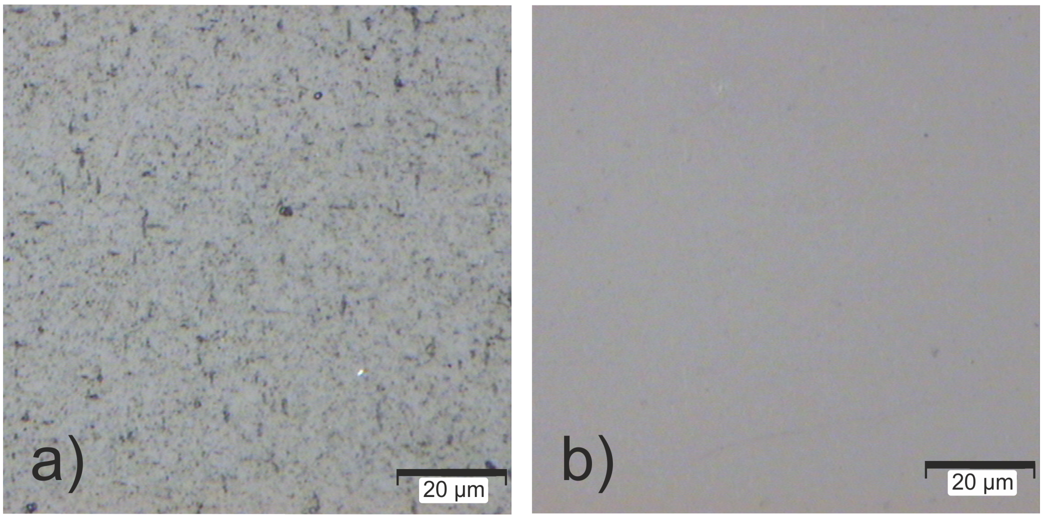

Figure 21: Optical photographs of single layer 300 nm - thick YBCO film (a) before and (b) after 2 min of CMP.

speed from 0 to 70 rpm with a loading weight from 0 to 2800 g. The polishing pressure can be set according to the size and the structure of the sample [74]. The rotating table was covered with the soft porous polyurethane pad (chemocloth Logitech).

Samples were mounted on a glass carrier disk (4″) using thin film wax (Ocon-195, Logitech). During mounting/unmounting of the substrates carrier was heated up to 110 °C to melt the wax. Several blank STO substrates (satellites) were mounted together with the sample to provide uniform distribution of the loading weight (see Fig. 20 (a)).

Logitech SF1 polishing suspension was used in the process. It is the alkaline colloidal silica for polishing silicon wafers and it is consisted of formaldehyde (<1.0%), ethylene glycol (4%–5%), and amorphous silica (15%–50%) [80]. The size of the amorphous silica particles is 20–140 nm. After polishing the samples were washed under the flow of water and mechanically cleaned with a clean room wipes. Wax was removed using non-solvent Logitech Ocon-178 cleaner fluid.

During the very first experiments of the polishing YBCO we found that the removal rate is very high (up to 150 nm/min). It was very hard to adjust loading weight of the standard PP5D Precision Polishing Jig below 500 g. So it was decided to fix loading weight to 400 g that improved the reproducibility of the process and allowed to decrease the removal rates (see Fig. 20 (b)). During the polishing the carrier with the applied loading weight performs movement as it is shown in the Fig. 20 (c).

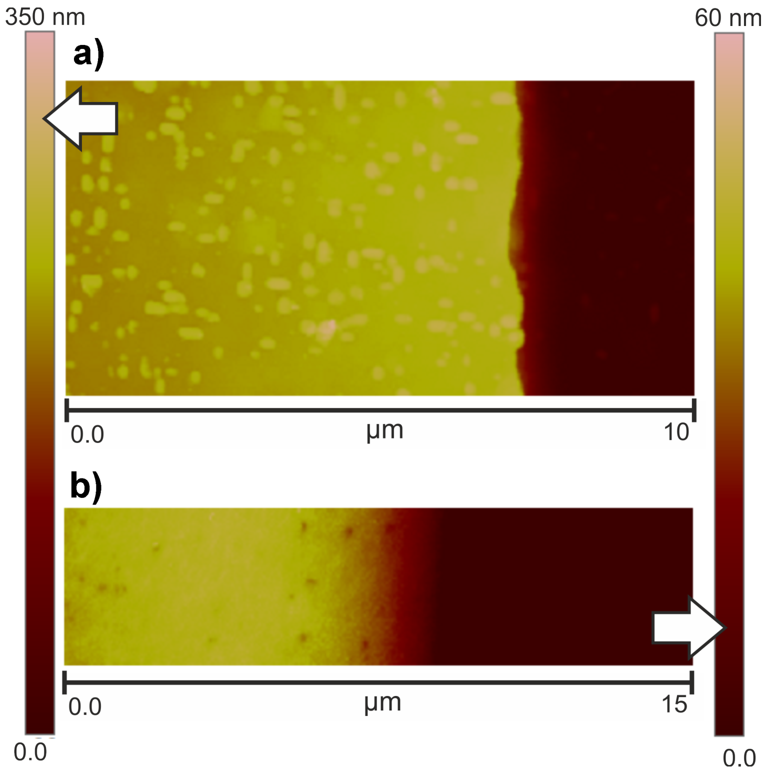

Figure 22: AFM micrograph of the edge of the YBCO structure before (a) and after (b) CMP.

First, CMP of the single layer thin high-T_c superconducting films was performed. 300 nm thick YBCO films were deposited on 5×5 mm^2 STO substrates as it was described in section 2.2. Optical micrograph in Fig. 21 shows that the surface of the YBCO film is greatly improved after the CMP. Measurements of the T_c of the film demonstrated that the superconducting properties did not change after the polishing process.

At the next stage, test structures consisting of lines with different widths were patterned in the 300 nm thick YBCO film. The sample was polished using 400 g weight and 10 rpm rotation speed. The AFM images of the YBCO structures before and after polishing are presented in Fig. 22 and Fig. 23. The slope angles of 2° were obtained after 2–5 min of polishing. An average roughness $R_a = 0.5$ nm of the YBCO film surface after polishing was measured using AFM. Together with decreasing of the slope angles the thickness of the films also reduced. For example the thickness of the 5 μm YBCO line (Fig. 23) after the CMP was 50 nm.

In order to investigate how the polishing parameters affect the resulting slope angles and thicknesses of the YBCO structures, the YBCO electrodes

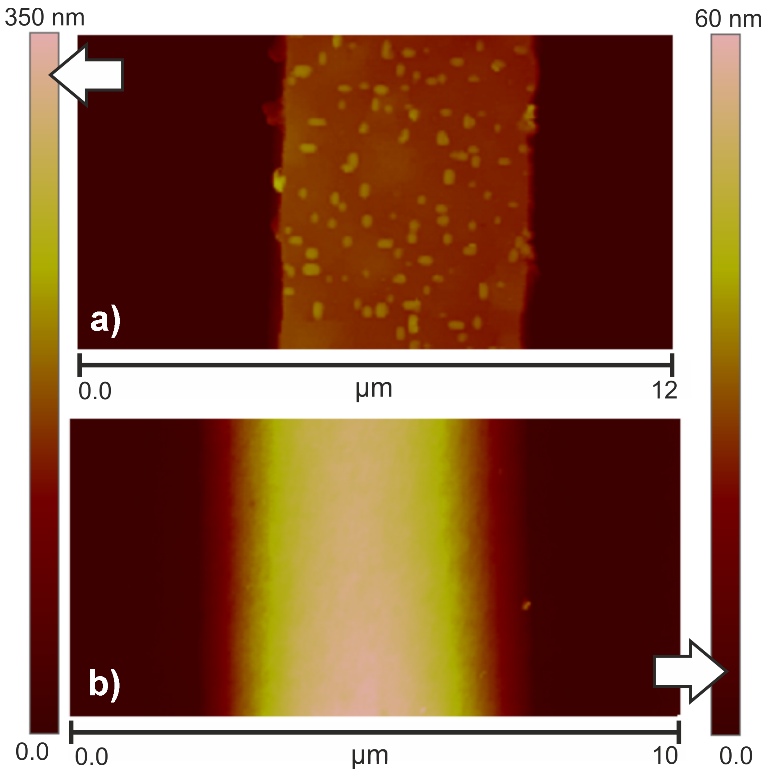

Figure 23: AFM micrograph of 5 μm YBCO line before (a) and after (b) CMP.

(lines with different width) were polished at different rotation speeds. Slope angles and thicknesses were measured after every minute of CMP.

The results of these investigations are presented in the Fig. 24. It was found that the slope angle has a non-linear dependence on the rotation speed (Fig. 24 (a)). To achieve slope angles below 2° the rotation speed should be increased that at the same time leads to a significant increase of the polishing rate (Fig. 24 (b)). With the total applied weight of 520 g (400 g of the loading weight and 120 g of the glass carrier) and 12 satellites, the removal rate of 60 nm/min was obtained at 10 rpm of the polishing table. The slope angles of YBCO electrodes after CMP performed using these parameters were 2–3°.

The geometry of the structures of electrodes plays an important role in the CMP. First, the width of stand-alone lines is limited by the need to keep reasonable thickness of the superconducting film. For a minimum thickness of the YBCO film of 100 nm and slope angle of 3°, the minimum line width is 4 μm. The slope angle depends on the distance between two adjacent structures as illustrated in the Fig. 25. When the distance becomes too small (about 10 μm in our conditions), the slope angle increases. Possible

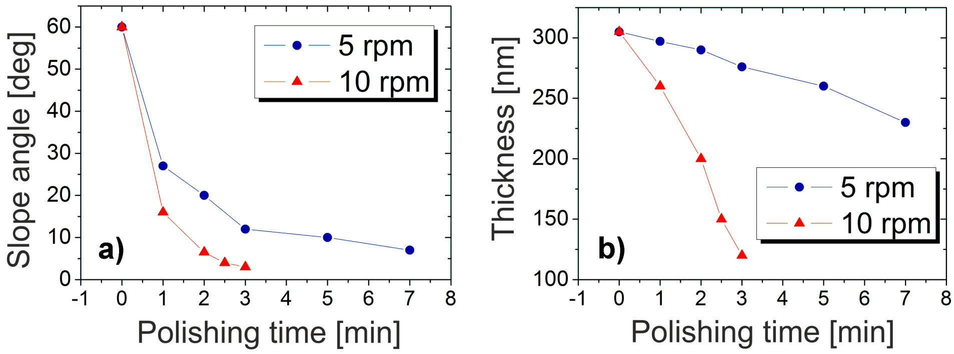

Figure 24: Slope angle (a) and the thickness (b) of the YBCO electrode as a function of polishing time for two different rotation speeds.

reason for this is that hardness of the polishing pad limits its ability to penetrate deeply in narrow trenches (Fig. 25 (b)).

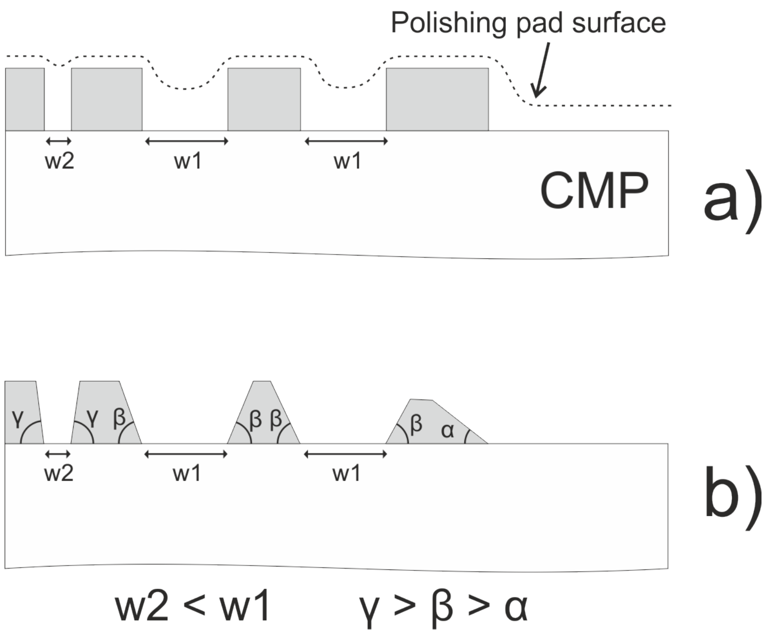

Figure 25: Schematic diagram of the CMP of the structure consisted of lines separated by different distances w. Distance w1 is larger then w2 that lead to the decreasing of the slope angle β compared with γ. The slope angle α is smallest compared with γ and β because this side of the line is treated during polishing more efficiently.

Special test marks were developed for visual estimation of the polishing progress. The marks are a set of concentric squares with different line widths patterned in the YBCO film together with the main structure. The marks enable quick visual evaluation of the electrode thickness and determination of when polishing should be stopped.

To make an interconnection between superconducting layers, a window in the insulator should be etched and polished. It is necessary to obtain shallow slope angles of the insulating layer edges and bottom superconducting electrode as well (see Fig. 13 b)). The main problem of the CMP of the insulator is the need to keep the thickness of the insulating layer. It was found that the top STO sublayer of the insulator stack works as an effective stopper for the CMP. The removal rate of the STO is much lower compared with the YBCO and PBCO [63, 68]. During CMP of the SPS trilayer, only top STO sublayer is removed that allows to keep necessary thickness of insulator.

Several YBCO/SPS/YBCO multilayer samples on 5×5 mm^2 STO substrates with test crossover and via structures were fabricated. Deposition and patterning of the thin superconducting and insulating films were performed as described in the section 2.2. PEB of the photoresist masks was applied before IBE of the bottom superconducting electrode and insulating layers to obtain the initial low slope angles.

Table 5: Electrical properties of the bottom and top YBCO electrodes of the crossover fabricated using CMP.

	bottom YBCO	top YBCO
R^{300}, Ω	914	481
T_c, K	89.5	90.5
J_c, A/cm^2	6×10^6	6×10^6

Electrical properties of bottom and top YBCO electrodes in the crossover fabricated using CMP are presented in the Table 5. The crossover was formed by two crossing YBCO 5 μm width lines separated by an insulator. The four-probe measurements of the bridges in bottom and top electrodes were done in liquid nitrogen. We found that there was no degradation of the superconducting properties during the fabrication process. The T_c of the bottom electrode increased after the fabrication process probably due to additional annealing during deposition of the insulator. Critical current densities of 6×10^6 A/cm^2 were calculated from the measured critical currents and known dimensions of the bridges.

Via test structures consisting of few interconnections between superconducting electrodes were fabricated. The test structures had windows in the

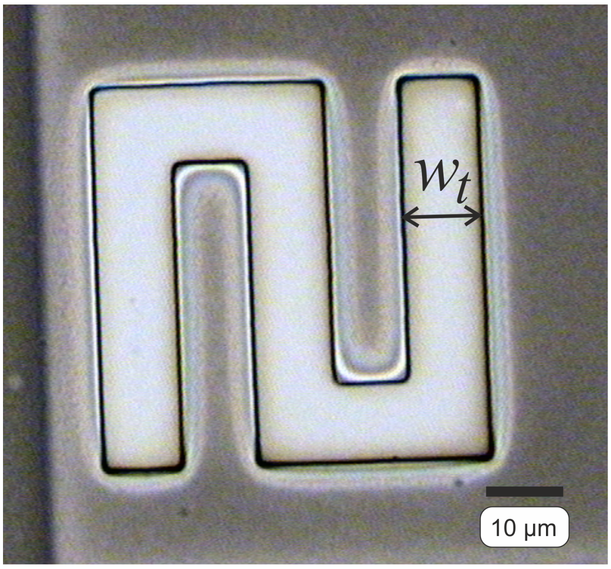

Figure 26: Optical photograph of the window in insulating layer after CMP. w_t denotes the width of the trench of the via.

insulating layer with different shapes and dimensions. Since the critical current density of the YBCO in the a-b planes is about 100 times higher than along the c-axis direction, the cross-sectional area of the via that dominates supercurrent transport is mainly defined by the perimeter of the window and overlap between the top and bottom electrodes on the slopes of the edges (see Fig. 13). Therefore the windows had meander-like shapes to increase the perimeter (see Fig. 26). The width of the trench w_t also varied for different windows.

Table 6 presents the characteristics of tested vias fabricated using the CMP. Maximum I_c of 80 mA was obtained on the via with w_t=10 μm. Vias with 5 μm wide trench had lower critical currents due to the larger slope angles of the insulator and bottom YBCO (dependence of the slope angle as a function of width of the trench was discussed above). Critical current density of interconnections with w_t=10 μm was estimated to be 1.2×10^5 A/cm^2. The critical current of 80 mA is sufficiently higher than the currents that would be induced by typical signals in biomagnetic application.

The microstructure of vias was investigated using high resolution transmission electron microscopy (HR-TEM), see Fig. 27. Selected area electron diffraction (SAED) investigations (see insets in the Fig. 27) of the top electrode showed that the top YBCO film has grains with a-orientation on the slope of the via. The rest of the top electrode had c-orientation. The dashed lines in Fig. 27 indicate the boundaries between regions of different orienta-

Table 6: Electrical characteristics of vias between bottom and top YBCO electrodes fabricated using CMP.

Outer dimensions, μm	Window area, μm^2	Perimeter, μm	Contact area, μm^2	w_t, μm	I_c, mA
50×50	1375	560	112	5	11
50×50	1700	360	72	10	80
25×30	500	210	42	5	7
40×45	1500	210	42	15	50

tion. A possible source of nucleation for a-oriented YBCO could be a bottom STO layer in the insulator stack.

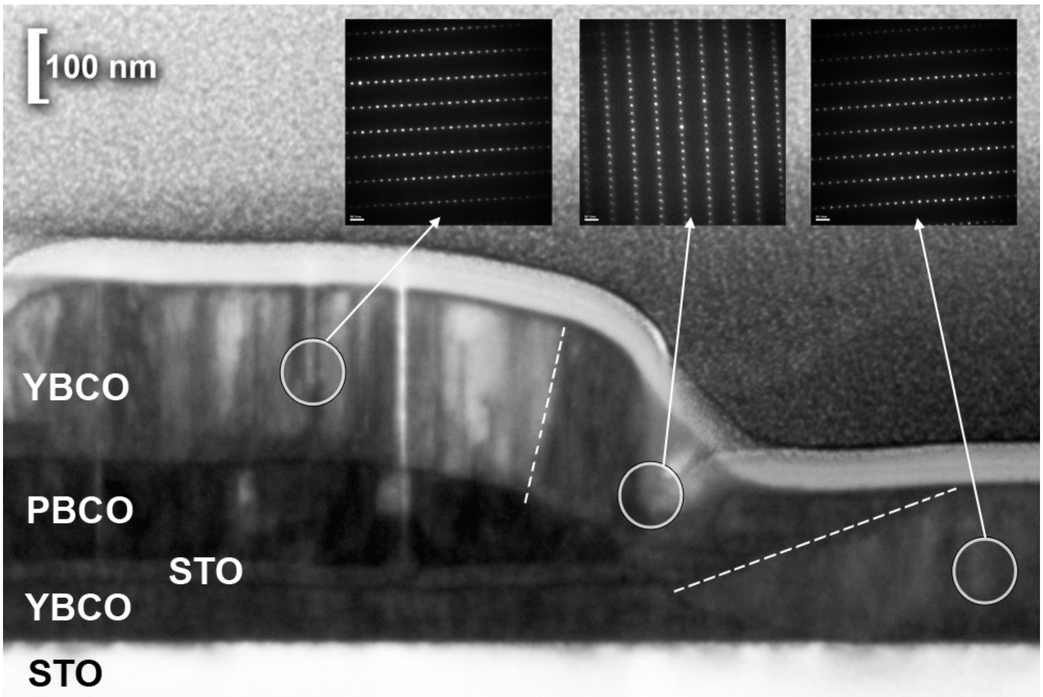

Figure 27: Cross-sectional high resolution transmission electron microscope image of interlayer connection (via) of the flux transformer presented herein. Insets show selected area electron diffraction (SAED) images from three different locations in the top YBCO electrode. Dashed lines indicate the boundaries between a-axis and c-axis oriented grains of the YBCO film.

2.6 Developed step-flow of the process

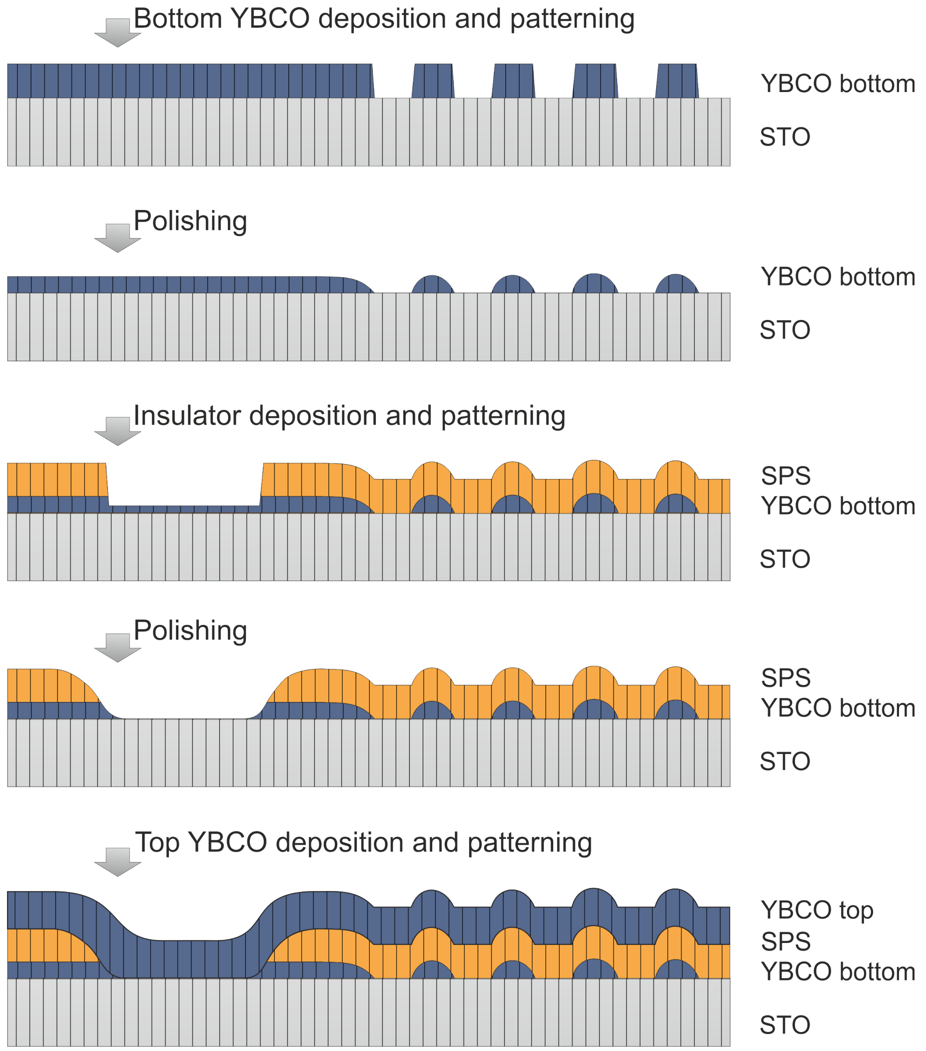

Figure 28: The step-flow of the developed multilayer process (the figure is not to scale).

A developed process for fabrication of high-T_c superconducting multilayer structures is presented in the Fig. 28. The process starts with the pulsed laser deposition of the bottom 300 nm thick YBCO film. After a patterning of the bottom electrode using post exposure baking and Ar^+ ion beam etching, the slope angles of the edges are 25–30°. The next step is polishing of the bottom electrode to obtain slope angles around 2°. The YBCO film thickness decreases to 120-150 nm. After that insulating STO/PBCO/STO (30 nm/270 nm/30 nm) trilayer is deposited using the RF magnetron sputtering. Windows in the insulator are etched using PEB and IBE. To form more shallow slopes of the edge of the YBCO layer, thin layers of superconducting film are left on the bottom of the etched windows. These layers are removed during second polishing procedure to form shallow slopes of the edges of the insulator. The last step is the deposition of the second YBCO layer (350 nm) with the subsequent patterning of the top superconducting electrode.

3 Flip-chip high-T_c SQUID magnetometers

3.1 Design of the flip-chip dc SQUID magnetometer

SQUID magnetometers with inductively coupled flux transformers were discussed in the section 1.7. To increase a coupling between flux transformer coil and SQUID loop, both SQUID and flux transformer can be fabricated on the same chip (integrated design). In this case the distance between input coil and the SQUID washer is limited only by the thickness of the insulating layer (typically few hundred nanometers). The integrated configuration provides the best coupling between the SQUID and input coil of the flux transformer and is commonly used with low-T_c materials. For high-T_c superconductors, fabrication of multilayer circuits is difficult due to the anisotropic properties of materials, high deposition temperatures, and outgrowths and particles in the film. Fabrication of grain boundary junctions (to form SQUIDs), crossover and vias (to make flux transformer) on the same chip are even more complicated tasks. Grain boundary Josephson junctions are very sensitive to environmental conditions and therefore adding more technological steps could affect the junction parameters and decrease the reproducibility of the manufacturing process. Therefore a flip-chip configuration can be used to separate fabrication processes of the SQUID and flux transformer. In the flip-chip configuration, the SQUID and flux transformer are fabricated on two different chips. The SQUID magnetometer is formed by attaching the two chips together. In this case the distance between the SQUID loop and input coil is larger as compared with the integrated configuration and this may decrease coupling. Misalignment of the SQUID and flux transformer could also decrease the coupling. Overall, this decreases the effective area of the SQUID magnetometer. However, the possibility to fabricate the SQUID and flux transformer on separate chips increases the reproducibility of the fabrication process – one can replace components independently and select the best SQUID and flux transformer from different fabrication batches. For this reason, flip-chip high-T_c SQUID magnetometers with superconducting flux transformers were used in this work. The SQUID and flux transformer design considerations are presented and discussed below.

Throughout the work, several designs of flip-chip magnetometers were developed in order to optimize transformation coefficient and magnetic field sensitivity. In this work we demonstrate final (FT6) version of the high-T_c flip-chip dc SQUID magnetometer. Some of the experiments described in this work were done with the previous version (FT4). FT4 samples have slightly different design, but were fabricated using the same fabrication process and demonstrated similar flux noise properties.

As described in the section 1.7, the flux transformer is the closed superconducting circuit consisting of a large pickup loop and a multiturn input coil that is inductively coupled to the SQUID. The design of the flux transformer is shown in the Fig. 29. The pickup loop is a rectangular frame with a line width of 0.3–1 mm [28, 30, 29]. The size of the pickup loop is limited by the substrate dimensions. The inductance of the pickup loop can be calculated using equation below [28]:

$$L_P = \frac{1.86}{\pi}\mu_0\left(\frac{D+d}{2}\right)\left[ln\frac{D+d}{D-d}+0.42\right] \tag{15}$$

where D and d are the outer and inner dimensions, $\mu_0 = 4\pi \times 10^{-7}$ T·m/A is the vacuum permeability. The effective area of the pickup loop is $A_P = D \cdot d$.

The input coil of the flux transformer is a concentric multiturn spiral coil. The inner turn of the input coil is connected to the outer turn by an interconnection line that can be fabricated in either top or bottom superconducting layer (Fig. 31). The inductance of the planar spiral coil with the inner diameter d_{in} and outer diameter d_{out} can be calculated using a modified Wheeler formula [81, 82]:

$$L_i = K_1\mu_0\frac{n^2 d_{avg}}{1+K_2\rho} \tag{16}$$

where K_1 and K_2 can be found in the Table 7; n is the number of turns; $d_{avg} = 0.5(d_{out}+d_{in})$ is the average diameter, and $\rho = (d_{out}-d_{in})/(d_{out}+d_{in}))$.

Table 7: Coefficients for the modified Wheeler expression.

Layout	K_1	K_2
Square	2.34	2.75
Hexagonal	2.33	3.82
Octagonal	2.25	3.55

Our flux transformers were designed for 10×10 mm^2 substrates that is a maximum standard substrate dimension in our fabrication process.(Our technology allows fabrication of YBCO films on larger wafers up to 2 inches and the flux transformer can be scaled in future to a larger size). The size of the pickup loop cannot be made 10×10 mm^2 due to edge effects during the growth of the YBCO films; 9×9 mm^2 is a maximum size that can be used. The line width of the pickup loop is 0.5 mm. The inductance of the pickup loop was estimated as L_P=20.5 nH using Eq. 15.

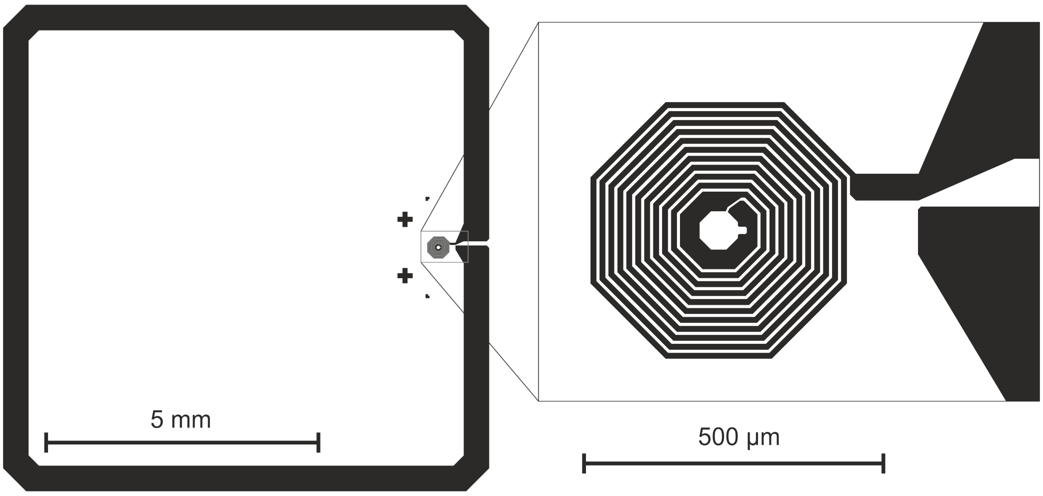

Figure 29: Layout of the top layer of the flux transformer (version FT6).

Software package 3D-MLSM was used to optimize the input coil. 3D-MLSM uses finite-element method on a triangular mesh with linear finite elements [83, 84].

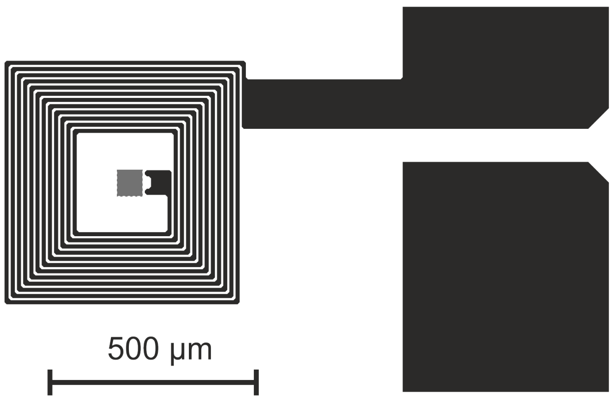

Figure 30: Layout of the input coil of the flux transformer (version FT4). The gray square indicate the center hole of the SQUID.

The central part of the spiral input coil should have an interconnection area that should fit the window in the insulator with a few hundred micrometers perimeter (see section 2.5). In an early design [85], the internal turn of the input coil was placed at 80 μm distance from the side of the center hole of the SQUID (see Fig. 30). This was done to keep the symmetry of the input coil and to obtain the size of the interconnection of 55×55 μm^2. Simulations using 3D-MLSM show that the mutual inductance (and as result effective area of the magnetometer) could be increased by widening of the line of the internal turn (see Fig. 29). In this case the distance between the side of the SQUID hole and edge of the turn is minimized. 3D-MLSM simulations demonstrated that this change in the layout increases the coupling coefficient by 15%.

The developed layout of the input coil is presented in Fig. 29 and 31 (c),(g). The octagonal spiral coil has 11 turns with the width of the line 10 μm and pitch 5 μm. The parameters of the input coil were chosen to match the inductance of the pickup loop. The inductance of the input coil of L_i=26.7 nH was calculated using Wheeler equation (Eq.16).

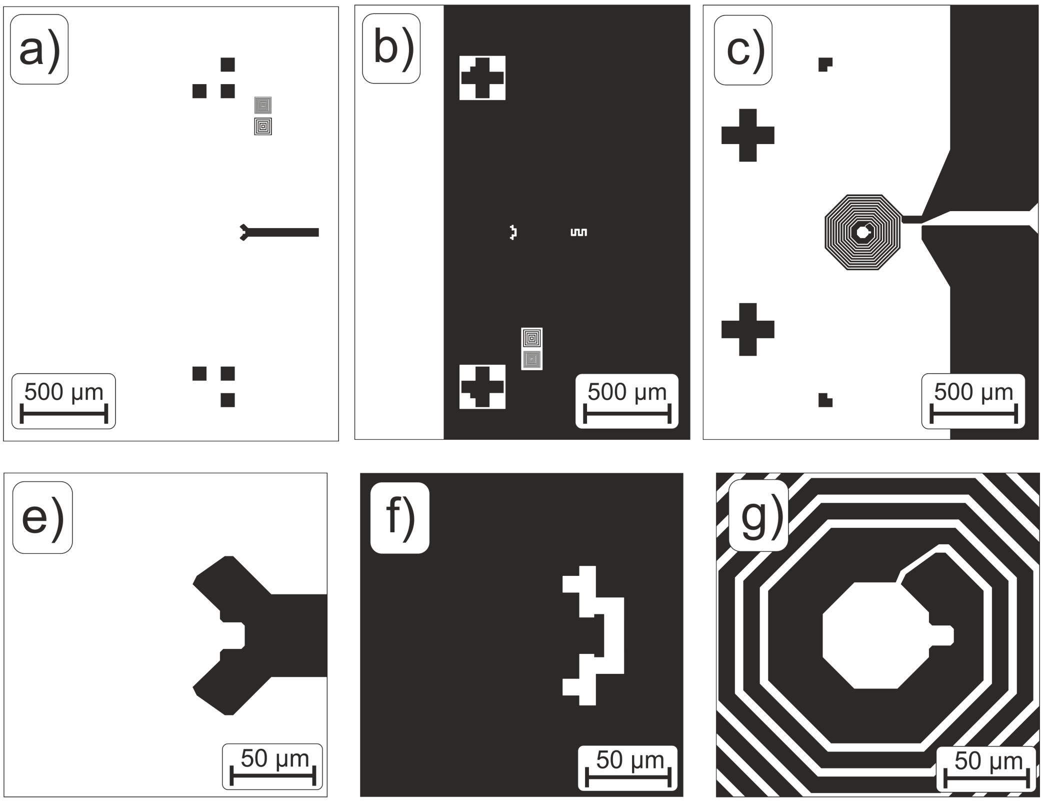

Figure 31: Layer-by-layer layout of the input coil of the flux transformer in two magnifications. The layouts are positive masks for IBE. a) and e) - bottom electrode, b) and f) - insulating layer, c) and g) - top electrode.

Zoomed layouts of both superconducting electrodes and insulating layer are presented in Fig. 31. The interconnection line is formed in the bottom electrode ((a) and (e) in the figure). The top electrode layer has a pickup loop and input coil and also has marks that are needed to align SQUID and flux transformer chips relative to each other. Both bottom electrode and insulator layers contain polishing marks to simplify CMP process (see section 2.5).

The design of SQUIDs on the 5×5 mm^2 bicrystal substrate is presented in Fig. 32. SQUIDs have 1280×1280 μm^2 octagonal washer and 60×60 μm^2 center hole that forms the SQUID loop. The washer has set of 3×3 μm^2 holes along the grain boundary to improve flux pinning and reduce low-frequency noise. Contact pads of the SQUIDs are placed on the edge of the chip in order to have a possibility to reach them when the flip-chip magnetometer is assembled. The SQUID inductance of L_S=110 pH was estimated using software package 3D-MLSM.

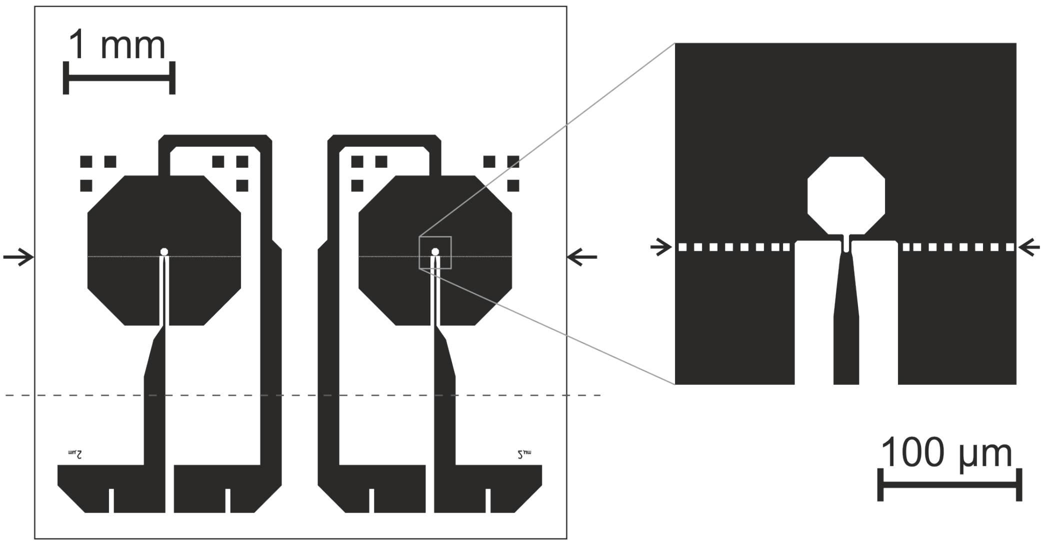

Figure 32: Layout of the SQUIDs on the 5×5 mm^2 bicrystal substrate. Arrows indicates the position of the grain boundary. Dashed line indicates the expected position of the edge of the flux transformer chip.

Using these parameters, an effective area of the designed SQUID magnetometer is estimated to be about A_{eff}=2.1 mm^2 using Eq. 12 and assuming a reasonable value of $\alpha = 0.8$ [30, 39]. This effective area corresponds to the transformation coefficient $1/A_{eff}$=1 nT/Φ_0. With the typical flux noise of high-T_c dc SQUIDs of 10 $\mu\Phi_0$/Hz$^{1/2}$ the magnetic field sensitivity of the designed flip-chip SQUID magnetometers can be estimated as 10 fT/Hz$^{1/2}$.

Multilayer YBCO/SPS/YBCO flux transformers were manufactured using developed fabrication process involving CMP as described in the Chapter 2. Some important details should be mentioned here. All flux transformers were fabricated on 10×10 mm^2 STO substrates with both sides polished in order to have a possibility to see the alignment marks during gluing together the SQUID chip and flux transformer.

Flux transformers were fabricated in small batches of 3 substrates each. During investigations, 5 batches were fabricated and 14 operational flux transformers were made. All fabricated flux transformers were operational and demonstrated very similar (depending on the version) properties. The obtained statistics indicates a very high reproducibility of the developed fabrication process.

To protect the YBCO film and to avoid unnecessary electrical contact with the SQUID washer, a protective 1 μm thick LOR3A polymer layer was spinned on the flux transformer chips.

SQUIDs were fabricated on 5×5 mm^2 or 10×10 mm^2 bicrystal 24° STO substrates. A CeO_2 buffer layer was used to improve the quality of the bicristal boundary before *in-situ* YBCO deposition. SQUIDs demonstrated high critical parameters and good stability during investigations.

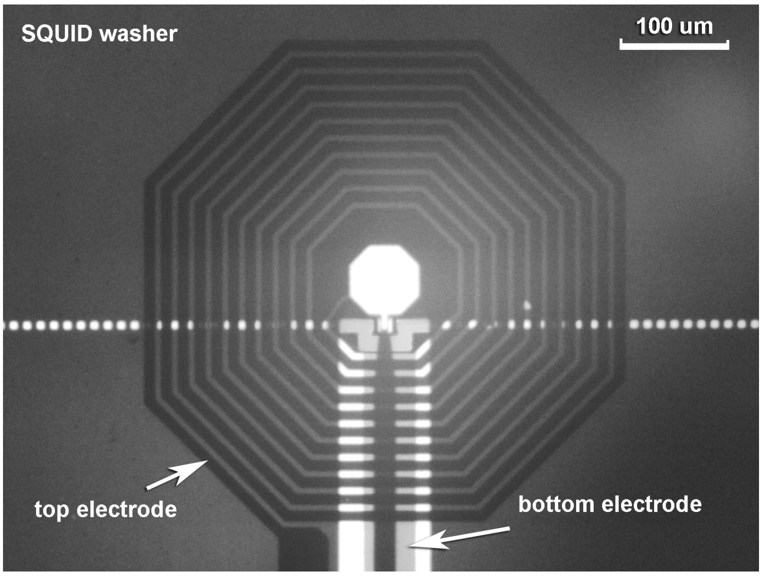

Figure 33: Optical image of aligned SQUID and flux transformer.

The alignment of the SQUID to the flux transformer chips was done manually using back-light stage and an optical microscope. To glue chips together, UV5 photoresist or BF2 (phenol formaldehyde and butyral resin dissolved in ethyl alcohol) were used. Both showed good gluing properties, but BF2 is not toxic and can be used without special precautions. Samples were left to dry at room temperature for 60 min after gluing. The disassembling of the flip-chip magnetometers can be done using acetone (for UV5) or ethanol (for BF2).

Distances between chips were measured using precision ball-gauge micrometer.. Typically their values were close to 3-5 μm. Significant deviations from the plane parallelism were not observed.

3.2 Electrical characterization

In order to evaluate the magnetic field sensitivity of the SQUID magnetometers, the effective area of the sensors should be first calibrated. To do this, magnetometer is placed in an magnetic field perpendicular to the magnetometer plane. A pair of Helmholtz coils with diameter 40 cm was used to form the uniform magnetic field (see Fig. 34). The Helmholtz coils had the current-to-field coefficient of 0.244 A/mT. A waveform generator was used to apply magnetic field to the sample during the calibration. The MAGNICON SEL-1 electronics was used to control and readout the SQUID [13]. The calibrations of the magnetometers were done either in 4-layers μ-metal shields or in the magnetically shielded room (MSR). All measurements were done in liquid nitrogen (77 K).

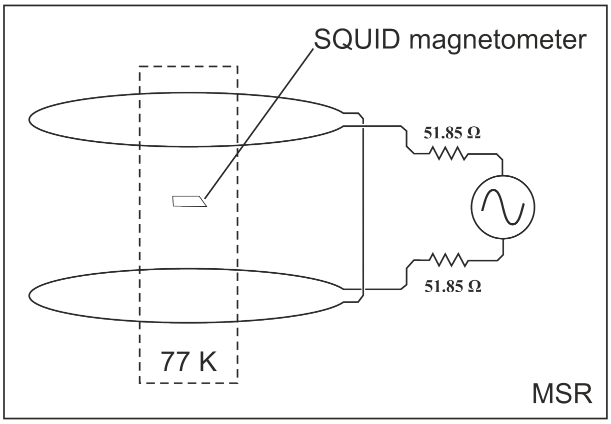

Figure 34: The schematic illustration of the calibration setup of the flip-chip SQUID magnetometer.

The current in the coil was adjusted to produce exactly one flux quantum in the SQUID loop (this can be easily seen from the sinusoidal SQUID output with period corresponding to one flux quantum). The transformation coefficient of 0.9 nT/Φ_0 was calibrated using the Helmholtz coils. It corresponds to an $A_{eff} \approx 2.3$ mm^2 that is very close to the estimated value. The difference can be explained by a larger coupling coefficient α than expected. To check flux transformer efficiency, transformation coefficient of a bare SQUID (i.e., without the transformer) was also investigated under the same conditions. It was estimated as 23 nT/Φ_0. Therefore the flux transformer increases the effective area of the SQUID by more than 20 times.

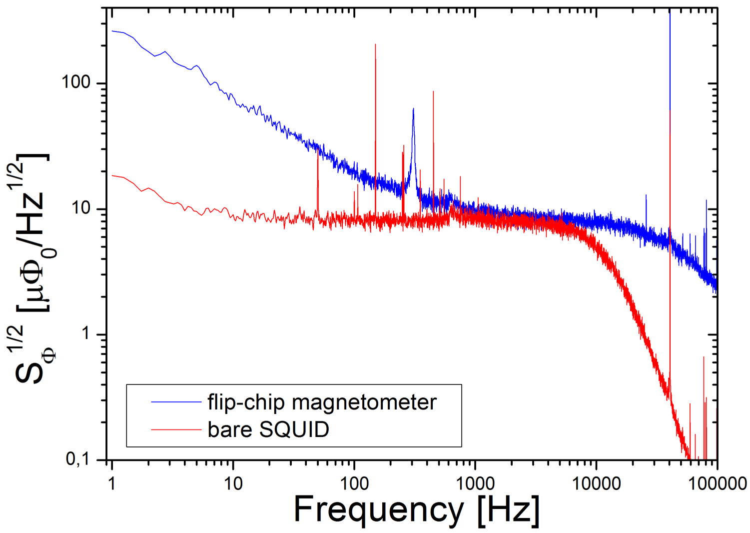

Figure 35: Magnetic flux noise spectra of the bicrystal dc SQUID (red) and the same SQUID coupled with the superconducting flux transformer (blue).

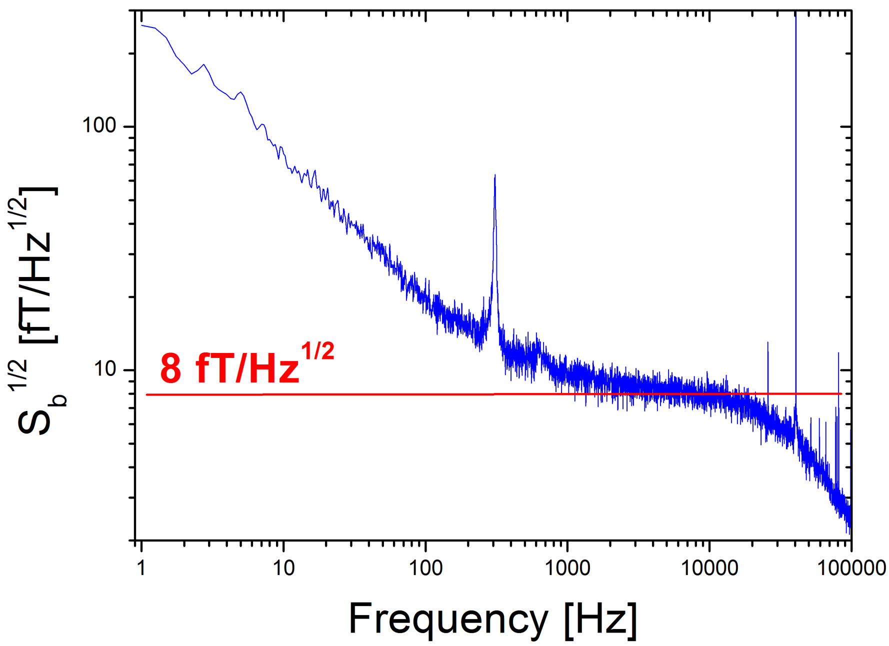

Figure 36: The spectral density of equivalent magnetic field noise of the flip-chip magnetometer measured in the MSR. Red line indicates the 8 fT/Hz$^{1/2}$ level.

Noise measurements were recorded with a Stanford Research 785 spectrum analyzer in the frequency range 0.1 Hz - 100 kHz. Samples were slowly cooled down to 77 K in the MSR. In order to reduce the critical current fluctuations in the junctions of the bicristal SQUID, the devices were operated with a bias reversal technique at 40 kHz [13].

Noise spectra of the flip-chip magnetometer and bare SQUID in ac-bias mode are shown in the Fig. 35. The bare SQUID (i.e., without the transformer) had a magnetic flux noise of about 10 $\mu\Phi_0/\mathrm{Hz}^{1/2}$ with a *1/f* cut-off frequency of about 10 Hz. When the SQUID was coupled to the flux transformer, the white noise level above 2 kHz remained the same (see Fig. 36) and corresponded to a magnetic field sensitivity of about 8 $\mathrm{fT/Hz}^{1/2}$. This is the best sensitivity achieved by high-T_c SQUID flip-chip magnetometer on a 10×10 mm^2 substrate. Below 1 kHz, excess *1/f* noise was observed that was not suppressed by the ac-bias. Similar $1/f$ noise was observed in all flux transformers fabricated and tested during the work.

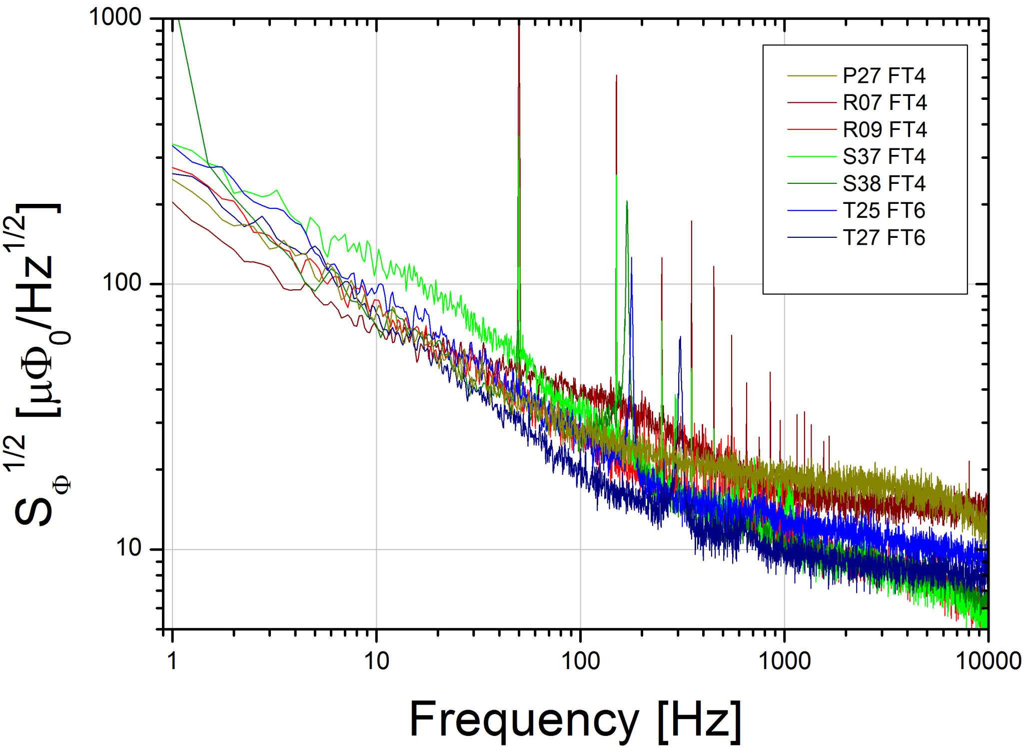

Figure 37: Magnetic field noise spectra of the flip-chip magnetometers.

Several flux transformers and SQUID designs were developed and electrically characterized. Fig. 37 shows noise properties of several different flip-chip SQUID magnetometers fabricated using the developed fabrication

Table 8: Parameters of the fabricated flip-chip magnetometers.

Sample ID	Version	SQUID type (a)	Transformation coefficient, $1/A_{eff}$, nT/Φ_0	$S_B^{1/2}$ (at 10 Hz), fT/Hz$^{1/2}$	$S_B^{1/2}$ (white noise), fT/Hz$^{1/2}$
P27	FT4	SQR05	3,9	304	70
R07	FT4	SQR10	2,3	158	33
R09	FT4	SQS42	1,6	134	15
S37	FT4	SQS42	1,85	223	15
S38	FT4	SQS42	1,95	135	17
T25	FT6	SQS42	1	95	10
T27	FT6	SQT24	0.9	76	8

process. Table 8 presents the parameters of the tested magnetometers and estimated magnetic field sensitivities. As can be seen, all of the fabricated devices have very similar excess *1/f* noise below 1 kHz.

To exclude the possibility of environmental origin of detected low-frequency noise we performed a number of experiments with different shielding conditions. A superconducting BiSCCO shield was used, together with the multilayer permalloy shields and MSR. The flip-chip magnetometers demonstrated the same *1/f* noise that allows us to attribute this excess noise to the presence of the flux transformer.

3.3 Investigation of low frequency noise

There are several possible sources of the *1/f* magnetic flux noise in our magnetometers. First, it can be caused by thermally activated motion of magnetic flux vortices in weak links in grain boundaries that may be formed in vias and crossover structures of the flux transformer. Another possibility is that the flux transformer can amplify stray magnetic field in a measurement setup that would increase probability of flux trapping in the SQUID washer. This will enhance the magnetic flux noise due to thermally activated motion of magnetic flux vortices in it.

The excess noise in the SQUID washer can be reduced by introducing holes and slots as it was demonstrated by Dantsker *et al.* [86]. In order to investigate this possibility, different layouts of SQUID washers were developed and fabricated.

Fig. 38 demonstrates the layouts of the SQUIDs with different types of washer structure: (a)– solid washer with holes along the grain boundary, (b)– slotted structure, and (c)–meshed structure (washer with holes). To prevent the motion of the vortices in the YBCO film or along the grain boundary the SQUID type (a) had the line of holes along it. Type (d) is a different SQUID concept that has no superconducting film on the grain boundary except at the Josephson junctions. All SQUIDs were designed for an earlier versions of the flip-chip magnetometer (FT4) and had slightly different parameters compared to the latest design (FT6).

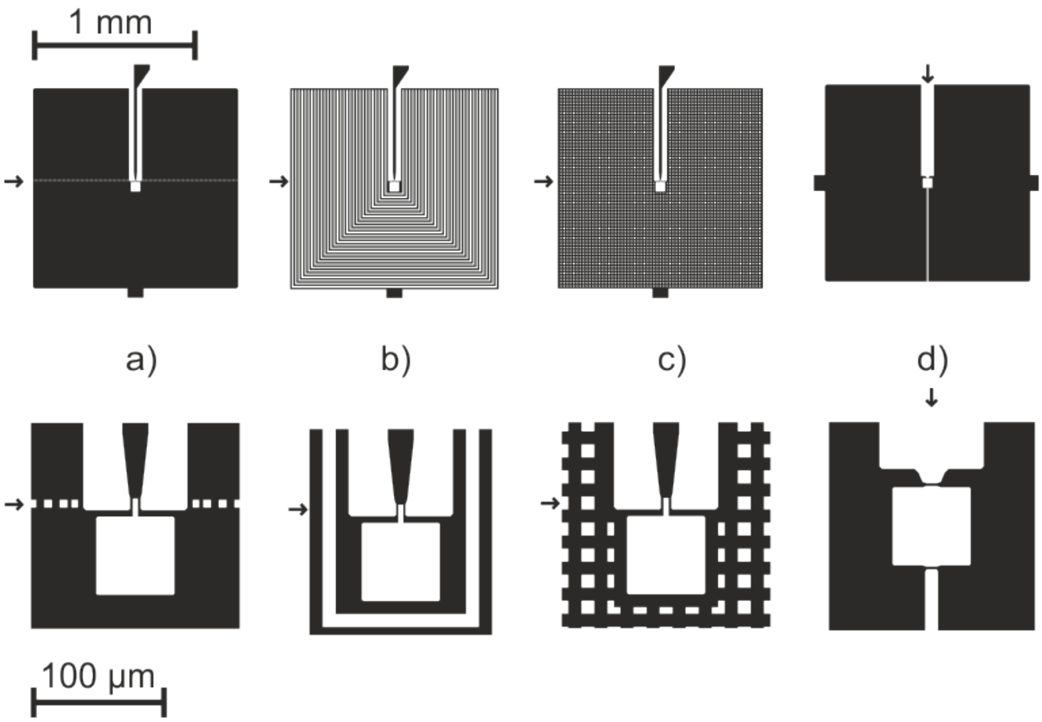

Figure 38: Layouts of dc SQUIDs with different washer configuration. Arrows indicate the position of grain boundaries.

Designed SQUIDs and assembled SQUID magnetometers (the same flux transformer was used for all SQUIDs) were calibrated in order to evaluate transformation coefficient, $1/A_{eff}$. Calibrations were performed as described above. Table 9 presents the results of the calibrations. SQUID type (a) with a solid washer demonstrated the largest effective area. The transformation coefficient of the flip-chip magnetometer with a type (a) SQUID was 1.6 nT/Φ_0. It is the best value obtained for this version of the flip-chip SQUID magnetometer.

At the same time, SQUID of types (b) and (c) demonstrated smaller effective areas. As was shown by Dantsker *et al.*, meshed and slotted SQUIDs have almost the same (or even larger) effective area compared to the SQUID with a solid washer [86]. A possible reason for the decreasing of the effective

Table 9: Transformation coefficients of the SQUIDs with different washer configuration.

SQUID type	$1/A_{eff}$ bare SQUID, nT/Φ_0	$1/A_{eff}$ SQUID + FT, nT/Φ_0
a	23	1.6
b	66	7.6
c	45	2.4
d	61	3.9

area in our case, can be the larger size of the holes and slots (10 μm compared to the 4 μm presented by Dantsker *et al.*). This, in turn decreases flux focusing effect of the washer.

The SQUID type (d) can be promising because its washer has no YBCO film above the grain boundary. It should reduce the noise originating due to the movement of the flux vortices along the grain boundary. As can be seen from Table 9, the effective area of such SQUID is too small to compete with the type (a) SQUID. The coupling to the flux transformer, at the same time, was better compared to the type (c) due to the solid washer.

All SQUIDs (listed in Table 9) demonstrated the absence of $1/f$ noise above 10 Hz. Investigations of the noise properties of the SQUID with flux transformer revealed the same excess $1/f$ noise below 1 kHz for all types of SQUID washers. Fig. 39 demonstrates the comparison of the flux noise spectra of the bare SQUID (green curves) and the SQUID magnetometers (red curves) for SQUIDs type (b) and (c).

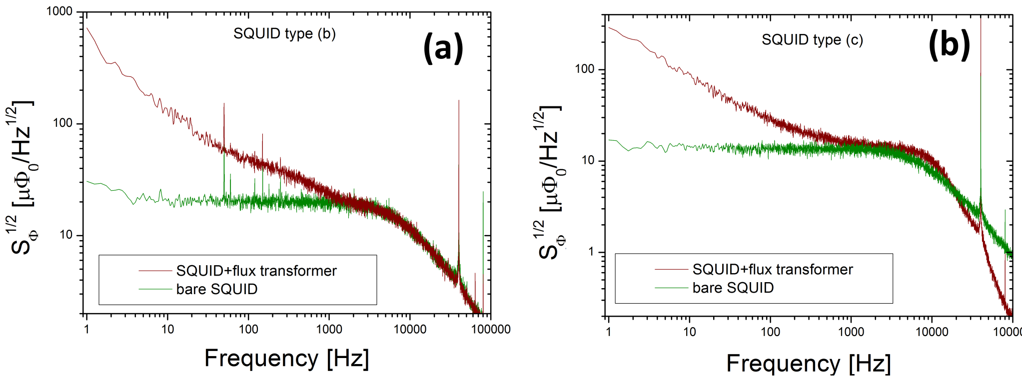

Figure 39: Magnetic flux noise spectra of a bare SQUIDs (green curves) and flip-chip magnetometers (red curves). a)– SQUID type (b), b)–SQUID type (c).

These experiments show that meshes and slots also did not reduce the excess magnetic flux noise. This suggests that the origin of the $1/f$ noise is somewhere in the structure of the flux transformer placed close to the SQUID loop. Thermally activated movement of magnetic flux vortices in the grain boundaries formed in the top YBCO film on the slope of the bottom electrode can be the source of the excess noise. It can be either in the vias or on the slopes of the crossovers. Another possible reason is the motion of the magnetic flux vortices in the defects (e.g. a-oriented outgrowths) in the top YBCO film.

Ferrari *et al.* showed that YBCO films with a-oriented grains have high level of *1/f* noise and it was demonstrated that the magnitude of this noise decreases as the crystalline quality of thin YBCO films is improved [87]. To check the quality of the YBCO films, noise properties of the YBCO films used for the flux transformer fabrication were investigated. To do this, test films were deposited on single crystal STO substrates without bottom YBCO electrode and patterned to the shape of the input coil. Magnetic noise spectra were obtained with SQUID inductively coupled with test films in the same way as it was done for the flux transformer. Fig. 40 shows the magnetic noise spectra of the YBCO film deposited under optimized conditions (blue curve) compared to the film grown at higher temperature that had a-oriented grains (red curve). High quality films did not show any *1/f* noise above 40 Hz, while film with a-oriented outgrowths has very similar *1/f* noise as it was measured in the flux transformer structure. This suggests that the possible origin of *1/f* noise in the flux transformer is either in via or crossover structures or that presence of the bottom electrode results in bad quality of the top YBCO film. To check the latter possibility, detailed investigations of the morphology of the YBCO film of fabricated flux transformers using scanning electron microscopy (SEM) was performed. Fig. 41 shows a SEM image of the central part of the input coil with a via. It can be seen that the quality of the top YBCO film above the interconnection line is different compared with other parts of the input coil. Films above the interconnection line has a-oriented grains, see Fig. 42. Further SEM investigations revealed that the YBCO film of the top electrode in other parts of flux transformers is free from the a-outgrowths.

The presence of a-oriented grains in the top YBCO electrode of the flux transformer above the bottom interconnection electrode can be explained by a local overheating of these areas during the deposition of the top layers. The thermally activated magnetic flux vortices motion between these grains in the top electrode could be the possible source of the *1/f* flux noise detected in fabricated flux transformers because of their proximity to the SQUID.

Test sample was fabricated to check how the small area of the top YBCO film with a-oriented grains can affect the noise properties of the input coil

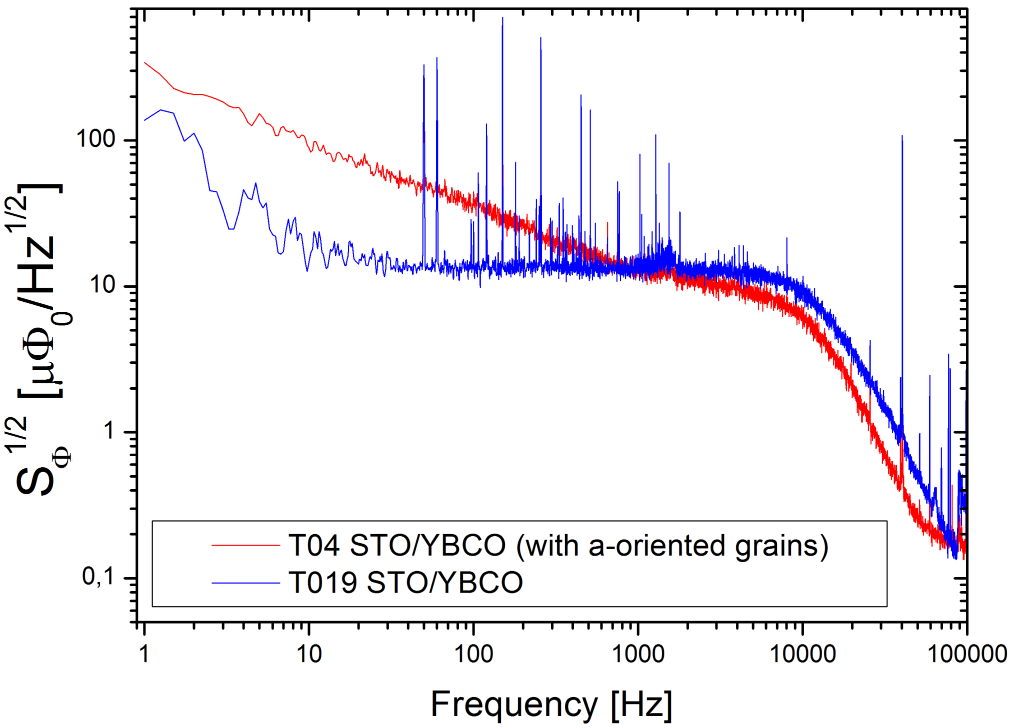

Figure 40: Noise spectra of the YBCO films with (red) and without(blue) *a*-oriented grains.

structure. Two separate input coils were patterned in the top YBCO film deposited on the same substrate. One of the coils was made in a single layer (e.g. top film was deposited on the insulator without interconnection line). Second coil had a multilayer structure (bottom interconnection line - insulator - top spiral input coil). Both coils had no vias to exclude the flux noise produced by vortex motions in grain boundaries on the perimeter of the window in the insulator. We measured the noise spectra of the SQUID when these test coils were aligned with SQUID loop and compared them to the noise spectra of a bare SQUID. In this way we model the input coil with the uniform good film (single layer) and the input coil with areas with *a*-oriented grains (multilayer).

SEM investigations of the test structure revealed that the single layer input coil had no *a*-oriented grains. At the same time the multilayer input coil had areas in the top electrode with *a*-oriented outgrowths (see Fig. 43).

Noise properties of both input coil structures were investigated as described above. Fig. 44 shows magnetic flux noise spectra of the bare SQUID (green curve), SQUID with attached single layer input coil structure (blue),

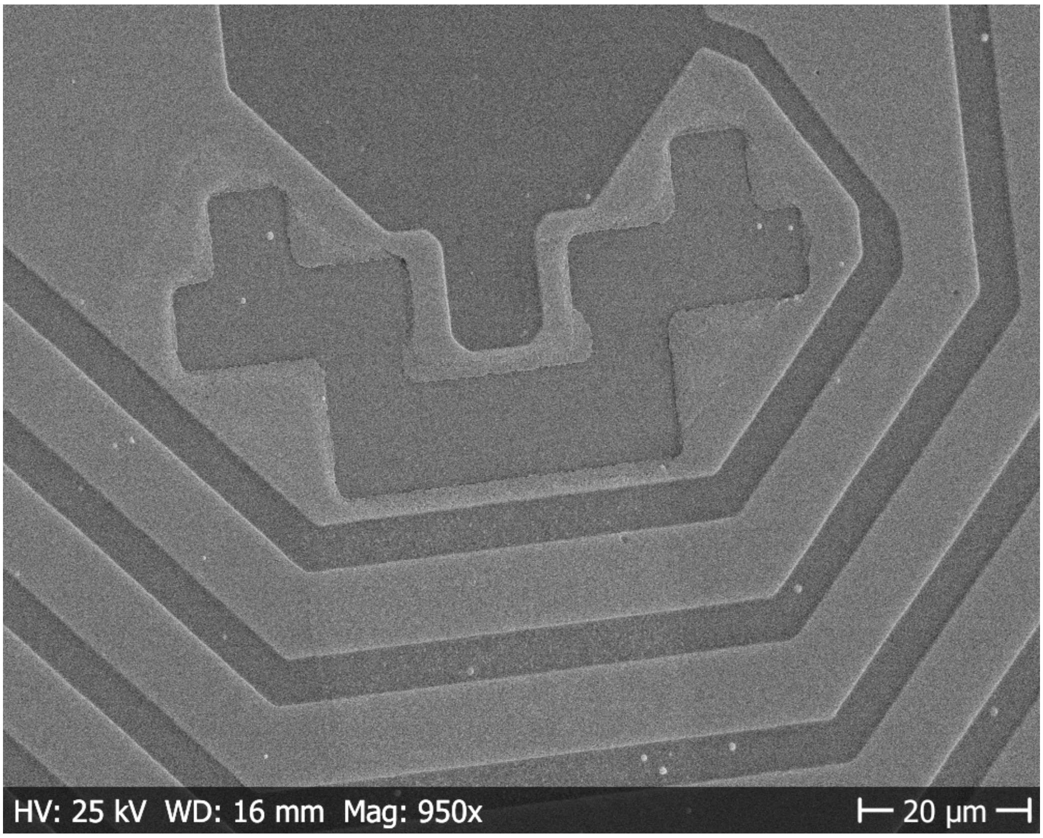

Figure 41: SEM image of the interconnection area of the flux transformer.

and SQUID with attached multilayer input coil structure (red). Obtained noise spectra prove that the areas of top YBCO electrode with *a*-oriented grains could be the possible source of the *1/f* flux noise of the multilayer flux transformers.

At the same time, we cannot exclude a possibility that crossovers also contribute to the flux noise. The top YBCO film on the slopes of the bottom electrode also have defects (as it seen in the Fig. 42), and motion of the magnetic flux vortices in them can be a possible source of the excess noise. However, we assume that crossovers are located at the distance from the SQUID loop above the slot in the washer (see Fig. 33) and their contribution in the detected $1/f$ noise is smaller.

These investigations reveal that the possible source of the excess *1/f* flux noise of developed flux transformers may be due to a presence of *a*-oriented outgrowths in parts of the input coil situated above the bottom YBCO electrode. During the deposition of the top YBCO film, the temperature of the regions above bottom YBCO electrode becomes higher due to more readily

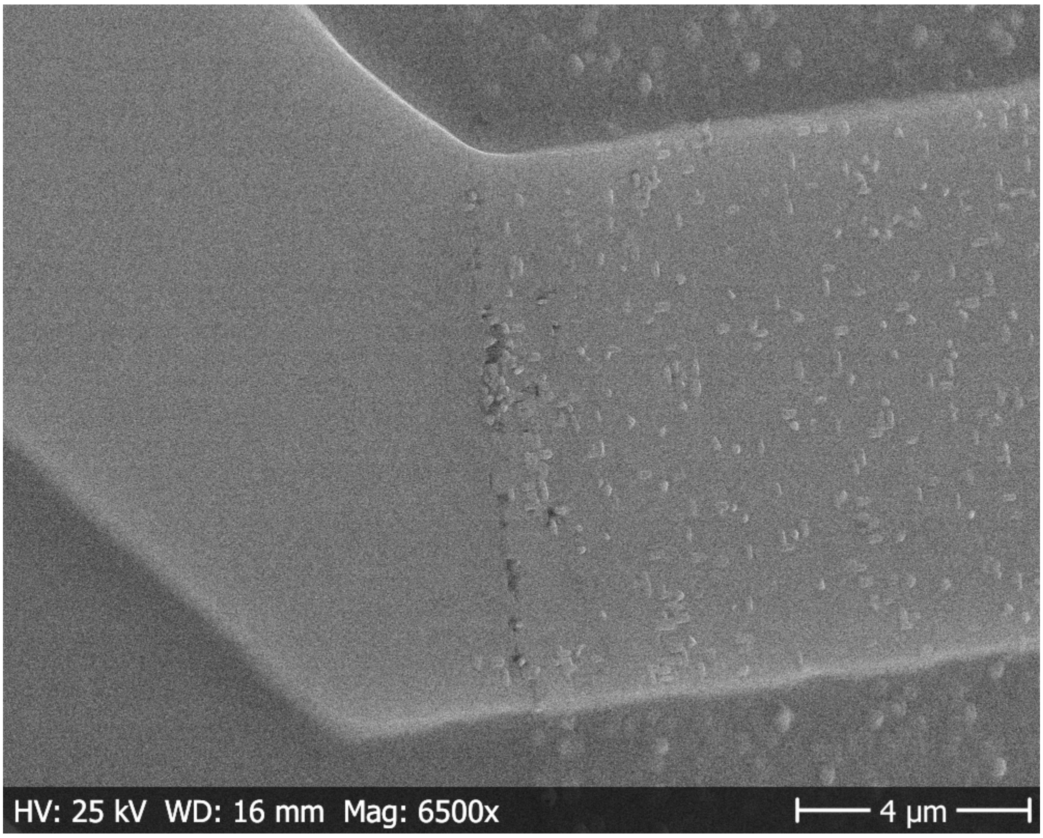

Figure 42: SEM image of the input coil line with the crossover.

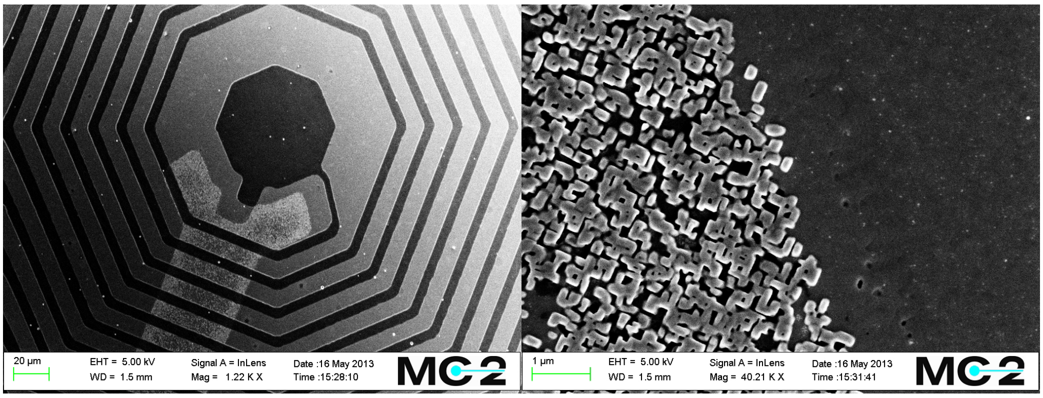

Figure 43: SEM images of the multilayer input coil of the test structure.

absorbing of the infrared radiation from the heater. It leads to the local overheating of the substrate and formation of unwanted outgrowths. This problem can be solved by optimizing the heating method of the sample or

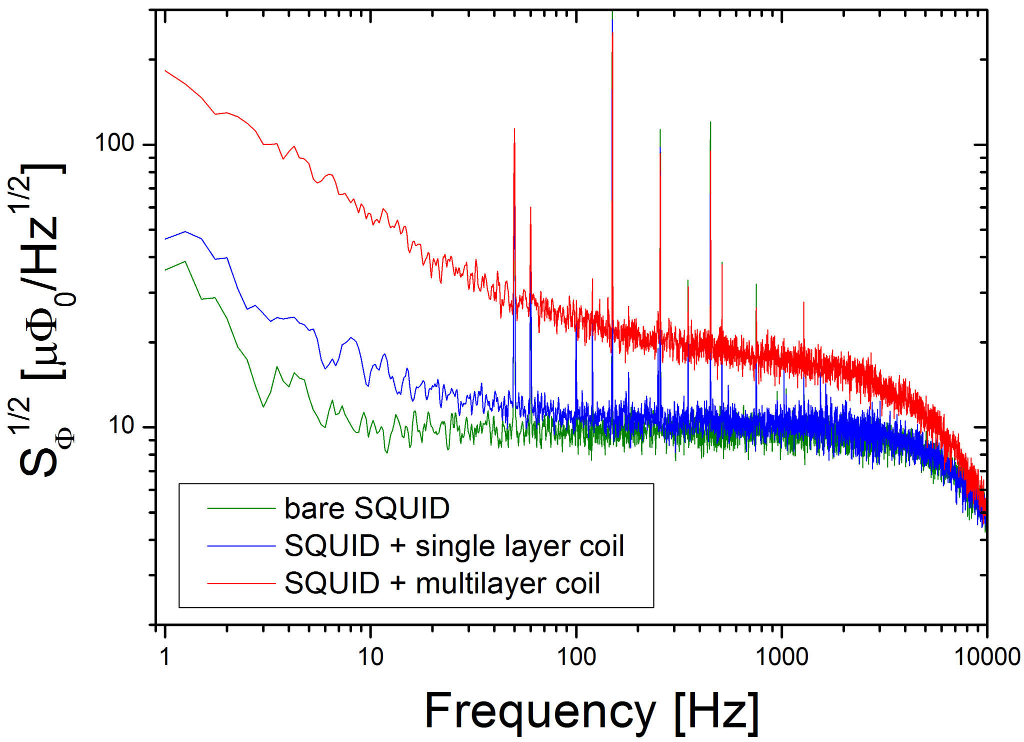

Figure 44: Noise spectra of the bare SQUID (blue curve), SQUID with attached single layer input coil structure (green), and SQUID with attached multilayer input coil structure (red).

by changing deposition parameters of the top electrode. Another possible solution is modification of the layout of the input coil in order to increase the distance between via and SQUID loop by making the inner turn of the coil wider, but this change can decrease coupling.

3.4 Magneto-optical imaging of high-T_c flux transformers.

Fabricated flux transformers were investigated using magneto-optical imaging (MOI) technique [88]. The purpose of this study was investigation of possible sources of $1/f$ noise in the flux transformer. Investigations were done in collaboration with Oslo University using their MOI system. MOI system has the capability of detecting single flux quanta [89] and therefore dynamic measurements could reveal the presence of flux motion in our structures. Detailed description of the MOI system can be found in [90].

The basic principle of MOI is the Faraday effect in a ferrite garnet film

(FGF). Linearly polarized light propagating through the FGF will experience a rotation of its polarization vector if a magnetic field B_{ext} is present parallel to the direction of propagation [90]. The relation between the angle of rotation θ_F and the magnetic field is:

$$\theta_F = B_{ext} \cdot V_F \cdot d_F \tag{17}$$

where V_F is the Verdet constant of the FGF, d_F is the thickness of garnet film. The measured intensity of the light I_F rotated an angle $(\pi/2 - \phi_F)$ and passed through the analyzer is given by the equation [90] (valid for small values of ϕ_F):

$$I_F \approx I_F^0(\phi_F - \theta_F) \tag{18}$$

where I_F^0 is the incoming intensity. Magneto-optical experiments require a polarized light microscope, an optical cryostat, an electromagnetic coil for the generation of the magnetic fields and a recording system (for digital image processing a CCD camera (charge-coupled device) can be used) [88]. The MOI experimental setup used in our investigations is presented in Fig. 45.

To obtain magneto-optical images, the sensor was placed on the surface of the flux transformer. The sensor is a FGF, consisting of a thin film with the chemical composition $(Bi,Lu)_3(Fe,Ga)_5O_{12}$ deposited on a gadolinium gallium garnet substrate. The flux transformer with attached sensor was mounted into the cryostat (Oxford Hi-res). Measurements were done in the temperature range 40–90 K. A magnetic field normal to the surface of the flux transformer was applied using Helmholtz coils in the range 0–8.5 mT.

Fig. 46 presents the magneto-optical images of the input coil of the flux transformer obtained at 67 K for different external magnetic fields. Areas with higher intensity of MOI signal correspond to the higher magnetic in the FGF field compared to the ares with lower intensity. Stronger magnetic field on the edges of the structure is due to the currents flowing in the superconducting film. With increasing external field these areas becomes wider.

Figure 47 presents the zoomed part of the MOI of the input coil. Distribution of the currents in the interconnection areas is of the most interest. As can be seen from the image, current flows through the contour of the vias confirming our assumption that most of the current should flow through the perimeter of via.

During the measurements, the intensity of the MOI signal in the the input coil of the flux transformer was changing during the sweeping of the external field. This behavior is illustrated in the Figures 48, 49, and 50. Fig. 48 demonstrates the MOI of the input coil of the flux transformer taken at 68 K. Frames were taken at different moments of time during slow sweeping of the magnetic field in the range of 0.8–1.6 mT. To analyze the obtained

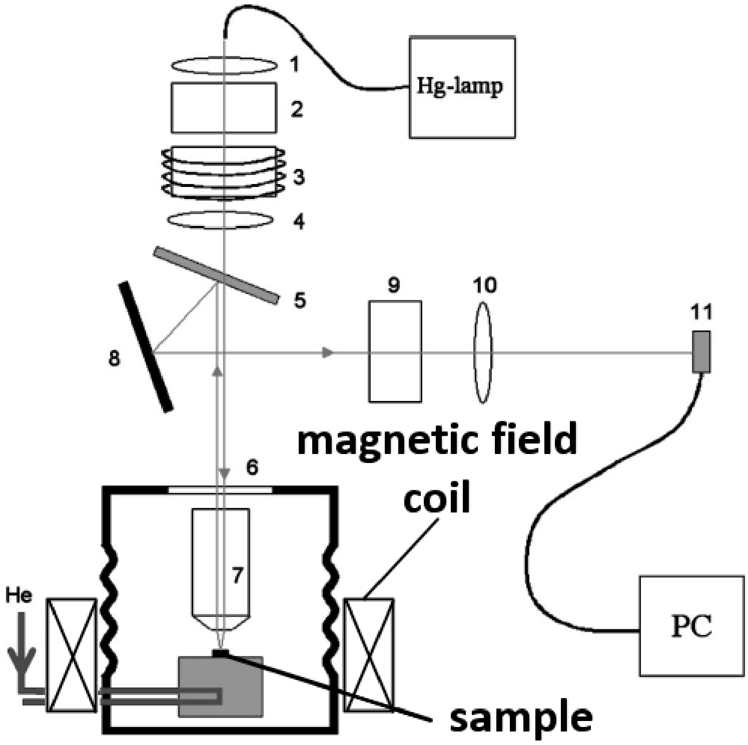

Figure 45: MOI experimental setup. Collimating lens (1), polarizer (2), Faraday rotator (3), focusing lens (4), beamsplitter window (5), vacuum window (6), objective (7), mirror (8), analyzer (9), focusing lens (10), and CCD (11). Figure adopted from [90].

images, small square areas of the images inside and outside of the input coil were selected as presented in Fig. 48.

These areas were processed in MATLAB in order to obtain histograms of images. The y-axis of the histogram gives the number of pixels with certain gradation of gray, the x-axis represents the gradations of gray in the range 0–256, where 0 – black, 256–white. Fig. 49 presents the histograms of areas taken from outside of the input coil. The peak positions on these histograms are the same for all areas indicating that changes in the field is negligible.

MOI and histograms of the areas taken inside of the input coil are presented in Fig. 50. The histograms in this case can be represented by a sum of two peaks corresponding to the bright lines (turns of the input coil) and dark lines (space between turns). It can be seen that peaks for frames (b) and (d) are shifted compared to the frames (a) and (c). This shift indicates increasing of the magnetic field produced by the input coil. This may happen because

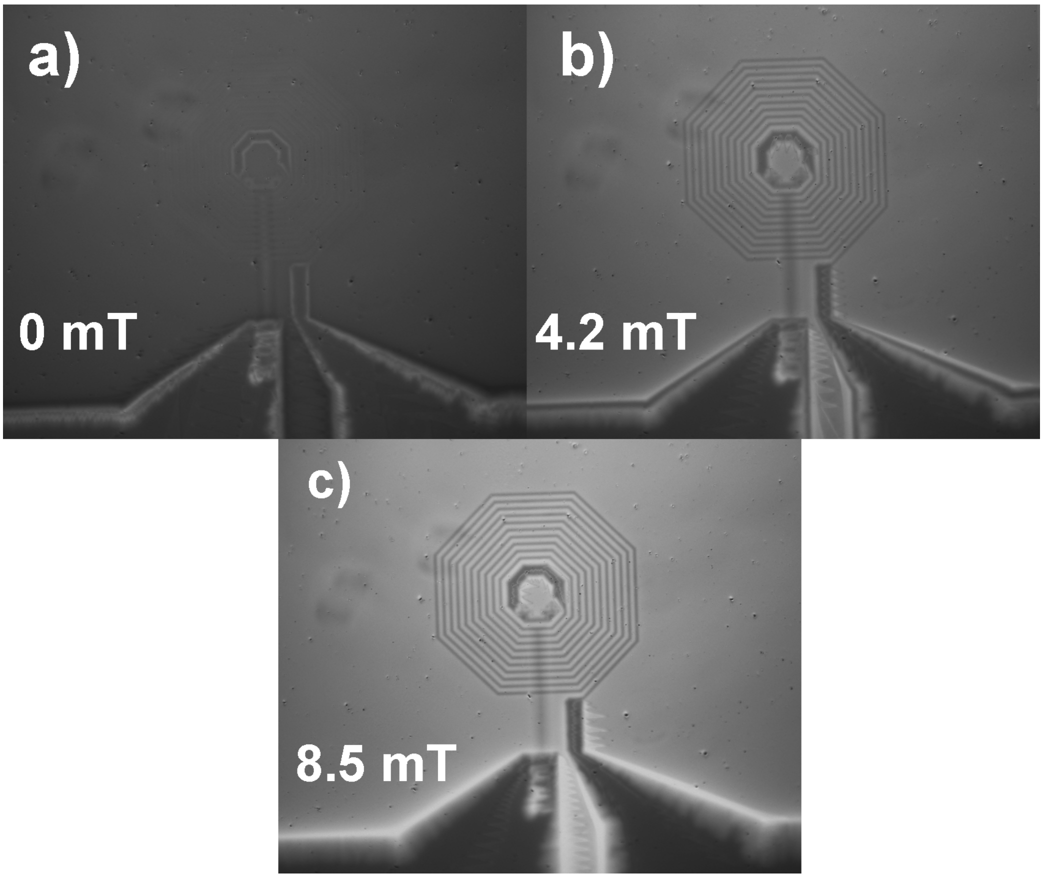

Figure 46: Magneto-optical images of the flux transformer obtained at T=67 K. Frames (a), (b), and (c) correspond to the applied external magnetic fields 0 mT, 4.2 mT, and 8.5 mT.

of the fluctuation of the current in the Helmholtz coils that produces weak fluctuation of the external magnetic field. The FGF is not sensitive enough to detect these fluctuations. At the same time, these weak changes of the magnetic field may be picked up by the flux transformer producing currents flowing in the input coil. These currents generate corresponding magnetic fields above the flux transformer input coil which are detected by FGF.

The assumption that flickering of the magnetic field generated by the flux transformer input coil is attributed to the closed superconducting circuit of the flux transformer is further supported by observation that MOI of the flux transformer with broken pickup loop did not show such behavior. The flickering was still detectable at fields up to 8.5 mT that indicates that upper limit of the operational magnetic fields of our device is at least 8.5 mT or even higher.

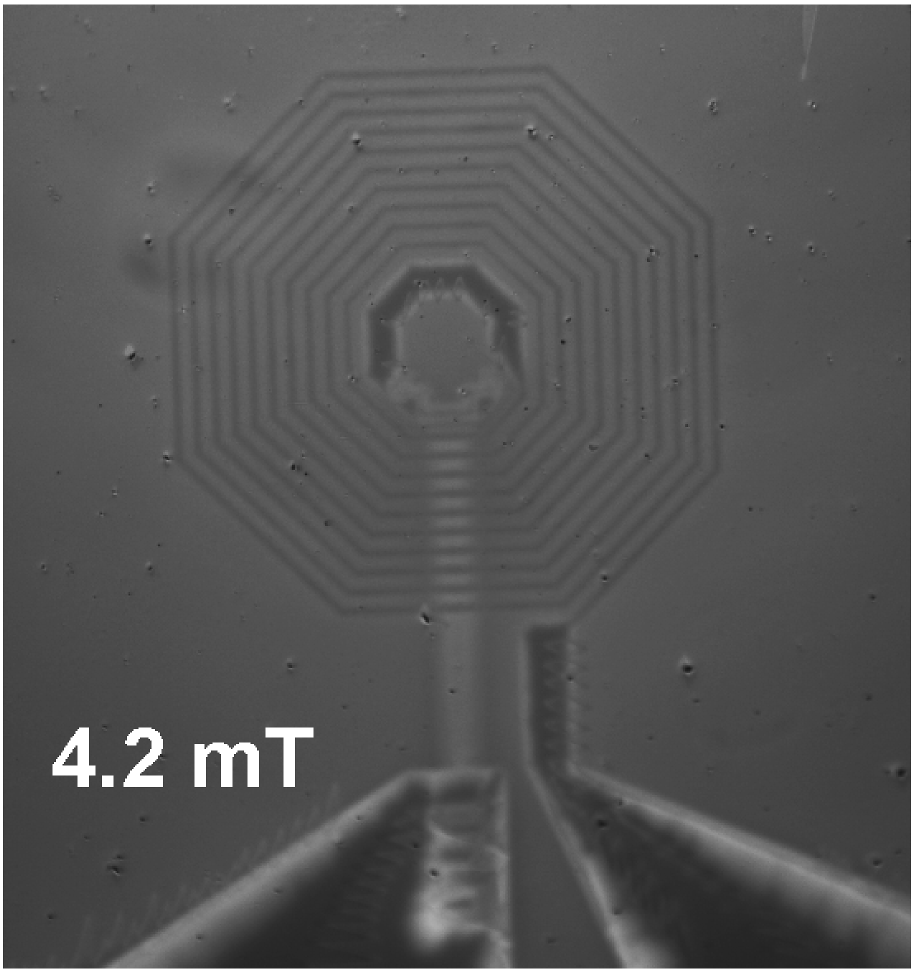

Figure 47: Magneto-optical image of the flux transformer obtained at T=68 K and applied external field of 4.2 mT.

Magneto-optical imaging did not reveal, as we expected, any weak place in the superconducting structure of the fabricated flux transformer. The spatial resolution of the MOI setup used in this particular measurements did not allow us to investigate possible sources of the $1/f$ noise. The resolution was mainly limited by the FGF itself. Detailed investigations of the via areas of the input coil could help localizing the region with the higher levels of flux noise.

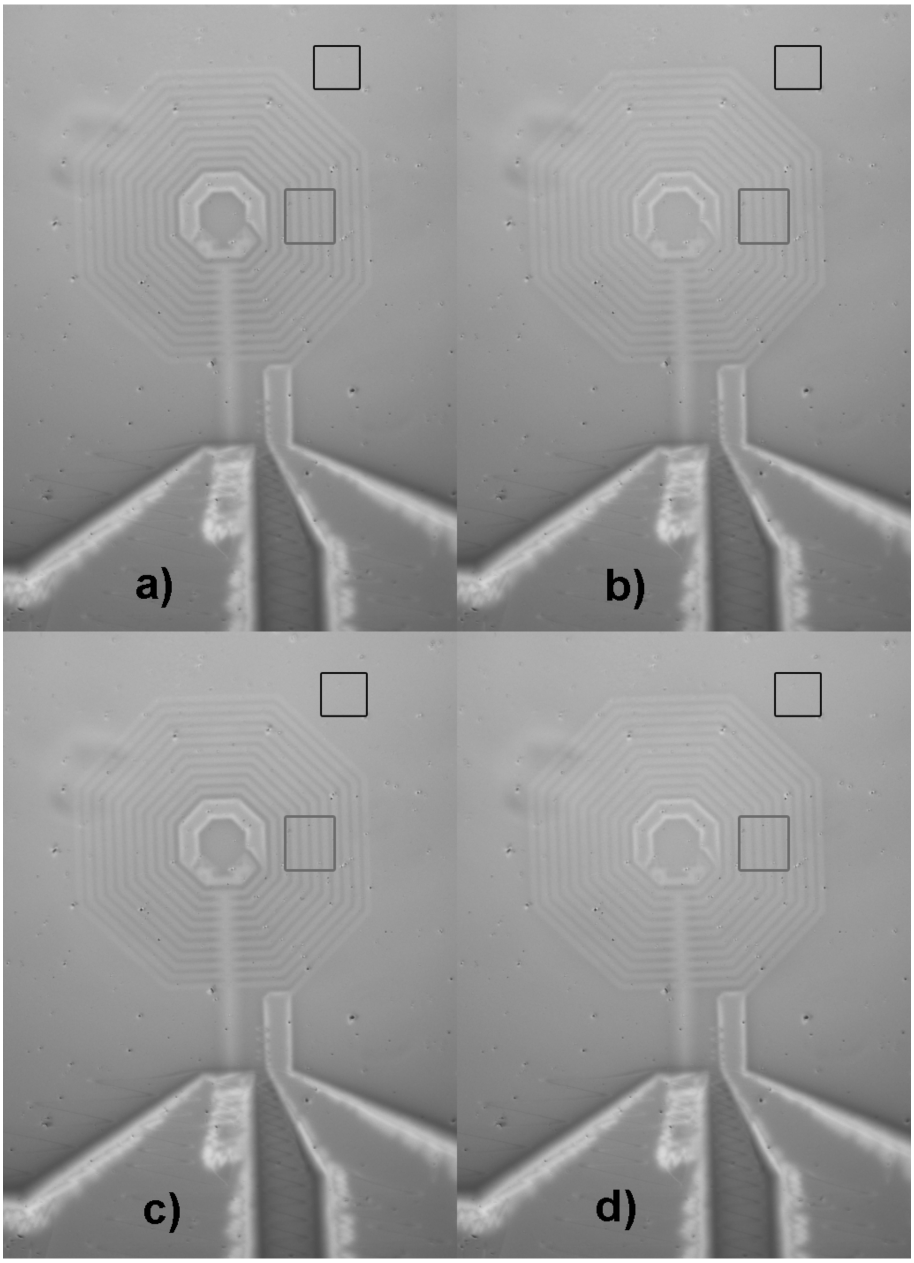

Figure 48: Magneto-optical images of the flux transformer obtained at T=68 K. Squares outside and inside the input coil indicate the position of the analyzed areas.

3.5 Implementation of the flip-chip SQUID magnetometers in ultra-low-field NMR.

Our SQUID magnetometers with superconducting flux transformers were used in an ulf-MRI system. We compared the performance of these sensors

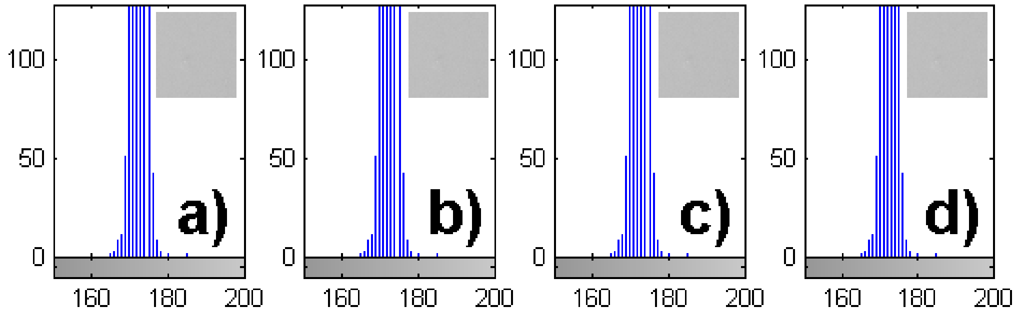

Figure 49: Histograms of the areas placed outside the input coil. Y-axis – counts, x-axis – gradation of gray, where 0 – black, 255 – white.

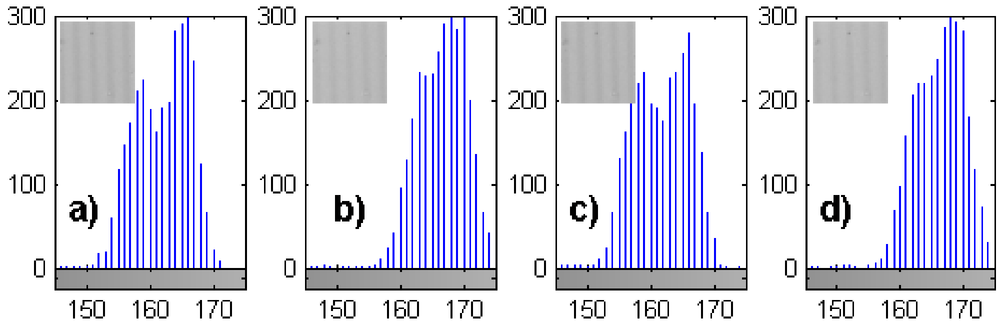

Figure 50: Histogram of the areas placed inside the input coil. Y-axis – counts, x-axis – gradation of gray, where 0 – black, 255 – white.

with that of our planar high-T_c SQUID magnetometers [36].

To evaluate the performance of the ulf-MRI system, we started by doing nuclear magnetic resonance (NMR) spectroscopy at ultra-low field (ulf-NMR). The NMR setup is shown in Fig. 51 and 52. The characteristics of the coils used for the ulf-NMR sensor benchmarking experiments are listed in Table 10. The earth-field cancellation system consisted of 3 orthogonal Helmholtz-like rectangular coils. Each coil was driven by a dc power supply (BK Precision 1745A) and low-pass filtered at 2 Hz. These coils were attached along the inner walls of an RF shielded room that housed the ulf-MR setup. The measurement (B_0) field coil consisted of a large Helmholtz pair (R = 0.8 m) that produced a homogenous measurement field over the sample volume. The current for the measurement coil was supplied by dc power source (HP 6030A) and low-pass filtered at 1 Hz. A 1600-turn solenoid coil produced the prepolarization (B_P) field.

In order to protect the SQUID sensor during the MR pulse sequences, we constructed a copper flux transformer that inductively coupled the MR

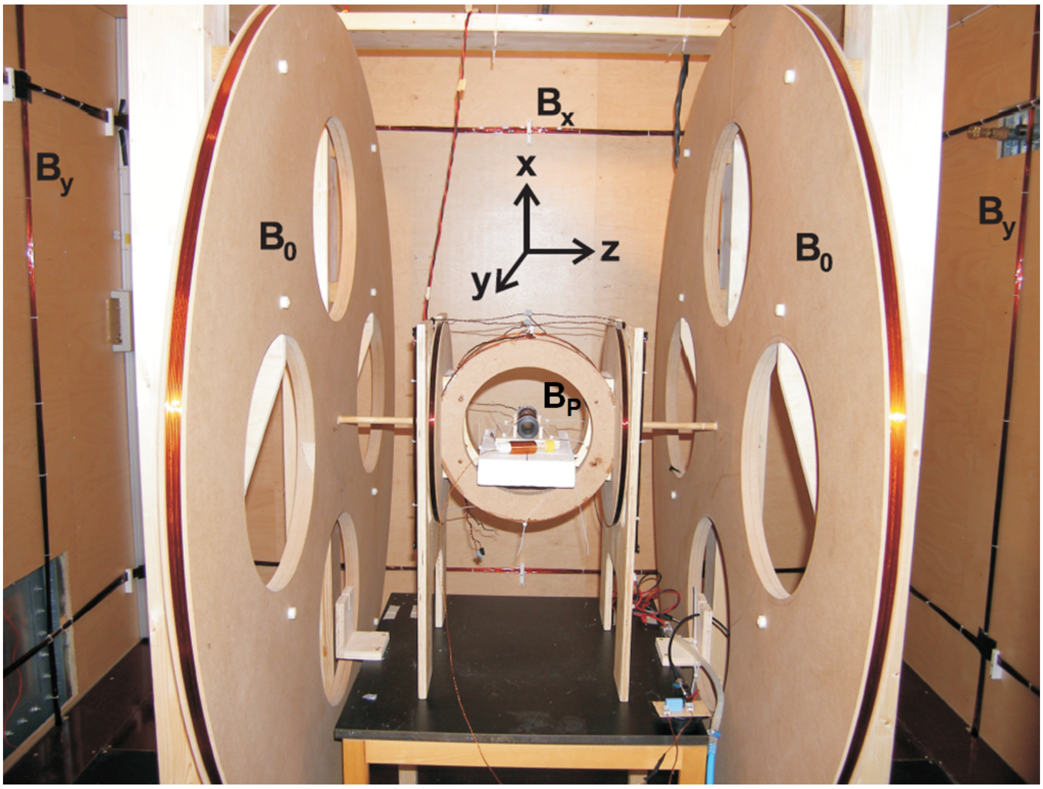

Figure 51: Photograph showing the NMR setup.

sample to the sensor [91]. The transformer had a 400-turn sensing coil (diameter 0.5 mm copper wire) that fit inside the B_P solenoid. The coil had an inner diameter of 22 mm and a length of 60 mm. The sensing coil was connected in series to a 200-turn coupling coil (diameter 0.15 mm copper wire). The total inductance of the copper flux transformer was 1 mH that, when connected to a 1.47 μF capacitor, had a resonance frequency of 4150 Hz. A computer-controlled switch circuit was used to disconnect the transformer line from the coupling coil during the prepolarization pulse. A 10-ml water sample was placed inside the sensing coil as shown in Fig. 52.

We employed a simple free-induction decay (FID) ulf-MRI pulse sequence for comparing the SNR of the planar and flip-chip SQUID magnetometers. After switch-off of the prepolarization pulse, the excess magnetization of the protons-in-water remains aligned in the x-y plane as it precesses around the axis of the measurement (B_0) field (z-direction) for a time T_1 [43]. The SNR of this FID signal is the benchmark figure of merit for comparison of our sensors.

Fig. 53 (a) presents a single-shot water NMR peak obtained with a pla-

Table 10: Ulf-MR system coil characteristics.

Coil description	Field	Dimensions	Number of turns	Inductance	Field strength
Cancellation coil x-axis	B_{CX}	2.93 m×2.93 m	20	10 mH	10 μT/A
Cancellation coil y-axis	B_{CY}	2.93 m×2.37 m	20	10 mH	10 μT/A
Cancellation coil z-axis	B_{CZ}	2.93 m×2.37 m	20	10 mH	10 μT/A
Measurement coil	B_0	$R = 0.8$ m	100	80 mH	120 μT/A
Prepolarization coil	B_P	Inner $R = 0.012$ m Outer $R = 0.036$ m Height $h = 0.078$ m	1600	30 mH	20 mT/A

nar SQUID sensor under optimized system parameters. The peak yielded an SNR of 90 and was obtained with a measurement (B_0) field of 90 μT and a prepolarization pulse of 50 mT. As a proof-of-principle demonstration, we performed direct benchmarking in which the flip-chip SQUID magnetometer was compared to a planar one. This experiment was performed with a measurement field of 102 μT and prepolarization pulse of 18 mT. We present the average of 50 NMR peaks obtained under these experimental conditions with both the flip-chip and planar SQUID sensors in Fig. 53 (b).

The overall SNRs in the benchmarking experiment presented in Fig. 53(b) were lower than that of Fig. 53 (a) for several reasons. First and foremost, the prepolarization pulse was lower in magnitude because the prepolarization coil was modified for the benchmarking experiments. Furthermore, low-frequency magnetic-field fluctuations affected the NMR frequency over the course of 10s of seconds. We therefore did not use single-shot recordings for the benchmarking because, for example, it is difficult to be certain the fluctuations in the magnetic field would be the same for the two conditions under such a short time window ($\approx$ 5 s per "shot"). Only by averaging many periods of the fluctuating field ($\approx$ 5 mins total measurement time) can we ensure the fluctuations are averaged out in the same way for both sensor technologies. Each individual shot was then adjusted in frequency (i.e. field) to form an overlay of spectra to obtain a more noise free averaged spectrum. Nevertheless, the measurements demonstrate a more than 2-fold improvement in the SNR for the flip-chip sensor.

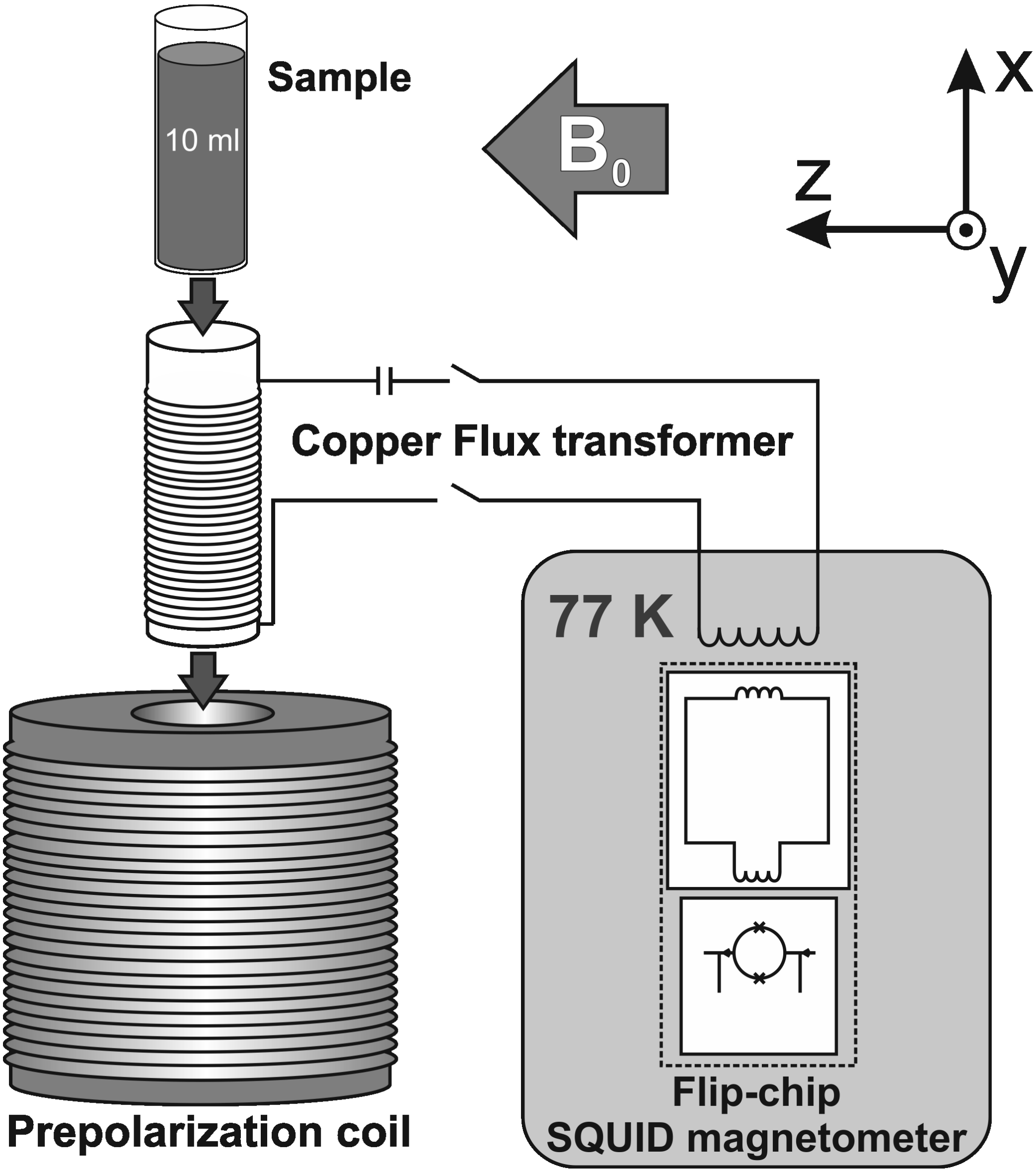

Figure 52: NMR setup.

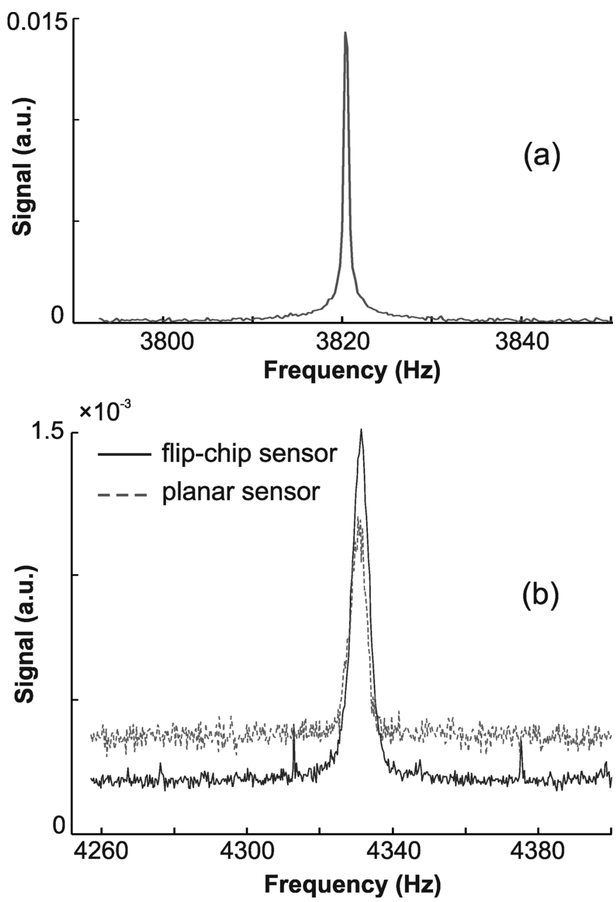

Figure 53: (a) A single-shot NMR peak of tap water obtained with a single-layer SQUID sensor. B_0 was 90 μT and B_P was 50 mT. (b) Average of 50 NMR peaks directly comparing the SNR of our flip-chip (solid) and planar (dotted line) SQUID magnetometers (B_0 = 102 μT, B_P = 18 mT).

4 Superconducting Quantum Interference Filters

4.1 Principles of SQIF operation

A dc SQUID is a magnetic flux-to-voltage transducer. The response of the SQUID to the magnetic flux is periodic and therefore SQUID can measure only the variation of the magnetic flux and not its absolute value (see Fig. 54 (a)). It turns out that if many dc SQUIDs with randomly distributed loop sizes are connected in a parallel or in a serial array its flux-to-voltage response function $V-\Phi$ becomes non-periodic. Such an array is called superconducting quantum interference filter (SQIF). A full theoretical description of the SQIF function is complicated and can be found in [92]. Briefly, the average voltage $\overline{V}$ across the SQIF (for an array consisting of $N/2$ SQUIDs) is:

$$\overline{V} = I_c R \sqrt{J_N^2 - |S_N(\mathbf{B})|^2} \tag{19}$$

where $I_c = \frac{1}{N}\sum\limits_{n=1}^{N} I_{c,n}$, $R = \frac{1}{N}\sum\limits_{n=1}^{N} R_n$ ($I_{c,n}$ and R_n – critical current and normal resistance of n-s Josephson junction), $J_N^2 = \frac{I}{NI_c}$, and $|S_N(\mathbf{B})|$ is a structure factor for the Josephson junction array. The structure factor is an extremely responsive function of strength and orientation of the magnetic field $\mathbf{B}$, and it is strongly affected by the choice of the individual area elements $\mathbf{a}_m$:

$$S_N(\mathbf{B}) = \frac{1}{N}\sum_{n=1}^{N}\frac{I_{c,n}}{I_c} exp\left|\frac{2\pi i}{\Phi_0}\sum_{m=0}^{n-1}\langle\mathbf{B},\mathbf{a}_m\rangle\right| \tag{20}$$

Theoretical calculation shows that if the areas a_n of different loops are chosen in such a way that for a finite external magnetic field $B^{(1)}$ a coherent superposition of the array junction currents is prevented, the voltage response function $\overline{V}$ vs. $|\mathbf{B}_{ext}|$ becomes nonperiodic. From the analogy to optical interference pattern such configuration was called unconventional grating structure [92].

To prevent the coherent superposition of the array junction currents for a finite external magnetic field $\mathbf{B}_{ext}$, a distribution of the array loop sizes should have two properties. First, there is no existing greatest common divisor for the loop sizes. Second, the loop sizes are distributed between their maximum and minimum values in such way that no distinct loop size is preferred and the smallest loop size strongly differs from the size of the largest [92]. When these conditions are fulfilled, the voltage response of the SQIF as a function of the external magnetic field demonstrates a dip in at the zero $\mathbf{B}_{ext}$ (see Fig. 54 (b)).

Such an array can be used as an absolute detector of magnetic flux (or magnetic field) [93]. Another advantage of the SQIF is that the slope of the $V - \Phi$ transfer function is much higher as compared with a single dc SQUID of the equivalent area. This increases the linearity and dynamic range of the sensor. On the other hand, standard FLL readout scheme traditionally used for the dc SQUIDs can not be applied to the SQIF. New readout configuration should be developed to operate the SQIF sensors.

Theoretical calculations also show that the response of the SQIF is not very sensitive to the spread of parameters of Josephson junctions in individual loops. This is advantageous for high-T_c superconductors since the reproducibility of high-T_c Josephson junctions is relatively low (10-20 % at the best, and typically about 50 % depending on junction type used in the fabrication technology).

SQIFs were realized in high-T_c superconductors in 2003 for the first time [94, 95]. In this work, the fabricated arrays consisted of 30 SQUID loops with different loop sizes. Two basic SQIF types (serial and parallel connection of SQUIDs) as well as parallel-serial/serial-parallel combinations were tested. It was shown that for serial SQIFs the transfer function V_ϕ increases with increasing of a peak voltage (the height of the dip at the $\mathbf{B}_{ext} = 0$) as expected and noise decreases. The parallel (and parallel-serial) SQIF did not reach their full potential with respect to the transfer function V_ϕ when compared to the serial SQIF [94]. The possible reason for this is the self-field of the bias current which is flowing in many parallel paths through the SQIF. Therefore, the outer loops observe a different magnetic field than the inner ones.

A possibility of using high-T_c SQIFs as magnetometers was also investigated [95, 96]. SQIFs were connected to the pickup loops and SQIFs-based magnetometers were tested. The best magnetic field sensitivity of 70 fT/Hz$^{1/2}$ was achieved with a multilayer flip-chip pickup loop [95]. These experiments demonstrated the possible potential of using SQIFs as an absolute magnetic field sensor. On the other hand, it was shown that high-T_c SQIFs still suffer from a spread in the Josephson junction parameters. The spread in critical currents of junctions in the array can lead to the decreased number of SQUIDs which operate at certain bias current. Nevertheless, preliminary results show that serial SQIF arrays can be realized on bicrystal Josephson junctions.

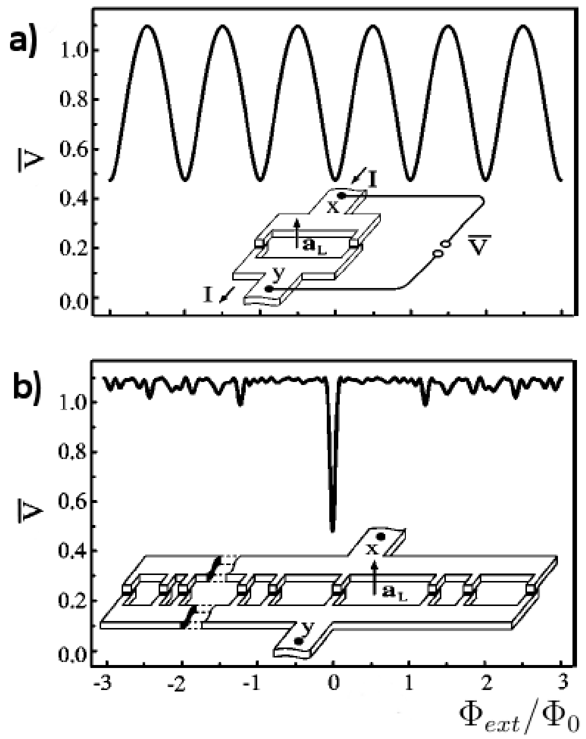

Figure 54: Voltage response $\overline{V}$ in units of I_cR_n as a function of external magnetic flux Φ_{ext} through largest area element a_L of the interferometer with N junctions for bias current $I = 1.1NI_c$: a) – symmetrical SQUID ($N = 2$), b) – array with the SQUID loop areas randomly distributed between 0.1 and 1.0 a_L ($N = 18$). Figure adopted from [92].

4.2 Design and fabrication of high-T_c SQIFs

We have developed the design of the serial array of dc SQUIDs on bicrystal substrate. Even if a serial array is more sensitive to variation of individual junction parameters, it was chosen because the normal resistance of the parallel array will be very low ($\approx R_n/N$, where R_n - normal resistance of a single SQUID, N – number of SQUIDs in the array). Very low normal resistance will be difficult to match to the high impedance of the preamplifier in the readout electronics. Another goal of this project was to extend the operational frequency to the gigahertz range and use the SQIF as a microwave amplifier. For this reason the impedance of the SQIF should also match 50 Ω impedance of a microwave line.

The layout of the developed SQIF is presented in Fig. 55. The SQIF structures consisted of the 50 SQUIDs with randomly distributed inductances

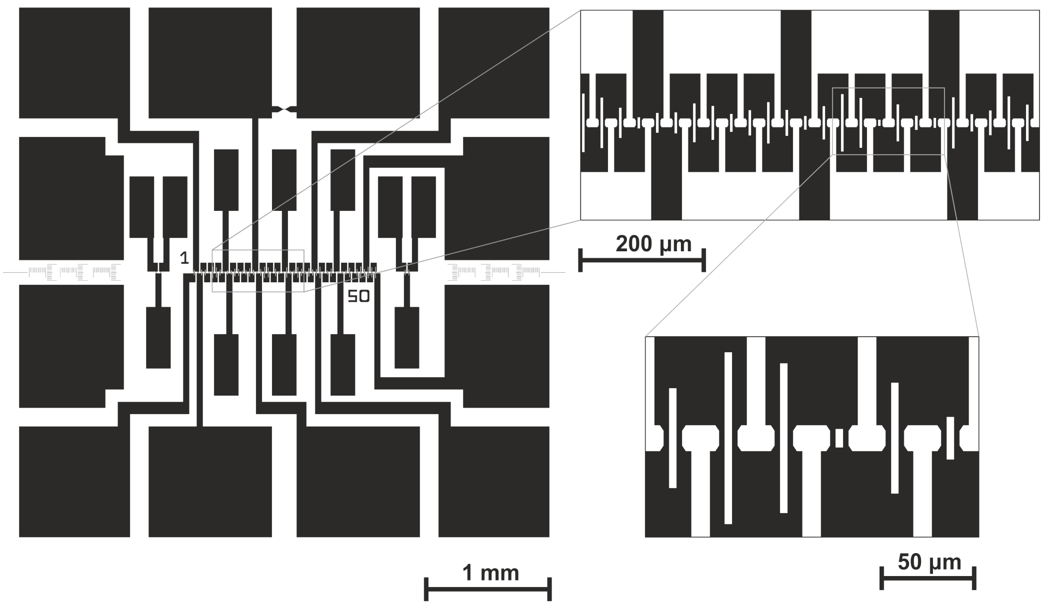

Figure 55: Layout of the contact mask for the SQIF fabrication (only one structure with SQIF chip is shown for clarity).

(in the range of 15–150 pH). The length of the SQIF array is 1.5 mm. The inductances of each individual SQUID were chosen using a random number generator. To compare non-periodic and periodic serial arrays of SQUIDs, a regular SQUID array consisting of 50 SQUIDs with equal inductances of L_S=50 pH was also designed. In this design we also preserved a possibility to access individually segments of the SQIF structure.

Calculated flux-to-voltage transfer functions of the designed SQIF structure and the single SQUID using Eq. 19 and 20 are presented in Fig. 56. The voltage response is normalized to the value of a single SQUID modulation depth. The SQUID has loop size that corresponds to the average area of the SQIF. In these calculations influence of the neighboring inductances of the SQUID loops was taken in to account that led to a reduction of the voltage peak height.

Four SQIFs and one regular SQUID array were fabricated on 24° YSZ and STO bicrystal substrates. 220–300 nm thick YBCO films with 30 nm thick CeO_2 buffer layers were deposited using PLD. The structures were patterned as described in section 2.2. The Josephson junction width was 3 μm for all samples.

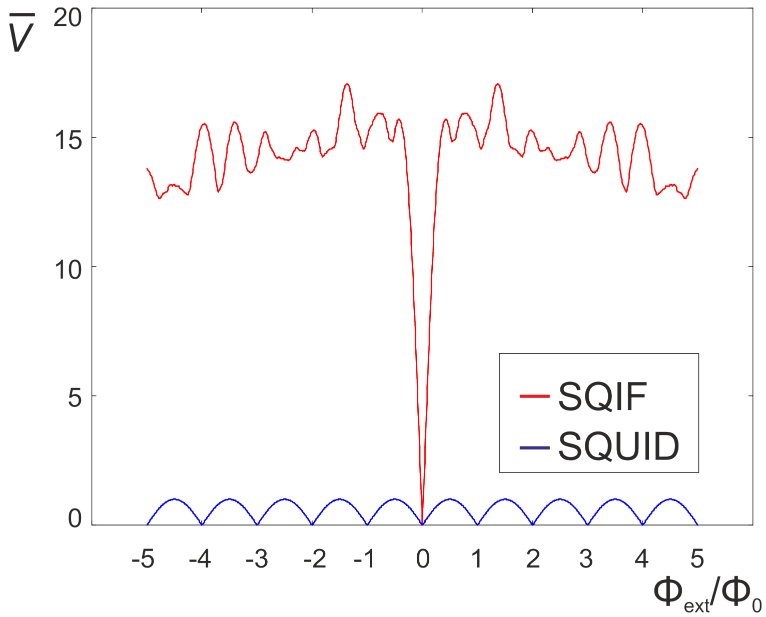

Figure 56: Calculated voltage response of the SQIF (red) and single SQUID with average area (blue) as a function of applied external flux. Voltage response normalized to a modulation depth of a single SQUID with area corresponding to the average SQUID area of the SQIF.

4.3 Electrical characterization

Electrical characterization of the fabricated SQIFs was performed in the temperature range 4-300 K. Fig. 57 shows a typical resistance vs. temperature curve of one of the SQIFs. There is a sharp transition at 90 K corresponding to the T_c of the YBCO thin film electrodes and residual tail down to approximately 77 K. This broadening of the resistance vs. temperature curves of the GBJs can be described by thermally activated phase slippage (TAPS) [97]. The experimental study of TAPS in YBCO grain boundary Josephson junctions can be found in [98].

$I-V$ curves and voltage-to-field responses were obtained in the temperature range 4–77 K. The voltage responses were measured using external normal metal coil. Typical $I-V$ characteristic of the SQIF obtained at T = 7 K is presented in the Fig. 58 (a). It can be seen that the $I-V$ curve has a set of steps corresponding to critical currents of the individual SQUIDs. Maximum and minimum critical currents of the array can be evaluated from the dependence of dV/dI as a function of current (see Fig. 58 (b)). At a higher temperature, the $I-V$ characteristics of the SQIF become more round due to thermal fluctuations of the critical currents (see Fig. 59). All

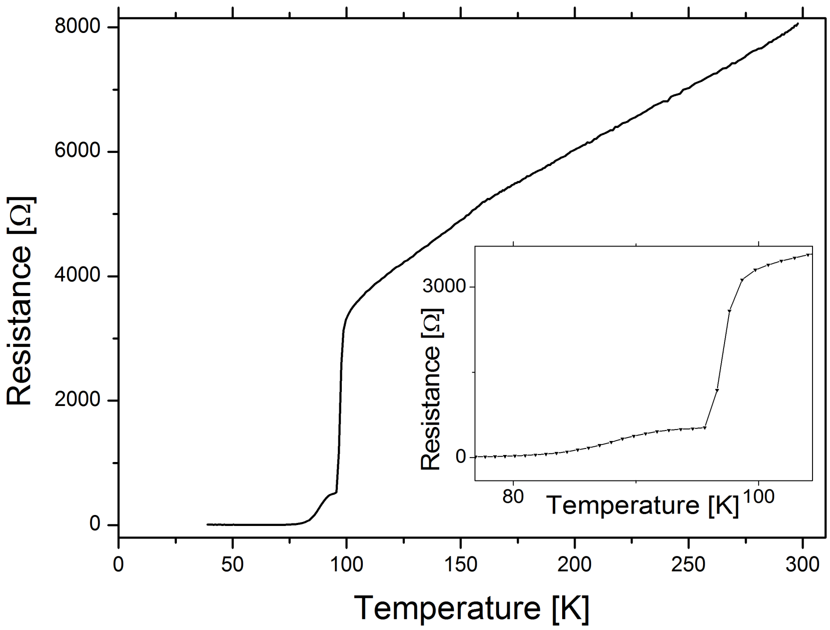

Figure 57: Temperature dependence of SQIF resistance.

samples fabricated on YSZ substrates (SQIF01, 02, 04 and SQUID array) demonstrated similar spread in the parameters as it is shown in Table 11.

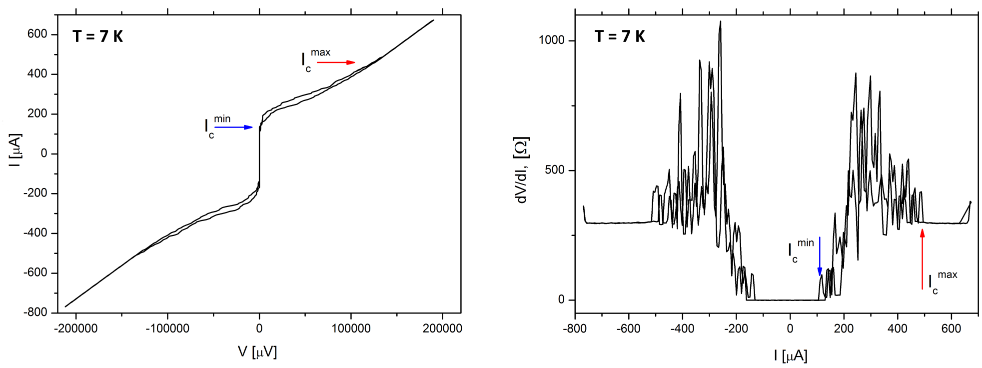

Figure 58: Typical SQIF I-V characteristic (a) and dV/dI as a function of I (b) at T = 7 K.

Observed spread of the critical currents means that when a certain bias current is applied to the array, not all of the SQUIDs are operated together.

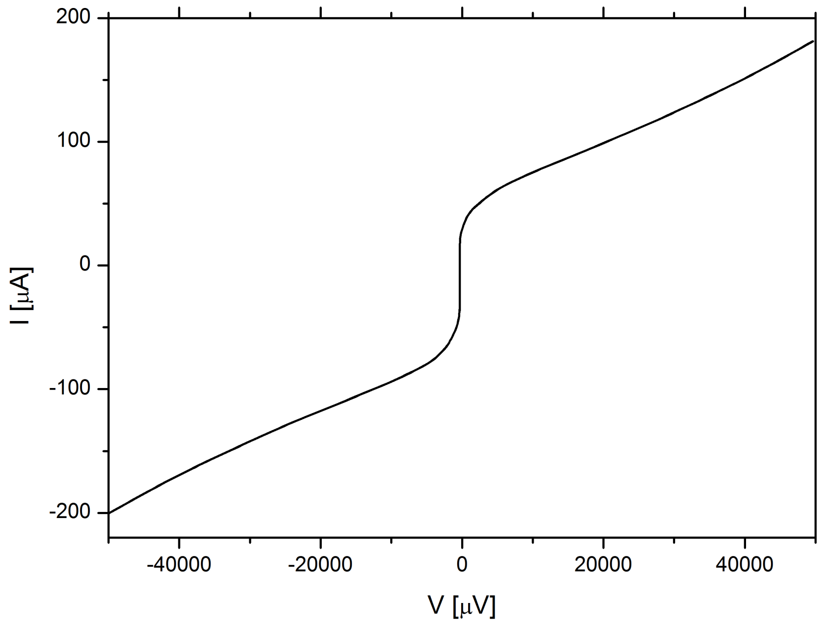

Figure 59: *I-V* characteristic of the serial SQIF array of 50 loops fabricated on the YSZ bicrystal substrate at T = 60 K.

This is illustrated in Fig. 60 that shows the voltage-to-field responses of SQIF04 obtained at T = 65 K (x-axis indicates the current applied to the coil). The nonperiodic voltage response seen in Fig. 60 (a) corresponds to a bias point where only a few SQUIDs are operational. Fig. 60 (b) illustrates the situation when only one SQUID is biased.

Electrical characterization of the SQIFs on YSZ bicrystal substrates revealed a large spread in the parameters of individual Josephson junctions along the grain boundary. Due to the spread of critical currents, not all of the 50 SQUIDs operated at chosen bias point which led to the absence of the voltage dip at zero applied field (see Fig. 60). Electrical characterization of individual SQUIDs in the array (for the sample SQIF02) is presented in Table 12.

The possible reason of the Josephson junction parameter spread is the variation of the grain boundary quality in the bicrystal substrate. When the YBCO film grows over the bicrystal border, some "dead" superconducting layer may appear in the beginning of the growth. The thickness of the dead layer depends on the local quality of grain boundary that results in variation of junctions parameters.

Table 11: Characteristics of SQIFs obtained at 7 K.

Sample ID	Film thickness, nm	I_c^{min}, μ A	I_c^{max}, μ A	R_n^{max}, Ohm
SQIF01	220	75	280	550
SQIF02	220	68	300	480
SQUID array	300	170	500	280
SQIF04	300	140	480	300
SQIF05	250	180	350	100

Table 12: Measured parameters of individual SQUIDs in the serial array of 50 loops sample SQIF02.

SQUID ID	I_c, μA	R_n, Ohm	$I_c R_n$, mV
SQD	230	8	1.8
SQ01	190	8	1.5
SQ02	200	7	1.4
SQ10	175	11	1.9
SQ18	260	8	2
SQ26	200	7	1.4
SQ34	250	7	1.8
SQ40	370	5	1.9

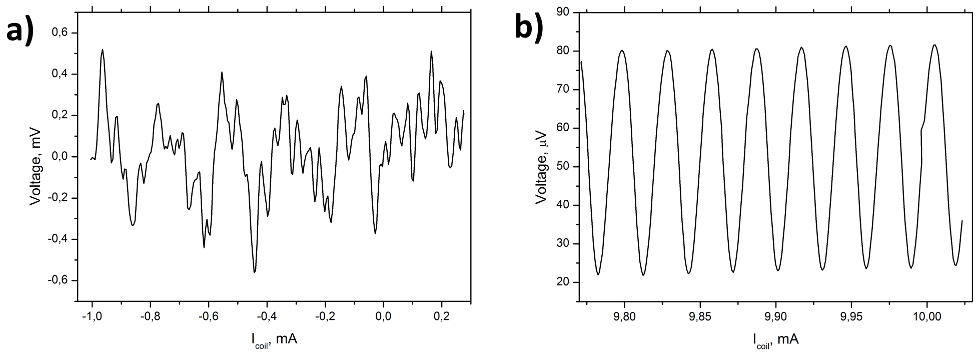

Figure 60: Voltage-to-field responses of the SQIF04 serial array measured at T=65 K at different bias currents. a) – a bias point where only few SQUIDs are operational, b) – only one SQUID is biased.

Table 13: Measured parameters of individual SQUIDs of the sample SQUIF05 fabricated on the STO bicrystal substrate.

SQUID ID	I_c, μA	R_n,, Ohm	I_cR_n, mV
SQD	240	7	1.7
SQ01	320	4.3	1.4
SQ02	230	4.4	1
SQ10	350	4.2	1,5
SQ18	330	4.2	1.4
SQ26	320	4.4	1.4
SQ34	280	5	1.4
SQ40	190	6.8	1.3

One of the SQIFs was fabricated on an STO bicrystal substrate (sample SQIF05 in the Table 11). Parameters of the individual SQUIDs of this SQIF obtained at 7 K are presented in Table 13.

The spread of critical currents is smaller on this sample possibly due to the more uniform film quality along the grain boundary. The voltage-to-field responses of this SQIF at different magnetic field ranges obtained at 77 K are presented in Fig. 61. Decreased spread of junction parameters resulted in the appearance of the voltage dip at zero applied magnetic field. Nevertheless, the depth of this dip is still small (approximately 1.5 times larger than the "roughness" of the other parts of the voltage-to-field characteristic) that indicates that the number of operational SQUIDs is still small.

To estimate the number of operational SQUIDs in the array calculations

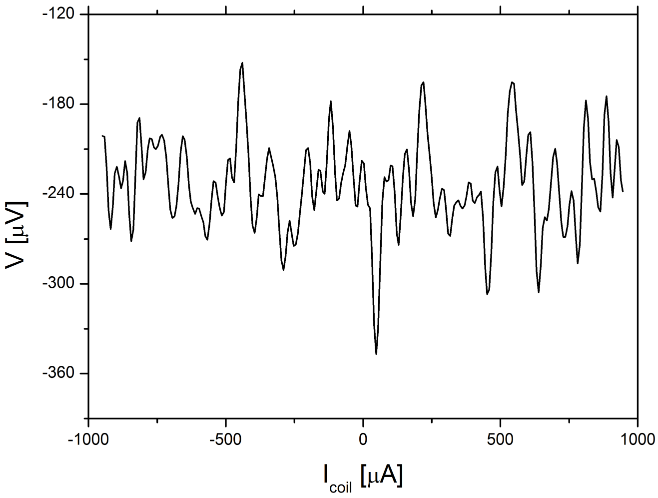

Figure 61: Voltage-to-field response of the SQIF serial array fabricated on an STO bicrystal substrate (sample SQIF05) obtained at T = 77 K.

using Eq. 19 and 20 were performed. Fig. 62 presents calculated voltage response as a function of the external magnetic flux for an aperiodic array of 5 SQUIDs. Calculated voltage response demonstrates similar ratio between the zero field dip depth and "roughness" of the other parts of the voltage-to-field characteristic. It indicates that even in case of relatively small spread of junction parameters the number of operational SQUIDs of the array is around 10%. This means that for a practical use the number of SQUIDs in the high-T_c SQIF should be increased. For a 5×5 mm^2 substrate the number of SQUIDs can be increased by approximately three times (length of the array is 1.5 mm). The number of SQUIDs can be increased up to 300 using 10×10 mm^2 substrates, but in this case the total length of the array will be 9 mm. This means that a gradient in the magnetic field will affect such magnetometer. Another important issue is the thermal noise of the SQIF that increases with the increasing normal resistance of the SQUID array.

One of the tested samples was a regular array of SQUIDs (sample SQUID array in Table 11). It demonstrates similar spread of parameters but has periodic response with the peak-to-peak amplitude close to 800 μV at T = 55 K (see Fig. 63). The transfer function V_Φ of such array is much higher as compared with the single SQUID. Regular SQUID arrays may be promising in the magnetometer configuration. The periodic response means that standard FLL electronics can be used to operate such a SQUID array. At the same time the normal resistance of such array is 280 Ω that is much

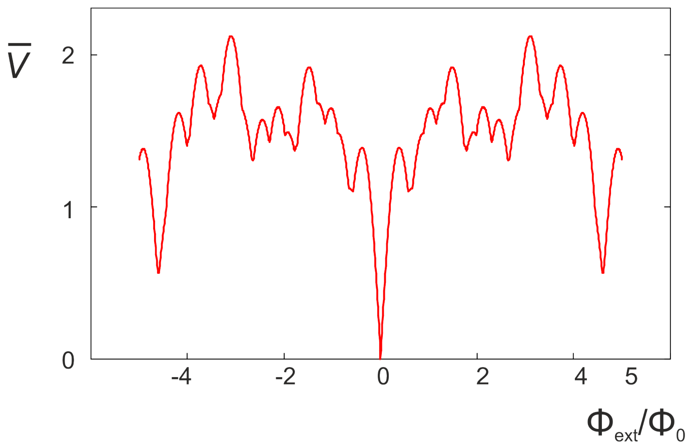

Figure 62: Calculated voltage response of the serial SQIF consisting of the 5 SQUIDs as a function of external magnetic flux. Voltage response normalized to a modulation depth of a single SQUID with area corresponding to the average SQUID area of the SQIF.

higher compared to the single SQUID and that will increase the white noise level of the possible SQUID array-based magnetometer.

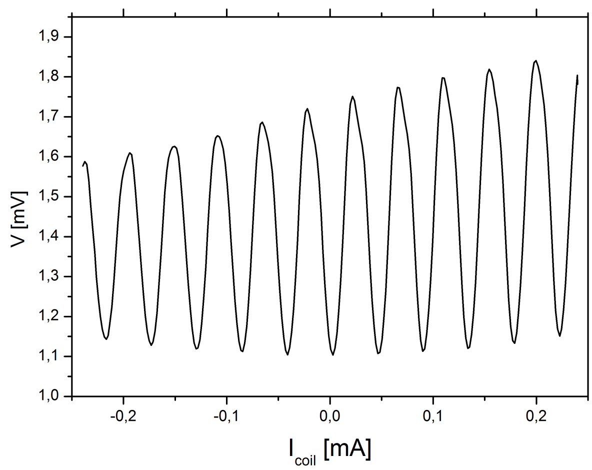

Figure 63: Magnetic responses of the serial array of SQUIDs with equal inductances measured at T = 55 K.

4.4 Summary

In conclusion, we have realized practical SQIF arrays of 50 individual random SQUID loops on a bicrystal substrate. We have shown that the spread of the parameters of individual Josephson junctions is critical for the operation of the SQIFs. The number of SQUIDs working at a certain bias point was less than 10% that led to the absence of the voltage dip at the zero external field. The large spread of the parameters can be explained by the inhomogeneity of the quality of the YBCO film on along the grain boundary. When the SQIF was fabricated on the bicrystal substrate with higher quality of the grain boundary the spread of critical currents decreased and the dip at zero external field appeared. Our experiments show a possibility of the fabrication of the high-T_c superconducting quantum interference filters on the bicrystal substrates. Nevertheless, SQIFs cannot outperform SQUIDs in a magnetometer configuration at the current state of reproducibility and quality of high-T_c Josephson junction fabrication.

5 Summary and outlook

High-T_c superconducting flip-chip magnetometers with inductively coupled flux transformer were developed and fabricated. Magnetometers consist of a bicrystal SQUID with large washer and a superconducting multilayer flux transformer. A new method for fabrication of multilayer high-T_c structures based on chemical mechanical polishing was developed to obtain shallow slopes of the superconducting electrodes. Optimized chemical mechanical polishing for high-T_c superconductors demonstrated very high (up to 90 %) yield and it is a promising method of production of multilayer high-T_c superconducting devices.

Magnetic field noise of fabricated flip-chip dc SQUID magnetometers was about 8 fT/Hz$^{1/2}$ at 2 kHz that is one of the best reported values. The magnetic field sensitivity can be further improved by increasing the size of the flux transformer to 30×30 mm^2. The magnetic field sensitivity below 2 kHz was lower (80 fT/Hz$^{1/2}$) due to the high $1/f$ flux noise. Investigations showed that this excess $1/f$ noise may originate from the thermally activated magnetic flux vortices motion in the flux transformer structure. Optimization of growth conditions should avoid undesirable a-oriented grains and likely improve 1/f noise.

Fabricated flip-chip SQUID magnetometers were successfully used in the ulf-NMR experiments. A proof-of-principle demonstration was performed. Direct benchmarking, in which the SQUID magnetometer with flux transformer was compared to a single layer SQUID sensor, was done. The measurements demonstrated more than 2-fold improvement in the SNR for the flip-chip sensor.

Finally, aperiodic arrays of randomly distributed SQUIDs (SQIF) were fabricated and tested. These arrays may benefit from higher voltage-to-flux transfer function as compared with a single SQUID. We have shown that spread of the parameters of individual Josephson junctions is critical for the operation of the SQIF. Our experiments show a possibility of the fabrication of the high-T_c superconducting quantum interference filters on the bicrystal substrates. Nevertheless, SQIFs cannot outperform SQUIDs in magnetometer configuration at the current state of reproducibility and quality of high-T_c Josephson junction fabrication.

Developed fabrication method based on CMP is very promising for fabrication of high-T_c multilayer structures with high reproducibility and throughput. While the magnetic field sensitivity of our high-T_c SQUID flip-chip magnetometers is about one order of magnitude lower than in low-T_c counterparts, the improved coupling to the signal sources results in similar signal-to-noise ratios. This, together with more flexible cooling systems, may enable applications of high-T_c SQUID magnetometers in MEG and ulf-NMR systems. State-of-the art microcooler systems may be used to develop high-T_c flexible multichannel MEG systems that further reduces the distance to the scalp and improves signal-to-noise ratios. One of the limiting factors of existing high-T_c SQUIDs is grain boundary Josephson junction technology that has relatively low reproducibility, high manufacturing cost and does not allow scaling of the fabrication process. Recent developments in our group demonstrated that SQUIDs based on high-T_c nanowires may be an alternative promising technology to replace bicrystal grain boundary Josephson junctions in high-T_c SQUID magnetometers.

Acknowledgements

I would like to thank the persons, who made this work possible, my supervisor Alexey Kalabukhov and Prof. Dag Winkler. Thank you for giving me the opportunity to work in such stimulating environment, for providing the means for my research, for guidance and advice.

Also I wish to thank Prof. Oleg Snigirev for his support and my colleagues from Moscow State University for all the years we worked together and the experience I've got there.

I wish to express my gratitude to my colleagues Justin Schneiderman, Fredrik Öisjöen and Magnus Jönsson for the help with the SQUID setup, MEG and ulf-NMR setup, for all the collaborative work and our fruitful discussions which helped me many times to look at the problem from another aspects.

Many thanks to Tom Johansen and Pavlo Mikheenko from Oslo University for their hospitality and help with obtaining magneto-optical images.

I would like to thank Henrik Frederiksen for the help with the deposition equipment. Thanks to Zonghe Lai for the help with obtaining of HR-TEM images and mask fabrication and all staffs of the cleanroom for help with fabrication issues and trainings. It was really great to work side by side with you all.

My warm gratitude and respect to Lars Jönsson and Staffan Pehrson for their golden hands. I am really glad to have you in Chalmers all these years of my experiment. Thanks to Susannah Carlsson, Maria Tremblay, and (of course!) Ann-Marie Frykestig for all the administrative support.

I thank Minshu Xie and Nikola Crovato for the discussions and help with experimental parts of my work as well as for the rest moments. I thank Samuel Alejandro Lara Avila for wise advices and words of encouragement.

I also grateful to all the members of Quantum Device Physics Laboratory, seniors and students for support and creating nice atmosphere to work in.

I would like to thank my excellent family: my parents, wife and brilliant son for the encouraging and support. Special thanks to my excellent wife for all the discussions during which she put different (although not always right) ideas into my head, which made me to think further.

Symbols and abbrevations

Table of symbols.

Symbol	Meaning
α	Coupling coefficient
μ_0	Vacuum permeability
λ_L	London penetration depth
ξ	Coherence length
β_c	Stewart-McCumber parameter
β_L	Inductance parameter
e	The electron elementary charge
h	Planck's constant
μ_0	Vacuum permeability
θ_F	Angle of the rotation of the polarization vector of FGF
Φ	Magnetic flux
Φ_{ext}	External magnetic flux
Φ_0	Magnetic flux quantum
ϕ	Phase
A_{eff}	Effective area
A_P	Effective area of pickup loop
a_m	Individual area element of the Josephson junction array
B_0	Measurement field for NMR/MRI
B	Magnetic field
$B_{CX,Y,Z}$	Earth's field cancellation fields for NMR/MRI in x, y, z, respectively
B_{ext}	External magnetic field
B_P	Prepolarization field
C	Capacitance
f	Frequency
D	Outer size of the pickup loop
D_S	SQUID washer outer size
d	Inner size of the pickup loop
d_{avg}	Average diameter of the input coil
d_{in}	Inner diameter of the input coil
d_{out}	Outer diameter of the input coil
d_F	Thickness of the FGF
d_S	Size of the dc SQUID loop
d_{TS}	Target-to-substrate distance

Symbol	Meaning
I_0	Maximum supercurrent
I	Current
I_D	Displacement current
I_f	Fluctuation current
I_F	Intensity of the light polarized by FGF
I_F^0	Incoming intensity of the light
I_{bias}	Bias current
I_c	Critical current
I_S	Supercurrent
J	Energy density
J_c	Critical current density
$K_{1,2}$	Constant from Wheeler formula
k	Coupling coefficient of galvanically coupled SQUID magnetometer
k_B	Boltzman constant
L_S	SQUID inductance
L_I	Input coil inductance
L_P	Pickup loop inductance
M_i	Mutual inductance
P_{O2}	Oxygen pressure
R_a	Average roughness
R_d	Dynamic resistance
R_n	Normal resistance
$\|S_N(\mathbf{B})\|$	Structure factor for the Josephson junction array
S_V	Spectral power density of the voltage noise
S_Φ	Equivalent flux noise
S_B	Equivalent magnetic field noise
T	Temperature
T_1	Longitudinal relaxation rate in NMR
T_c	Critical temperature
V	Voltage
$\overline{V}$	Average voltage
V_F	Verdet constant
V_{out}	Output voltage
V_Φ	Voltage-to-flux transfer junction

Table of abbreviations.

Abbreviation	Meaning
ac	Alterning current
AFM	Atomic force microscope
CMP	Chemical mechanical polishing
CCD	Charge-coupled device
dc	Direct current
GBJ	Grain boundary junction
FGF	Ferrite garnet film
FID	Free induction decay
FLL	Flux-locked loop
HR-TEM	High resolution transmission electron microscopy
IBE	Ion beam etching
MCG	Magnetocardiography
MEG	Magnetoencephalography
MOI	Magneto-optical imaging
MRI	Magnetic resonance imaging
NMR	Nuclear magnetic resonance
RCSJ	Resistively and capacitively shunted junction
rf	Radio frequency
RTS	Random telegrafic signal
PBCO	$PrBa_2Cu_3O_7$
PEB	Post exposure baking
PLD	Pulsed laser deposition
SAED	Selected area electron diffraction
SEM	Scanning electron microscopy
SIS	Superconductor-insulator-superconductor
SNR	Signal-to-noise ratio
SQIF	Superconducting quantum interference filter
SQUID	Superconducting quantum interference device
SPS	$SrTiO_3/PrBa_2Cu_3O_7/SrTiO_3$
STO	$SrTiO_3$
ulf-MRI	Ultra-low field magnetic resonance imaging
UV	Ultraviolet
YBCO	$YBa_2Cu_3O_{7-x}$

References

[1] J.G. Bednorz and K.A. Muller. Possible high-T_c superconductivity in the Ba-La-Cu-O system. *Zeitschrift fur Physik B (Condensed Matter)*, 64:189–193, 1986.

[2] B.D. Josephson. Possible new effects in superconducting tunneling. *Physics Letters*, 1(July):251–253, 1932.

[3] P. Anderson and M. Rowell. Probable observation of the Josephson superconducting tunneling effect. *Physical Review Letters*, 10(6):230–232, 1965.

[4] V. Ambegaokar and A Baratoff. Tunneling between superconductors. *Physical Review Letters*, 11:104, July 1963.

[5] W. C. Stewart. Current-Voltage Characteristics of Josephson Junctions. *Applied Physics Letters*, 12(8):277, 1968.

[6] D. E. McCumber. Structures for the Measurement of High-Frequency Properties of Point-Contact Josephson Junctions. *Journal of Applied Physics*, 39(1):297, 1968.

[7] V.V. Schmidt, P.(Eds.) Müller, and A.V.(Eds.) Ustinov. *The Physics of superconductors. Introduction to fundamentals and applications.* Springer, 1997.

[8] H. ed. Rogalla and P.H. Kes. *100 years of superconductivity.* CRC Press, 2012.

[9] T. Van Duzer and C.W. Turner. *Principles of superconductive devices and circuits.* Prentice Hall PTR, second edition, 1999.

[10] C.D. Tesche and J. Clarke. dc SQUID : Noise and Optimization. *Journal of Low Temperature Physics*, 29:301–331, 1977.

[11] J. Clark and A.I. Braginski. *The SQUID handbook.* WILEY-VCH, 2004.

[12] K. Enpuku, G. Tokita, and T. Maruo. Inductance dependence of noise properties of a high-T_c dc superconducting quantum interference device. *Journal of Applied Physics*, 76(12):8180, 1994.

[13] D. Drung. High-T_c and low-T_c dc SQUID electronics. *Superconductor Science and Technology*, 16:1320–1336, 2003.

[14] James E. Zimmerman and A. H. Silver. Quantum effects in type II superconductors. *Physics Letters*, 10(1):47–48, 1964.

[15] M. Gurvitch. High quality refractory Josephson tunnel junctions utilizing thin aluminum layers. *Applied Physics Letters*, 42(5):472, 1983.

[16] R.K. Singh and D. Kumar. Pulsed laser deposition and characterization of high-T_c $YBa_2Cu_3O_{7-x}$ superconducting films. *Material science and Engineering*, R22:113–185, 1998.

[17] A.K. Saxena. High-Temperature Superconductors. *Springer Series in Materials Science*, 125:41–57, 2010.

[18] J.R. Waldram. *Superconductivity of metals and cuprates.* IOP Publishing, 1996.

[19] P. Chaudhari, J. Mannhart, D. Dimos, C.C. Tsuei, J. Chi, M.M. Oprysko, and M. Scheuermann. Direct measurements of the superconducting properties single grain boundaries in YBCO. *Physical Review Letters*, 60(16):1653–1656, 1988.

[20] J. Mannhart, P. Chaudhari, D. Dimos, C.C. Tsuei, and T.R. McGuire. Critical current in [001] grain and across their tilt boundaries in YBCO Films. *Physical Review Letters*, 61(21):2476–2479, 1988.

[21] B. Mayer, S. Schuster, A. Beck, L. Alff, and R. Gross. Magnetic field dependence grain boundary junctions of the critical current in $YBa_2Cu_3O_{7-x}$ bicrystal. *Applied Physics Letters*, 62(7):783–785, 1993.

[22] H. Hilgenkamp. Grain boundaries in high-T_c superconductors. *Reviews of Modern Physics*, 74(April):485–549, 2002.

[23] A. Beck, A. Stenzel, M. Froehlich, R. Gerber, R. Gerdemann, L. Alff, B. Mayer, R. Gross, A. Marx, J.C. Villegier, and H. Moriceau. Fabrication and Superconducting Transport Properties of Bicrystal Grain Boundary Josephson Junctions on Different Substrates. *IEEE Transactions on Applied Superconductivity*, 5(2):2192–2195, 1995.

[24] D. Koelle, R. Kleiner, F. Ludwig, E. Dantsker, and J. Clarke. High-transition-temperature superconducting quantum interference devices. *Reviews of Modern Physics*, 71(3):631–686, 1999.

[25] J. Jaycox and M. Ketchen. Planar coupling scheme for ultra low noise DC SQUIDs. *IEEE Transactions on Magnetics*, 17(1):400–403, January 1981.

[26] M.B. Ketchen and J.M. Jaycox. Ultra-low-noise tunnel junctions dc SQUID with a tightly coupled planar input coil. *Applied Physics Letters*, 40(8):736–738, 1982.

[27] M.B. Ketchen. Design of improved integrated thin-film planar dc SQUID gradiometers. *Journal of Applied Physics*, 58(11):4322–4325, 1985.

[28] F. Ludwig, E. Dantsker, D. Koelles, R. Kleiner, A.H. Miklich, and J. Clarke. Multilayer magnetometers based on high-T_c SQUIDs. *Applied Superconductivity*, 3(7-10):383–398, 1995.

[29] M.I. Faley, U. Poppe, K. Urban, D.N. Paulson, T.N. Starr, and R.L. Fagaly. Low noise HTS dc-SQUID flip-chip magnetometers and gradiometers. *IEEE Transactions on Applied Superconductivity*, 11(I):1383–1386, 2001.

[30] M.N. Keene, S.W. Goodyear, N.G. Chew, R.G. Humphreys, J.S. Satchell, J.A. Edwards, and K. Lander. Low noise $YBa_2Cu_3O_7$-$PrBa_2Cu_3O_7$ multiturn flux transformers. *Applied Physics Letters*, 64(3):366–368, 1994.

[31] http://www.elekta.com/healthcare-professionals/products/elekta-neuroscience/functional-mapping/elekta-neuromag-product-specifications.html. August 2013.

[32] I.K. Kominis, T.W. Kornack, J.C. Allred, and M.V. Romalis. A subfemtotesla multichannel atomic magnetometer. *Nature*, 422(6932):596–9, April 2003.

[33] M. Pannetier-Lecoeur, L. Parkkonen, N. Sergeeva-Chollet, H. Polovy, C. Fermon, and C. Fowley. Magnetocardiography with sensors based on giant magnetoresistance. *Applied Physics Letters*, 98(15):153705, 2011.

[34] M. Matsuda, Y. Murayama, S. Kiryu, N. Kasai, M Kashiwaya, M Koyanagi, and T Endo. Directly-coupled dc SQUID magnetometers made of Bi-Sr-Ca-Cu oxide films. *IEEE Trans. Magn. MAG-27*, 27:3043–3046, 1991.

[35] D. Koelle, A. H. Miklich, F. Ludwig, E. Dantsker, D. T. Nemeth, and J. Clarke. dc SQUID magnetometers from single layers of YBCO. *Applied Physics Letters*, 63(16):2271, 1993.

[36] F. Öisjöen, J. F. Schneiderman, G. a. Figueras, M. L. Chukharkin, a. Kalabukhov, a. Hedström, M. Elam, and D. Winkler. High-Tc superconducting quantum interference device recordings of spontaneous brain activity: Towards high-Tc magnetoencephalography. *Applied Physics Letters*, 100(13):132601, 2012.

[37] P. Seidel, C. Becker, A. Steppke, M. Buettner, H. Schneidewind, V. Grosse, G. Zieger, and F. Schmidl. Long-time stable high-temperature superconducting DC-SQUID gradiometers with silicon dioxide passivation for measurements with superconducting flux transformers. *Superconductor Science and Technology*, 20(11):S380–S384, November 2007.

[38] D. Drung, F. Ludwig, W. Müller, U. Steinhoff, L. Trahms, H. Koch, Y. Q. Shen, M. B. Jensen, P. Vase, T. Holst, T. Freltoft, and G. Curio. Integrated $YBa_2Cu_3O_{7-x}$ magnetometer for biomagnetic measurements. *Applied Physics Letters*, 68(10):1421–1423, 1996.

[39] M.I. Faley, U. Poppe, K. Urban, D.N. Paulson, and R.L. Fagaly. A New Generation of the HTS Multilayer DC-SQUID Magnetometers and Gradiometers. *Journal of Physics: Conference Series*, 43:1199–1202, June 2006.

[40] C. D. Gratta, V. Pizzella, F. Tecchio, and G.L. Romani. Magnetoencephalography – a noninvasive brain imaging method with 1 ms time resolution. *Reports on progress in Physics*, 64:1759–1841, 2001.

[41] A.I. Ahonen, M. Hamalainen, M. J. Kajola, J. E. T. Knuutila, P. P. Laine, O. V. Lounasmaa, L. T. Parkkonen, J. T. Simola, and C. D. Tesche. 122-Channel SQUID Instrument for Investigating the Magnetic Signals from the Human Brain. *Physica Scripta*, T49:198–205, 1993.

[42] S. Comani, M. Liberati, D. Mantini, E. Gabriele, D. Brisinda, S. Di Luzio, R. Fenici, and G.L. Romani. Characterization of fetal arrhythmias by means of fetal magnetocardiography in three cases of difficult ultrasonographic imaging. *Pacing and clinical electrophysiology : PACE*, 27(12):1647–55, December 2004.

[43] J. Clarke, M. Hatridge, and M. Mössle. SQUID-detected magnetic resonance imaging in microtesla fields. *Annual review of biomedical engineering*, 9:389–413, January 2007.

[44] D. Cohen, E. Edelsack, and J.E. Zimmerman. Magnetocardiograms Taken Inside a Shielded Room With a Superconducting Point-Contact Magnetometer. *Applied Physics Letters*, 16(7):278, 1970.

[45] S. T. Achenbach and W. Moshage. Magnetocardiography: clinical investigations with a biomagnetic multichannel system. *Physiological measurement*, 14 Suppl 4A:A61–8, November 1993.

[46] S. Busch, M. Hatridge, M. Möß le, W. Myers, T. Wong, M. Mück, K. Chew, K. Kuchinsky, J. Simko, and J. Clarke. Measurements of T(1) -relaxation in ex vivo prostate tissue at 132 μT. *Magnetic resonance in medicine : official journal of the Society of Magnetic Resonance in Medicine / Society of Magnetic Resonance in Medicine*, 67(4):1138–45, April 2012.

[47] M. Hämäläinen, R. Hari, R. J. Limoniemi, J. Knuutila, and Louasmaa O. V. Magnetoencephalography – theory, instrumentation, and applications to noninvasive studies of the working human brain. *Rev. Mod. Phys.*, 65(2):413–497, 1993.

[48] D. Cohen. Magnetoencephalography : Detection of the Brain ' s Electrical Activity with a Superconducting Magnetometer. *Science*, 175(4022):664–666, 1972.

[49] J. Mannhart. Current Transport Across Grain Boundaries in Superconducting YBCO films. *Journal of Superconductivity*, 3(3):281–285, 1990.

[50] D. Grundler, B. David, F.L. Eckart, and O. Dössel. Highly sensitive $YBa_2Cu_3O_{7-x}$ dc SQUID magnetometer with thin-film flux transformer. *Applied Physics Letters*, 63(19):2700–2702, 1993.

[51] F. Ludwig, D. Koelle, E. Dantsker, D. T. Nemeth, a. H. Miklich, John Clarke, and R. E. Thomson. Low noise $YBa_2Cu_3O_7$ - $SrTiO_3$ - $YBa_2Cu_3O_7$ multilayers for improved superconducting magnetometers. *Applied Physics Letters*, 66(3):373–375, 1995.

[52] Y. Q. Shen, Z. J. Sun, R. Kromann, T. Holst, P. Vase, and T. Freloft. Integrated high-T_c superconducting magnetometer with multiturn input coil and grain boundary junctions. *Applied Physics Letters*, 67(14):2081–2083, 1995.

[53] W. Eidelloth, W. J. Gallagher, R. P. Robertazzi, R. H. Koch, B. Oh, and R. L. Sandstrom. Wet etch process for patterning insulators suitable for epitaxial high-T_C superconducting thin film multilevel electronic circuits. *Applied Physics Letters*, 59(10):1257–1259, 1991.

[54] M.I. Faley, U. Poppe, H. Soltner, C.L. Jia, M. Siegel, and K. Urban. Josephson junctions, interconnects, and crossovers on chemically etched edges of $YBa_2Cu_3O_{7-x}$. *Applied Physics Letters*, 63(15):2138–2140, 1993.

[55] U.M. Boguslavskij, J. Gao, A.J.H.M. Rijnders, D. Terpstra, G.J. Gerritsma, and H. Rogalla. Josephson junctions, interconnects, and crossovers on chemically etched edges of $YBa_2Cu_3O_{7-x}$. *Applied Physics Letters*, 63(15):2138–2140, 1993.

[56] M.I. Faley, U. Poppe, C.L. Jia, V.N. Glyantsev, M. Siegel, and K. Urban. Properties of Josephson edge type junctions prepared with Br-ethanol etching. *Physica C: Superconductivity*, 235-240:591–592, December 1994.

[57] M.I. Faley, U. Poppe, C L Jia, and K. Urban. Proximity effect in edge type junctions with $PrBa_2Cu_3O_7$ barriers prepared by Br-ethanol etching. *IEEE Transactions on Applied Superconductivity*, 5(2):2091–2094, 1995.

[58] M.I. Faley, U. Poppe, C.L. Jia, and K. Urban. Size, order and interface effects on $PrBa_2Cu_3O_7$ barriers. *IEEE Transactions on Applied Superconductivity*, 7(2):2514–2517, 1997.

[59] J. Dae Suh and G.Y. Sung. Behavior of the droplets ejecting from the YBCO target during the pulsed laser deposition. *Physica C: Superconductivity*, 235-240:571–572, December 1994.

[60] T. Petrisor, V. Boffa, F. Fabbri, D. Neri, A. Montone, and M. Krasnowski. Structural and morphological properties of in-situ PLD YBCO/STO/YBCO trilayer. *Superlattices and Microstructures*, 21(3):487–491, 1997.

[61] A.V. Varlashkin, S.I. Krasnosvobodtsev, M.L. Chukharkin, O.V. Snigirev, A. V. Tsikunov, and N.P. Shabanova. Deposition of smooth high-T_c superconducting films with a solid-state YAG:Nd^{3+} laser. *Technical Physics*, 52(5):660–662, May 2007.

[62] G. Brorsson, E. Olsson, P.Å Nilsson, and T. Claeson. Growth and properties of $YBa_2Cu_3O_{7-x}/(SrTiO_3/PrGaO_3)/YBa_2Cu_3O_{7-x}$ trilayers: Optimization of the insulation. *Journal of Applied Physics*, 75(2):827–834, 1994.

[63] H. Takashima, N. Terada, and M. Koyanagi. Improvement of $SrTiO_3$ thin film surface polished by chemical mechanical planarization for HTS

multilayer device. *IEEE Transactions on Applied Superconductivity*, 9(2):3464–3467, 1999.

[64] M. Maruyama, T. Furutani, Y. Yoshinaga, T. Kito, G. Matsuda, H Akaike, M Inoue, A Fujimaki, and H Hayakawa. Planarization of the YBa2Cu3O7-x base electrodes in trilayer josephson junctions. *Japanese Journal of Applied Physics*, 40:932–934, 2001.

[65] Y. Wada, K. Kuroda, and T. Takami. Fabrication of YBCO multi-layer wiring with polished PBCO insulator. *IEEE Transactions on Applied Superconductivity*, 13(2):817–820, 2003.

[66] J.D. Pedarnig, K. Siraj, M.a. Bodea, I. Puica, W. Lang, R. Kolarova, P. Bauer, K. Haselgrübler, C. Hasenfuss, I. Beinik, and C. Teichert. Surface planarization and masked ion-beam structuring of $YBa_2Cu_3O_{7-x}$ thin films. *Thin Solid Films*, 518(23):7075–7080, September 2010.

[67] P. Å. Nilsson, G. Brorsson, J.M. Orliaguet, E. Olsson, H. Olin, M. Gustafsson, and T. Claeson. Planarized Patterning of Y-Ba-Cu-O Thin Films for Multilayer Technology. *IEEE Transactions on Applied Superconductivity*, 5(2):1653–1656, 1995.

[68] B. Prijamboedi, H. Takashima, and A. Shoji. AFM study of $SrTiO_3$ and $YBa_2Cu_3O_{7-x}$ multilayer surface treated with chemical mechanical polishing process. *Journal of Physics: Conference Series*, 43:325–328, June 2006.

[69] H. Takashima, N. Kasai, and A. Shoji. Fabrication of high-quality $YBa_2Cu_3O_{7-x}$ multilayer structure using chemical mechanical planarization for superconducting quantum interference device gradiometer. *Japanese Journal of Applied Physics*, 41:L1062–L1065, October 2002.

[70] H. Takashima, N. Kasai, and A. Shoji. Fabrication of grain boundary Josephson junction on top layer of YBCO multilayer using chemical mechanical planarization. *Physica C: Superconductivity*, 392-396:1367–1372, October 2003.

[71] K. Kuroda, Y. Wada, T. Takami, T. Ozeki, and K. Hamanaka. YBaCuO/PrBaCuO/YBaCuO trilauer junctions with the polished YBaCuO electrodes. *Physica C: Superconductivity*, 392-396:1358–1361, October 2003.

[72] K. Kuroda, Y. Wada, T. Takami, and T. Ozeki. Fabrication of full high-T_c superconducting $YBa_2Cu_3O_{7-x}$ trilayer junctions using a polishing technique. *Japanese Journal of Applied Physics*, 42:L1006–L1008, August 2003.

[73] P. Michalowski, T. Shapoval, D. Meier, C. Katzer, F. Schmidl, L. Schultz, and P. Seidel. Enhancement of high-T_c superconducting thin film devices by nanoscale polishing. *Superconductor Science and Technology*, 25(11):115019, November 2012.

[74] T. Shapoval, S. Engel, M. Gründlich, D. Meier, E. Backen, V. Neu, B. Holzapfel, and L. Schultz. Nanoscale wedge polishing of superconducting thin films-an easy way to obtain depth dependent information by surface analysis techniques. *Superconductor Science and Technology*, 21(10):105015, 2008.

[75] G. Banerjee and R. L. Rhoades. Chemical Mechanical Planarization historical review and future direction. *ECS Transactions*, 13(4):1–19, 2008.

[76] S.A. Campbell. *Fabrication engineering at the micro- and nanoscale.* Oxford University Press, third edition, 2008.

[77] G. Nanz and L.E. Camilletti. Modeling of Chemical-Mechanical Polishing : A Review. *IEEE Transactions on Semiconductor Manufacturing*, 8(4):382–389, 1995.

[78] J.-W. Jung, J.-M Kim, J.-H. Son, and Y. Lee. Dependence of subthreshold hump and reverse narrow channel effect on the gate length by suppression of transient enhanced diffusion at trench isolation edge. *Japanese Journal of Applied Physics*, 39:2136–2140, 2000.

[79] http://www.logitech.uk.com/products-solutions/products-and-accessories/products/pm5-lapping-polishing-system.aspx. August 2013.

[80] http://www.logitech.uk.com/products-solutions/products-and-accessories/consumables/polishing-suspensions.aspx. August 2013.

[81] H.A. Wheeler. Simple Inductance Formulas for Radio Coils. *Proc. IRE*, 16(10):1398–1400, 1928.

[82] S.S. Mohan, M. del Mar Hershenson, S.P. Boyd, and T.H. Lee. Simple accurate expressions for planar spiral inductances. *IEEE Journal of Solid-State Circuits*, 34(10):1419–1424, 1999.

[83] M.M. Khapaev, A.Y. Kidiyarova-Shevchenko, P. Magnelind, and M. Yu. Kupriyanov. 3D-MLSI : Software Package for Inductance Calculation in Multilayer Superconducting Integrated Circuits. *IEEE Journal of Solid-State Circuits*, 11(1):1090–1093, 2001.

[84] M.M. Khapaev. Inductance extraction of multilayer finite-thickness superconductor circuits. *IEEE Transactions on Microwave Theory and Techniques*, 49(1):217–220, 2001.

[85] M. Chukharkin, A. Kalabukhov, J. F. Schneiderman, F. Öisjöen, O. Snigirev, Z. Lai, and D. Winkler. Noise properties of high-T_C superconducting flux transformers fabricated using chemical-mechanical polishing. *Applied Physics Letters*, 101:042602, 2012.

[86] E. Dantsker, S. Tanaka, and John Clarke. High-T_c super conducting quantum interference devices with slots or holes: Low $1/f$ noise in ambient magnetic fields. *Applied Physics Letters*, 70(15):2037, 1997.

[87] M. J. Ferrari, Mark Johnson, F. C. Wellstood, J. J. Kingston, T. J. Shaw, and John Clarke. Magnetic flux noise in copper oxide superconductors. *Journal of Low Temperature Physics*, 94(1-2):15–61, January 1994.

[88] Ch. Jooss, J. Albrecht, H. Kuhn, S. Leonhardt, and H. Kronmuller. Magneto-optical studies of current distributions in high-T_c superconductors. *Reports on progress in Physics*, 65:651–788, 2002.

[89] Pål Erik Goa, Harald Hauglin, Michael Baziljevich, Eugene Il, Peter L Gammel, and Tom H Johansen. Real-time magneto-optical imaging of vortices in superconducting $NbSe_2$. *Superconductor Science and Technology*, 14:729–731, 2001.

[90] P. E. Goa, H. Hauglin, Å.A.F. Olsen, M. Baziljevich, and T. H. Johansen. Magneto-optical imaging setup for single vortex observation. *Review of Scientific Instruments*, 74(1):141, 2003.

[91] K. Enpuku, S. Hirakawa, R. Momotomi, M. Matsuo, and T. Yoshida. Performance of HTS SQUID using resonant coupling of cooled Cu pickup coil. *Physica C: Superconductivity*, 471(21-22):1234–1237, November 2011.

[92] J. Oppenländer, Ch. Häussler, and N. Schopohl. Non-Φ0-periodic macroscopic quantum interference in one-dimensional parallel Josephson junction arrays with unconventional grating structure. *Physical Review B*, 63(2):024511, December 2000.

[93] J. Oppenländer, Ch. Häussler, T. Träuble, and N. Schopohl. Highly sensitive magnetometers for absolute magnetic field measurements based on quantum interference filters. *Physica C: Superconductivity*, 368:119–124, 2002.

[94] V. Schultze, R. Ijsselsteijn, H.-G. Meyer, Jörg Oppenländer, Christoph Häussler, and Nils Schopohl. High-T_c Superconducting Quantum Interference Filters for Sensitive Magnetometers. *IEEE Transactions on Applied Superconductivity*, 13(2):775–778, 2003.

[95] V. Schultze, R. Ijsselsteijn, R. Boucher, H.-G. Meyer, and J. Oppenländeer. Improved high-T_c superconducting quantum interference filters for sensitive magnetometry. *Superconductor Science and Technology*, 16:1356–1360, 2003.

[96] P. Caputo, J. Oppenländer, Ch. Häussler, J. Tomes, a. Friesch, T. Träuble, and N. Schopohl. High-performance magnetic field sensor based on superconducting quantum interference filters. *Applied Physics Letters*, 85(8):1389, 2004.

[97] Vinay Ambegaokar and B. I. Halperin. Voltage due to the thermal noise in the dc Josephson effect. *Physical Review Letters*, 22(25):1364–1366, 1969.

[98] R. Gross, P. Chaudhari, D. Dimos, A. Gupta, and G. Koren. Thermally activated phase slippage in high-T_c grain-boundary Josephson junctions. *Physical Review Letters*, 64(2):228–231, August 1990.